OPTICAL CHARACTERIZATION OF MOLYBDENUM DISULFIDE BY RAMAN AND PHOTOLUMINESCENCE

SUN LINFENG

DIVISION OF PHYSICS AND APPLIED PHYSICS

SCHOOL OF PHYSICAL AND MATHEMATICAL SCIENCES

NANYANG TECHNOLOGICAL UNIVERSITY

2015

OPTICAL CHARACTERIZATION OF MOLYBDENUM DISULFIDE
BY RAMAN AND PHOTOLUMINESCENCE

SUN LINFENG

2015

OPTICAL CHARACTERIZATION OF MOLYBDENUM DISULFIDE BY RAMAN AND PHOTOLUMINESCENCE

SUN LINFENG

School of Physical and Mathematical Sciences

A thesis submitted to the Nanyang Technological University
in fulfillment of the requirement for the degree of
Doctor of Philosophy

2015

Acknowledgements

I am grateful to many people who have helped me during my PhD period. Firstly, I would like to express my great acknowledgement to my supervisor, Prof Shen Zexiang, for his patient guidance and fruitful discussions. His comprehensive knowledge, rich research experience and strict attitude will strongly affect my research career in future. It is a great honor for me to be a member in his group. Moreover, I appreciate Nanyang Associate Professor Yu Ting, Nanyang Assistant Professor Liu Zheng, and Professor Liu Lei for their help on my projects.

I also would like to thank my colleagues, Dr Zhan Da, Dr Yan Jiaxu, Dr Hu Hailong, Mr Zheng Shoujun, Dr Liu Fucai, Dr Lu Congxiang, Dr Li Hong, Dr Liu Hai, Mr Zhang Bowei, Dr Zhang Xin, Mr Wang Xuewen, Dr Qiu Caiyu and Dr Shang Jingzhi for their suggestions on my projects.

It is my pleasure to extent my great gratitude to all of my friends around me. They not only help me broaden the range of professional knowledge, but also give me an enjoyable atmosphere in my daily life. It is really my pleasure to study in this group.

Finally, I would like to give my appreciation to my mother. In recent years, I have no enough time to take my responsibility for the care of my aged mother and I feel guilty about that. Hereby many thanks for her support and understanding in those hard years.

Table of contents

Summary

This thesis mainly presents results on the fabrication methods (mechanically exfoliation (ME) and chemical vapor deposition (CVD)) and Raman (photoluminescence (PL)) spectroscopy characterization of molybdenum disulfide (MoS_2) layers. The thesis could be divided into five parts as follows:

The first part (Chapter 1 and 2) gives a literature review on the fundamental knowledge of Raman and photoluminescence spectroscopic techniques in first. The physical properties of MoS_2 layers, such as thickness-dependent electronic band structures and valleytronics, are introduced. The recent research progress on the relationship between Raman (PL) features and the physical properties of MoS_2 layers is reviewed. Moreover, the fabrication methods of MoS_2 samples and the main facilities used in the work (Raman (PL) facilities) are also introduced, as well as our preliminary results on CVD grown MoS_2.

In the third part (Chapter 3), we experimentally observe the dramatically enhanced overtone and combination Raman modes of E_{2g}^{1} and A_{1g} in monolayer and few layer MoS_2 when samples excited by 325 nm laser. While other laser lines 457 nm, 488 nm and 532 nm are used as excitation sources, we don't observe such an enhancement of overtone and combination modes. The first principles calculations based on density functional theory with considering spin-orbital coupling effects, reveal the possible transition process excited by 325 nm laser and the partial charge density of electronic bands further confirms it. The significance of this work is to determine the value of spin-orbital splitting in single layer MoS_2 experimentally, which clarifies the

confusion on the different values of spin orbital splitting by various calculation methods.

The fourth part (Chapter 4) reveals MoS_2 layers after plasma treatment could be used as the substrate of surface enhanced Raman scattering (SERS). The main types of defects introduced during plasma treatment are investigated by the first principle calculations. Raman and photoluminescence spectra (before and after plasma treatment) are used to help us clarify the mechanism of enhancement. The surface treatment by plasma leads to the charge redistribution in defective MoS_2 nanosheets which facilitates the charge transfer between Rhodamine 6G (R6G) molecules and defective MoS_2. The PL spectra of defective MoS_2 nanosheets before and after R6G molecules deposited are also investigated. The PL shift also verifies the charge transfer between them. This work proposes a way of improving the SERS effect on low dimensional semiconductor materials.

The fifth part (Chapter 5) compares the PL spectra of CVD grown and mechanically exfoliated single layer MoS_2. By measuring the PL spectra of MoS_2 in vacuum, it is revealed that the abnormally strong photoluminescence intensity in CVD grown MoS_2 is not its intrinsic behaviors but is related to the adsorption behavior of adsorbates in air. Combined with Raman spectra and electrical performance of MoS_2 in vacuum and in air, respectively, we get the conclusion that the adsorbates in air contribute to the p-doping effect for MoS_2 nanosheets. For the components of adsorbates in air, first principles calculations show that both N_2 and O_2 contributed to the p-doping effect of defective single layer MoS_2. This work sheds light on how to engineer optical properties of the single layer MoS_2 and makes it a possible material for lighting emitting application.

Publications

1. **Linfeng Sun**†, Jiaxu Yan†, Da Zhan, Liu Lei, Hailong Hu, Hong Li, Benkang Tay, Jer Lai Kuo, Chung Che Huang, Daniel W. Hewak, Pooi See Lee, Zexiang Shen, Spin-Orbit Splitting in Single Layer MoS_2 Revealed by Triply Resonant Raman Scattering, ***Physics Review Letters***, 111 (2013), 126801 (Equal Contribution)

2 **Linfeng Sun**, Hailong Hu, Da Zhan, Jiaxu Yan, Lei Liu, Pooi See Lee, Zexiang Shen, Plasma Modified MoS_2 Nanoflakes for Surface Enhanced Raman Scattering, ***Small***, 10 (2014),6, 1090-1095

3 Shoujun Zheng, **Linfeng Sun**, Xiaohao Zhou, Fucai Liu, Zheng Liu, Zexiang Shen, Hongjin Fan, Coupling and Interlayer Exciton in Twist-Stacked WS_2 Bilayers, ***Advanced Optical Materials***, DOI: 10.1002/adom.201500301

4 Zhaogang Nie, Run Long, **Linfeng Sun**, ChungChe Huang, Jun Zhang, Qihua Xiong, Daniel W. Hewak, Zexiang Shen, Oleg V. Prezhdo, and Zhiheng Loh, Ultrafast Carrier Thermalization and Cooling Dynamics in Few Layer MoS_2, ***ACS Nano***, 8(2014).10,10931-10940

5 Shoujun Zheng, **Linfeng Sun**, Tingting Yin, Alexander M. Dubrovkin, Fucai Liu, Zheng Liu, Zexiang Shen, Hongjin Fan, Monolayer of $W_xMo_{1-x}S_2$ Alloy with in Plane Composition Variations. ***Applied Physics Letters***, 106, 063113(2015)

6 Xuesong Yin, Chunhua Tang, **Linfeng Sun**, Zexiang Shen, Hao Gong, Study on Phase Formation Mechanism of Non and Near Stoichiometric $Cu_2ZnSn(S,Se)_4$ Film Prepared by Selenization of Cu-Sn-Zn-S Precursors. ***Chemistry of Materials***, 26 (2014) 2005-2014

7 Jin Wang, Linlin Li, Chui Ling Wong, **Linfeng Sun**, Zexiang Shen, Srinivasan Madhavi, Controlled synthesis of a-FeOOH nanorods and their transformation to mesoporous a-Fe_2O_3, Fe_3O_4@C nanorods as anodes for lithium ion batteries, ***RSC Advances***, 3 (2013) 15316-15326

8 Jiadong Zhou, Qingsheng Zeng, Danhui Lv, **Linfeng Sun**, Lin Niu, Fei Fu, Fucai Liu, Zexiang Shen, Chuanhong Jin, and Zheng Liu, Controlled Synthesis of High Quality Monolayered α-In_2Se_3 via Physical Vapor Deposition, ***Nano Lett***, 2015, 15

(10), 6400

9 Ran Cheng, Wei Huang, Xiao Gong, **Linfeng Sun**, Pengfei Guo, Hailong Hu, Zexiang Shen, Genquan Han, Yee Chia Yeo, Relaxed and Strained Patterned Germanium Tin Structures: A Raman Scattering Study, ***ECS Journal of Solid State Science and Technology***, 2(4), 2013, 138-145

10 K.K. Ansah Antwi, C. B. Soh, Q. Wee, Rayson J. N. Tan, P. Yang, H. R. Tan, **L. F. Sun**, Z. X. Shen, S. J. Chua, ***Journal of Applied Physics***, 114 (2013) 243512

11 Xuesong Yin; Tang Jiao Huang; Chunhua Tang; Ming Du; **Linfeng Sun**; Zexiang Shen; Hao Gong, Significantly different mechanical properties and interfacial structures of $Cu_2ZnSn(S,Se)_4$ films prepared from metallic and sulfur-contained precursors, ***Solar Energy Materials and Solar cells***, 134 (2015) 389

12 Jie Tang, Jianwei Chai, Jian Huang, Liyuan Deng, Xuansang Nguyen, **Linfeng Sun**, T Venkatesan, Zexiang Shen, Chuanbeng Tay, Soo Jin Chua, ZnO nanorods with low intrinsic defects and high optical performance grown by facile microwave assisted solution method. ***ACS Applied Materials & Interfaces***. 2015, 7 (8), 4737-4743

13 Mukherjee Bablu, Wei Sun Leong, Yida Li, Hao Gong, **Linfeng Sun**, Zexiang Shen, John T L Thong, Raman Analysis of Gold on WSe_2 Single Crystal Film. ***Materials Research Express***. 2015, 2(6)

Conference Presentation

14. Linfeng Sun, Hailong Hu, Da Zhan, Pooi See Lee, Zexiang Shen, 7th ICMAT 2013, June 30 to 5 July, Suntec, Singapore (**Best Poster**).

15. **Linfeng Sun**, Jiaxu Yan, Da Zhan, Zexiang Shen, the OCPA8 International Conference on Physics Education and Frotier Physics 2014, June 23-27, Singapore (**Best Poster**).

Chapter 1
Introduction

1.1 Introduction to molybdenum disulfide

Moore's law reveals that the number of transistors doubles on integrated circuits about every 18 months [1-4]. However, because of the limitation from material and fabrication process, it cannot be sustained indefinitely [3]. The studies of two dimensional (2D) materials maybe continue this law and extend this limitation of miniaturization to the atomic level, especially due to the discovery of graphene in 2004 [5]. Graphene, with a single carbon atomic layer bonded in sp^2 way, has attracted the attention of researchers worldwide because of its distinctive electronic properties [6-8]. Particularly, its carrier mobility is remarkably high with reported value about 15000 $cm^2V^{-1}S^{-1}$ at 300K [9]. However, graphene has no bandgap which limits its application on nano-electronic devices [10-12]. Many kinds of approaches have been reported to engineer the bandgap of graphene, but it increases the processing complexity and reduces its intrinsic carrier mobility [13-15]. Therefore, it is urgent to find an alternatively ultra-thin material to replace graphene.

Transition metal dichalcogenides (TMDs), similar to graphene as layered materials, have gained renewed interest in the past years because of their natural bandgap [16-19]. Transition metal atoms (typically Mo, W) are sandwiched between two layers of chalcogen atoms (typically S, Se, or Te). Due to the plenty varieties of transition metal and chalcogen atoms, more than 40 different categories could be combined

[19-24]. Molybdenum disulfide (MoS_2), as a typical member of TMD group, displays exotic mechanical, optical and electronic properties [16-18]. A monolayer MoS_2 is a direct bandgap semiconductor, which makes it potential to be widely investigated in transistors [16, 25, 26], gas sensors [27, 28], Li ion batteries [29, 30], photovoltaic [31, 32], hydrogen production [33, 34], and dry lubricant [35] etc. The reported on/off current ratio of single-layer MoS_2 transistors exceeds 10^8 at room temperature [16], which is much higher than that of graphene based transistors [36], and comparable with that of the silicon based transistors [37]. Moreover, another special interesting feature of MoS_2 is its promising applications in spintronics and valleytronics [38-40]. The factor making MoS_2 unique is the strong spin–orbit interaction (SOI) due to the lack of inversion symmetry, which leads to the strongly coupled spin/valley physics in monolayer MoS_2.

However, the discussions on some fundamental properties of MoS_2 are still in debate, such as the origin of its photoluminescence (PL) peaks [41-43], the effect of substrates or ambient on the optical features of MoS_2, the spin-relaxation mechanisms of such a system etc [17, 44]. Since the exploration of fundamental property is the first step for potential applications of MoS_2, it is important to search a simple, effective and reliable way to explore the fundamental properties of MoS_2, such as electronic structure, and electron phonon interactions. This chapter will introduce some previously fundamental studies of MoS_2, including its crystal structure, electronic structure, electron phonon coupling, Raman and PL spectra.

1.1.1 The crystal structures of MoS_2 layers

MoS_2, as a typically layered material with the weak van der Waals force to stack the adjacent layers, consists of S-Mo-S layers with Mo atom sandwiched between two S atoms by covalent bond [18, 19]. The thickness of single layer MoS_2 is about 0.615 nm while the unit cell of MoS_2 includes two layers with the lattice constant c value ~ 1.2294 nm [45]. The three dimensional structure and the unit cell of MoS_2 are shown in Figure 1.1. The interactions between adjacent layers are weak van der Waals forces with a usual Bernal stacking order [18, 42]. While a single layer MoS_2 usually named as its 1H phase. Its unit cell, as shown in Figure 1.1 (b), is a triangular prism. The Mo atom is located in the center of the unit cell and it is bound with six S atoms by strong covalent bonds [46]. It is obvious that for the single layer MoS_2, the inversion symmetry is broken. However, for bulk MoS_2, such an inversion symmetry in spatial is kept, as shown in Figure 1.1(b) [47]. The symmetrical space group of bulk MoS_2 is P3m1 (point group D_{6h}), while the space group of the single layer MoS_2 is P6m2 (point group D_{3h}) [46, 48-50]. From the discussion above, it is naturally raised in mind that the spatial inversion symmetry of MoS_2 layers with even number and odd number should belong to the different space groups [38, 51-53]. The former (with inversion symmetry) and the latter (without inversion symmetry) belong to the space group: P3m1 and P6m2, respectively. Besides the 2H-type MoS_2 crystal, other phases of MoS_2 nanosheets fabricated by synthetic and chemically exfoliated methods may exist, such as 1T, 3R phases, which have presented distinct electronic structures [19, 39, 54, 55].

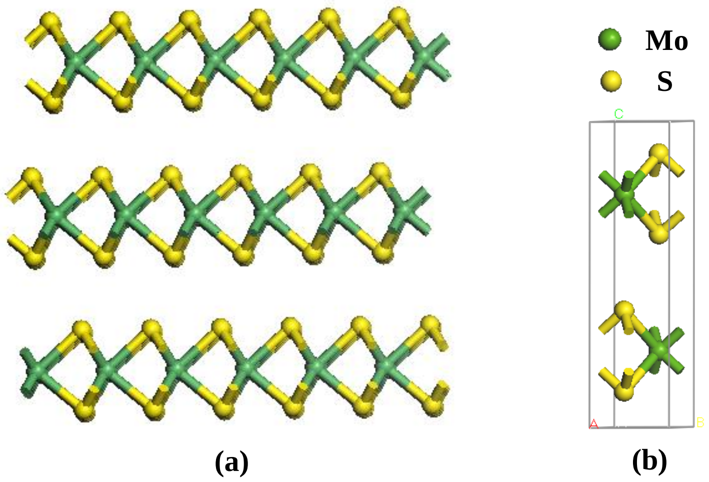

Figure 1.1 *(a) Three dimensionally schematic structure of* MoS_2*; (b) Unit cell of bulk* MoS_2*.*

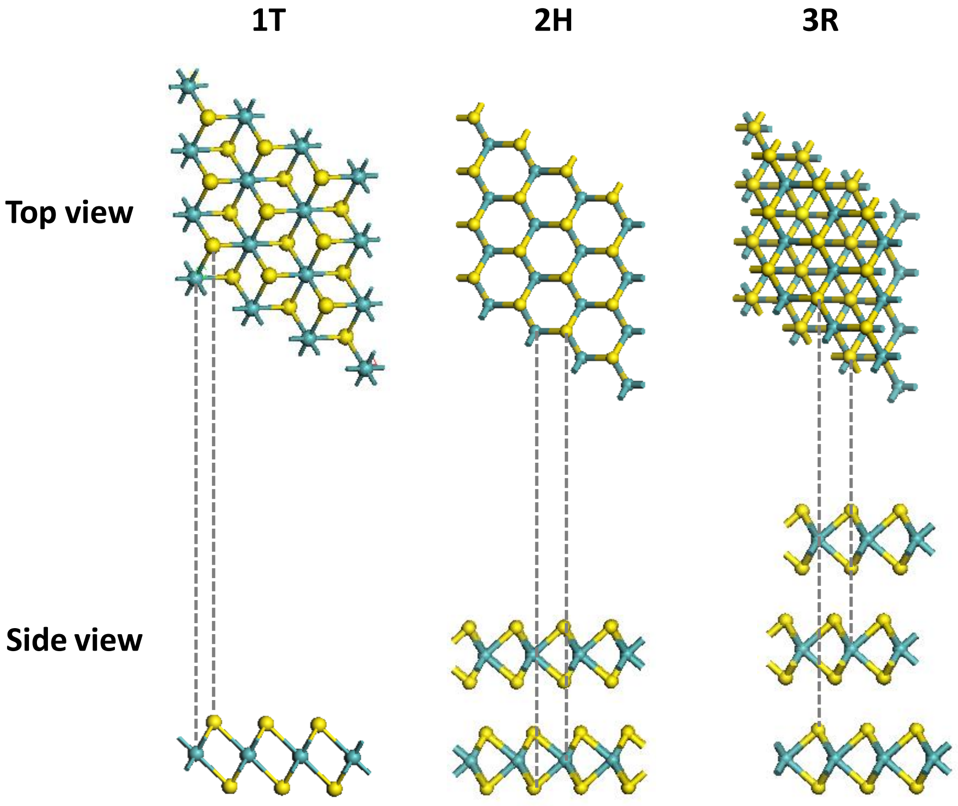

Figure 1.2 *Crystal structures of* MoS_2 *with different phases: (a) 1T, (b) 2H, (c) 3R (left: unit cell; right: 2a×2a polyhedral super cell) [55];*

As shown in Figure 1.2, the 1T-MoS_2 has octahedral coordination of the molybdenum center with one Mo atom in each unit cell [56, 57]; 2H-MoS_2 has trigonal prismatic coordination and two S-Mo-S units per unit cell [42, 43, 48, 49]; 3R-MoS_2 also have the same coordination as its 2H phase with S-Mo-S unit per unit cell [39, 55]. Both the 2H and 3R polytypes have the same lattice parameter a (b=a) with value ~ 3.16 Å [39, 55]. For 1T-MoS_2 phase, the Mo centers are displaced from their ideal positions, as shown in Figure 1.2(a). The 1T phase of MoS_2 is proved to be metallic [58]. By low temperature annealing, the 1T phase of MoS_2 could be modified as 2H phase MoS_2 [58].

1.1.2 The electronic band structures of MoS_2 layers

The previous theoretical calculations demonstrated that the electronic structures of MoS_2 nanosheets highly depend on their number of layers [42, 43, 49]. A crossover exists from indirect band gap for multilayer and bulk MoS_2 to direct band gap for monolayer MoS_2, which has been verified by experiments [17, 59]. The following Figure 1.3 shows the band gap variation of MoS_2 with its number of layers decreasing [42]. It varies from 1.2 eV of bulk phase to 1.9 eV for the monolayer of MoS_2. From Figure 1.3, it can be seen that for bulk MoS_2, the bottom of conduction band is located at Λ point, but the top of valence band is located at the Γ point. Therefore, the thicker MoS_2 is an indirect band-gap semiconductor. When the thickness of MoS_2 nanosheets is decreased to monolayer, both the conduction band minimum and valence band maximum shift towards to the K point, which results in a direct-gap semiconductor [42]. Moreover, in the evolution of band structure in MoS_2, we can see that the electronic states at K point remain the same energy while the energy of electronic states at Γ point decreases when the layer number of MoS_2 is decreasing.

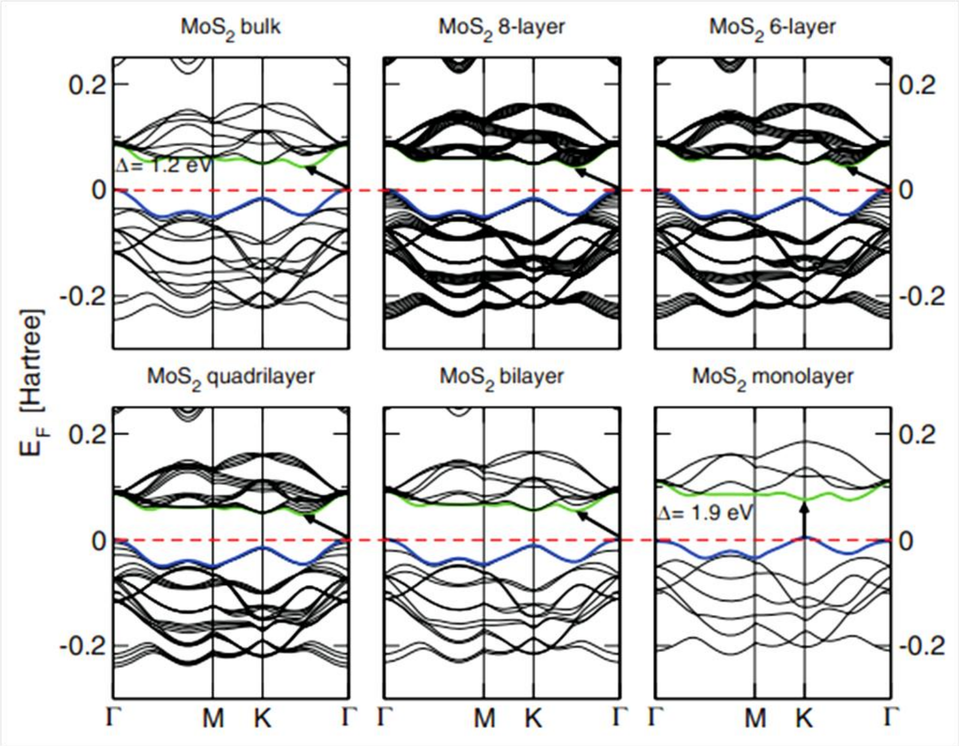

Figure 1.3 *Band structure of MoS$_2$, from single layer to bulk, calculated at the DFT/PBE level. The arrows in each graph show the evolution of bandgap from indirect bandgap to direct bandgap. The red lines represent the Fermi levels. The conduction band minimum and valence band maximum are marked by blue and green lines, respectively [59].*

Such an interesting phenomenon of the band structure displayed in MoS$_2$ is caused by the different components of electronic states at K and Γ points [43, 59]. Electronic states of the valence band maximum at K point are mainly composed by the hybridization of strongly localized *d* orbital of the Mo atom [42, 60]. Since the Mo atoms are sandwiched by two S atoms so they have minimal interlayer coupling and then they have no obvious change when the number of layers varies. While the electronic states at *Γ* point originate from a linear combination of *d* orbital on Mo atoms and anti-bonding *Pz* orbital on S atoms [42, 58, 61]. There are strong couplings between adjacent layers and the energies of their band states highly depend on the number of layers of MoS_2 [59]. The component of band structure at valence band and conduction band could also be resolved by partial density of states (DOS), as shown in Figure 1.4 [42].

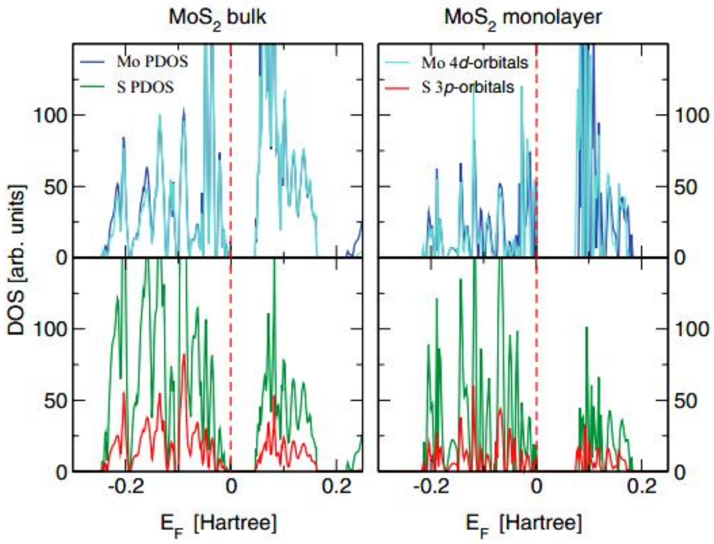

Figure 1.4 *Partial DOS of bulk (left column) and monolayer (right column)* MoS_2 *were calculated by DFT/PBE. The projections of Mo and S atoms are given, respectively, together with the contributions from 4d (Mo) and 3p (S) orbitals. The vertical dashed lines represent the location of the Fermi level [42].*

As discussed above, the experimental evidences have confirmed the theoretical descriptions. Such an evolution of electronic structures can be confirmed by the absorption spectra and PL spectra from band-edge emissions [17, 60, 62]. The PL intensity of monolayer MoS_2 is several orders of magnitude (quantum efficiency) higher than that of bulk MoS_2. Usually, for indirect bandgap semiconductors, the optical transitions will involve phonons or defect-scatterings to satisfy the momentum conservation. The PL quantum yield of single layer MoS_2 was found to be 10^4 fold compared with that of bulk MoS_2. The high PL quantum yield pushes monolayer MoS_2 as ideal candidates for optical emitters, solar cells, and other opto-electronic devices [63-65].

1.1.3 The phonon dispersion of MoS_2 layers

The lattice vibrations could be classified by the irreducible representation of the symmetry group of the crystals [48]. Bulk MoS_2 has D_{6h} point group symmetry. In few layer MoS_2, due to the translational asymmetry along the z axis, symmetry is reduced [47, 48, 61, 66]. We summarize the characters of the phonons for both the bulk (2H phase) and monolayer MoS_2 in Figure 1.5(a) with respect to the symmetry assignment, frequency, optical character, and eigenvectors [19, 48, 66]. Since the primitive cell of 2H-MoS_2 and monolayer MoS_2 contains 6 and 3 atoms, there are a total of 18 and 9 phonon modes, respectively. A group analysis of the point group (D_{6h} and D_{3h} for 2H-MoS_2 and monolayer MoS_2, respectively) shows that the optical phonon modes at the Γ point in the long-wavelength range (without the three translational acoustic modes) can be decomposed as:

$$\Gamma(\mathrm{Bulk}) = \mathrm{A_{1g}(R) + 2A_{2u}(IR) + 2B_{2g}(IN) + B_{1u}(IN) + E_{1g}(R) + 2E_{1u}(IR)}$$

$$\mathrm{+2E_{2g}(R) + E_{2u}(IN)}; \tag{1.1}$$

$$\Gamma(\mathrm{Monolayer}) = \mathrm{A_1^{'}(R) + A_2^{''}(IR) + E^{'}(IR + R) + E^{''}(R)}; \tag{1.2}$$

R, IR, IN mean Raman, infrared, and inactive modes, respectively. The A_{2u}, A_{1g}, B_{2g}, B_{1u}, A_2'', A_1' modes are singly degenerate and the E_{1u}, E_{2g}, E_{1g}, E_{2u}, E', E'' modes are doubly degenerate.

The density functional theory within the local density approximation (LDA) is applied to calculate the phonon dispersions of monolayer and bulk MoS_2, as shown in Figure 1.5(b) and (c) [66]. It is found that, phonons away from the Γ point are dispersive with respect to wave-vector q. There are three acoustic branches: transverse acoustic (TA), longitudinal acoustic (LA), and out-of-plane transverse acoustic (ZA) branches. The TO_1 and LO_1 modes are non-polar transverse optical (TO) and longitudinal optical (LO) modes, respectively. The TO_2, LO_2, and ZO_1 modes are three polar branches [66]. The homopolar ZO_2 branch shows a non-dispersive behavior, accompanied by a breathing mode eigenvector (see $A_1{}'$ mode in Figure 1.5(b)).

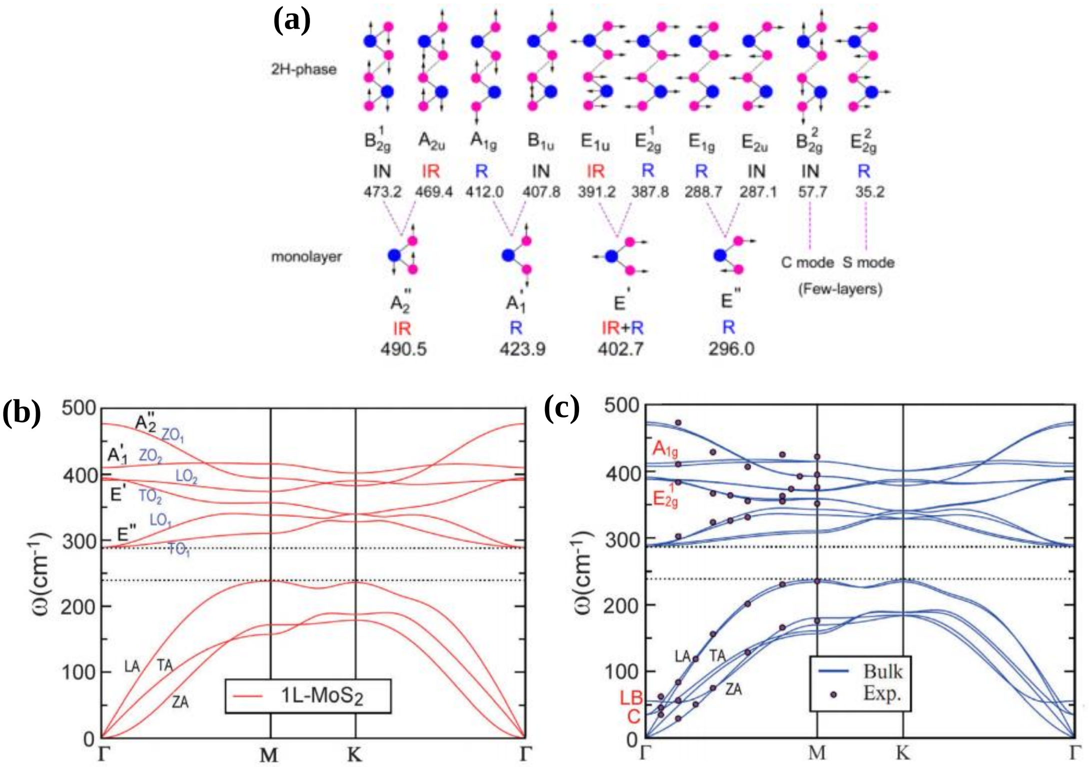

Figure 1.5 (a) Comparison of the zone-center modes between 2H-MoS_2 and monolayer MoS_2. The frequencies of the 2H phase are adopted from Ref. [66]. Phonon dispersion of monolayer (b) and bulk (c) MoS_2 are shown. The polarization of all the phonon branches is presented.

In polar semiconductor or insulators, each IR active mode (polar mode) displays the

LO / TO splitting due to the coupling of the lattice to the polarization field generated by the polar mode in the long-wavelength limit. For bulk 2H-MoS_2, the Born effective charges (BEC) of Mo and S are small [67] and the polarized fields associated with the two IR modes (A_{2u} and E_{1u}) are weak (only leading to a 2 cm^{-1} LO/TO splitting [68]) due to a small mode oscillator strength [69, 70]. For monolayer MoS_2, the electronic screening is weaker than its bulk phase and the splitting will be even smaller and thus could be neglected here.

1.2 Introduction to Raman spectroscopy

When a sample is illuminated by light, a fraction of the incident light is reflected and the rest is transmitted at the surface of the sample. While inside the sample some of the light could be absorbed or scattered, as shown in Figure 1.6. For the absorbed light, some of them may reemit a light with a different frequency, known as PL.

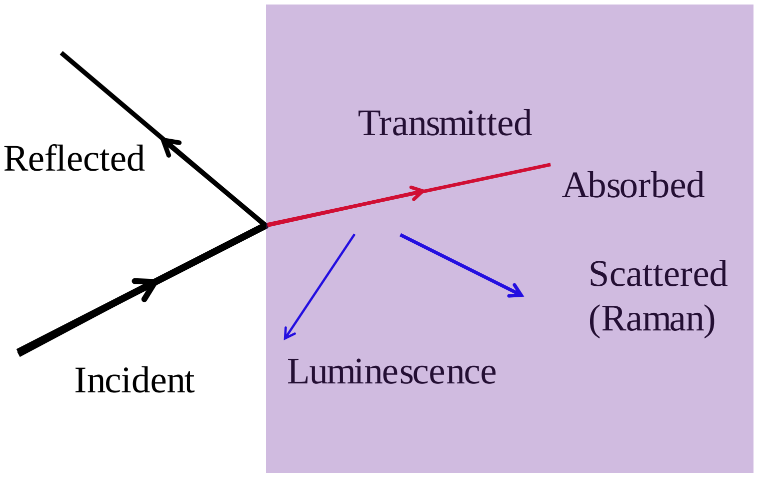

Figure 1.6 *Schematic diagram shows the possibly optical processes when a sample illuminated by light.*

Besides PL, other transmitted light inside the medium are scattered and the scattering process includes two different cases: elastic scattering process and inelastic scattering process. The elastic scattering process means that the frequency of scattered electromagnetic wave is the same as that of the incident photon, which is named as Rayleigh scattering. In the latter case, the frequency of the scattered light is larger (anti-stokes scattering) or smaller (stokes scattering) than that of the incident light, which is called Raman scattering phenomenon.

Actually, since the Raman spectroscopic technique was observed in 1927 for the first time, it has been employed as one of the main spectroscopic techniques to probe vibrations of atoms or molecules, which could provide information on chemical structures and physical forms to identify the properties of substances from the "fingerprinting" spectrum [71, 72]. In 1930, Sir C.V. Raman received the Nobel Prize in Physics for the discovering of Raman scattering, which describes how matter interacts with the incident laser light and it scatters photons with wavelength different from that of the incident photons. Moreover, the inelastic scattering of light actually had been theoretically predicted in 1923 by A. Smekal [73], therefore, sometimes Raman scattering process is also referred as Smekal-Raman effect.

In this part, we will introduce the basic concepts of Raman scattering and related literature reviews on Raman spectroscopy studies of MoS_2 layers.

1.2.1 Classical and quantum descriptions of Raman scattering

Light is, actually, an oscillating electromagnetic field. When light interacts with a molecule, the charges of the molecule (electrons and nuclei) move in the opposite directions in response to the driving potential. Thus, the molecule becomes itself an emitter of electromagnetic radiation. The magnitude of such an effect must be proportional to the induced dipole of the molecule. The relationship between the electrical field and the induced dipole moment can be expressed as follows:

$$P = \alpha \cdot E + (1/2) \cdot \beta \cdot E^{2} + (1/6) \cdot \gamma \cdot E^{3} \cdots \qquad (1.3)$$

α, β and γ are tensors, which are called as polarisability, hyper-polarisability and 2nd hyper-polarisability, respectively [74, 75]. Typically, their magnitudes are in the range of $\alpha \sim 10^{-40}$ C V^{-1} m^{2}, $\beta \sim 10^{-50}$ C V^{-2} m^{3},and $\gamma \sim 10^{-60}$ C V^{-3} m^{4}, respectively. Thus the influence of the latter two factors can be neglected in many cases.

Therefore, the equation (1.3) could be re-expressed as:

$$P = \alpha \cdot E \qquad (1.4)$$

In a first approximation, α is a constant, so the direction of electrical field vector E is the same as that of the induced dipole moment.

As discussed above, the electrical field results from the electromagnetic radiation. Supposing the monochromatic radiation of frequency v_0, the electrical field vector **E** could be described as:

$$E = E_0 \cdot \cos(2\pi \cdot v_0 \cdot t) \qquad (1.5)$$

By substituting equations (1.5) in the dipole moment ***p*** (equation (1.4)), we could obtain:

$$P = \alpha E_0 \cos 2\pi \upsilon_0 t \qquad (1.6)$$

the polarisability α is usually dependent on the dimensions and shape of the chemical bond et al. It can be said that α depends on the normal coordinate of the molecule. Thus, the polarizability α with vibrations of the molecules could be expressed as follows:

$$\alpha = \alpha_0 + \sum \alpha_n \cos 2\pi\upsilon_n t \qquad (1.7)$$

a_0 is a constant, and the second part means the sum of a typical molecule vibration with various normal frequency. α_n represents the n_{th} normal frequency, which can be the vibration frequency or the rotation frequency, and could also be the vibration frequency of lattice or phonon scattering frequency.

Thus

$$P = E_0\alpha_0 \cos 2\pi\upsilon_0 t + E_0 \sum \alpha_n \cos 2\pi\nu_0 t \cdot \cos 2\pi\nu_n t \qquad (1.8)$$

By using the trigonometrical formula:

$$\cos A \cdot \cos B = {}^{1}\!/_{2} [\cos(A + B) + \cos(A - B)] \qquad (1.9)$$

It can be deduced that the equation (1.8) could be expressed as:

$$P = E_0\alpha_0 \cos 2\pi\upsilon_0 t + \frac{1}{2} E_0 \sum \alpha_n [\cos 2\,\pi(\nu_0 - \nu_n)t + \cos 2\pi(\nu_0 + \nu_n)\,t] \qquad (1.10)$$

Therefore, the induced dipole moment could be considered as a function of the vibrational frequencies of the molecules (ν_n) and the incident radiation (ν_0)

$$P = P(\nu_0) + P(\nu_0 - \nu_n) + P(\nu_0 + \nu_n) \qquad (1.11)$$

The first item $P(\nu_0)$ represents the moments of oscillating dipole emitting with the same frequency ν_0 as that of the incident field (Rayleigh scattering). The second item ($P(\nu_0 - \nu_n)$) and the third item ($P(\nu_0 + \nu_n)$) represent the emitting frequencies modulated by the frequency of the excited vibration. When the emitting frequency is lower than that of the incident light, it is stokes Raman scattering process, otherwise, it is an anti-stokes Raman scattering.

Furthermore, according to the classical theory of electromagnetism states that an oscillating dipole emits radiation of the intensity

$$I = \frac{\nu^4}{12\pi\varepsilon_0 c^3}|p|^2 \tag{1.12}$$

Thus, the intensities of ratio between stokes and anti-stokes scattering should be expressed theoretically as follows:

$$\frac{I(\mathrm{Stokes})}{I(\mathrm{anti-Stokes})} = \frac{(\nu_0 - \nu_n)^4}{(\nu_0 + \nu_n)^4} \tag{1.13}$$

This is not in correspondence with experimental results, which is one of the failures of the classical picture. Therefore, when considering the intensities of scattering, it will be understandable when considering the quantum-treatment of the Raman effect, which is given in next section.

As discussed above, the classical theory of the Raman scattering fails, because the intensity of Stokes Raman scattering is stronger experimentally than that of the anti-Stokes Raman scattering. In the quantum mechanics theory, the molecular state could be express by the wave function and its energies are several discrete energy levels. When the molecule interacts with light, one or more vibration modes of the molecule would be excited and the transitions occur between the excited vibration energy levels, as shown in Figure 1.7. Supposing the Stokes Raman begins with a level having a small vibrational quantum number ν_0 (in particular $\nu_0 = 0$) and ends with a level having a higher quantum number ν_k (for example $\nu_k = 1$). Otherwise, the reverse process with quantum number $\nu_k < \nu_0$,is called anti-Stokes effect.

When the energy of the exciting light is the same or near the energy of an electronic absorption band of the measured sample, the intermediate state is a real rather than a virtual state (normal Raman spectroscopy case), and the resonance Raman spectroscopy occurs. Resonance Raman spectroscopy depends on the observation of the Raman spectrum at various incident laser frequencies. The peak frequencies generally do not depend on incident frequency as they are properties of the ground electronic state; however, the relative intensities of Raman modes vary as the excitation laser is tuned across the electronic absorption band. Most vibrational modes which display strong intensities in the resonance Raman spectrum derive their intensities from a geometry change of the molecule in the excited electronic-state, and the intensities of resonance Raman can be enhanced by a factor of 10^3 to 10^5 when compared with normal Raman band transition.

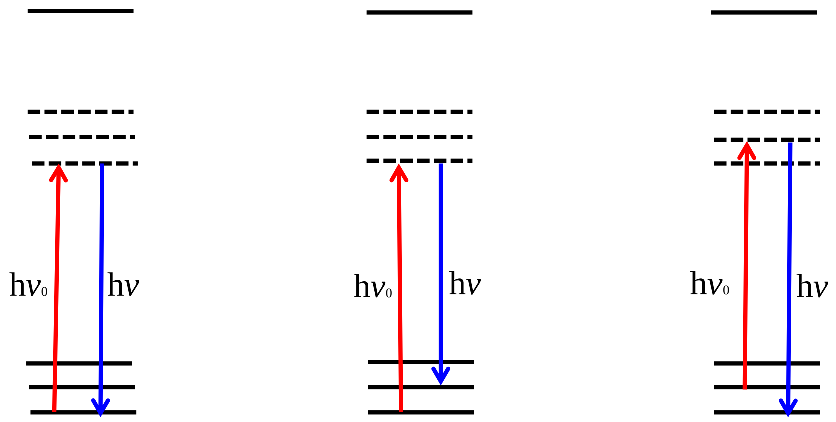

(a) Rayleigh scattering (b) Stokes scattering (c) Anti-Stokes scattering

Figure 1.7 *Schematic diagram of the quantum transition processes: (a) Rayleigh scattering* $(h\nu = h\nu_0)$*; (b) Stokes scattering* $h\nu = h\nu_0 - h\nu_k)$*; (c) Anti-Stokes scattering* $h\nu = h\nu_0 + h\nu_k$.

In the quantum mechanical model, the intensity of scattering depends on the occupation of the initial state. This is determined by the Boltzmann distribution. Thus the scattering intensity ratio is [76]:

$$\frac{\mathrm{I(Stokes)}}{\mathrm{I(anti{-}Stokes)}} = \frac{(\nu_0-\nu_k)^4}{(\nu_0+\nu_k)^4} e^{hc\nu_k/kT} \qquad (1.14)$$

The ratio depends on the temperature T. Therefore one can determine the temperature of the sample by considering the intensities of both the Stokes scattering and the corresponding anti-Stokes scattering. The temperature is given by the formula:

$$T = \frac{-\nu_k \times 1.43879}{\left[\ln\left\{\frac{\mathrm{I(anti{-}Stokes)}}{\mathrm{I(Stokes)}}\right\} + 4\ln\left\{\frac{\nu_0-\nu_k}{\nu_0+\nu_k}\right\}\right]} \qquad (1.15)$$

1.2.2 Selection rules in Raman spectroscopy

As discussed above, in equation (1.4), the induced moment is related to the field strength of the incident light. For a normal mode, if it is Raman active, there must be a nonzero change in the polarizability (α) with the normal coordinate at the equilibrium configuration; $(\partial\alpha/\partial Q)_0 \neq 0$.

The polarizability is best expressed as a tensor, equation (1.4) becomes[76]:

$$\begin{bmatrix} P_x \\ P_y \\ P_z \end{bmatrix} = \begin{bmatrix} \alpha_{xx} & \alpha_{xy} & \alpha_{xz} \\ \alpha_{yx} & \alpha_{yy} & \alpha_{yz} \\ \alpha_{zx} & \alpha_{zy} & \alpha_{zz} \end{bmatrix} \begin{bmatrix} E_x \\ E_y \\ E_z \end{bmatrix}$$

where $\alpha_{ij} = \alpha_{ji}$.

If the change in any one of the these components is nonzero $\left[(\partial\alpha_{ij}/\partial Q)_0 \neq 0\right]$ the mode will be Raman active, otherwise, it will be Raman inactive.

1.2.3 Raman spectra of MoS_2 layers

Since the band structures of MoS_2 nanosheets are highly dependent on its number of layers, the determination of its number of layer becomes very important for further exploring its properties and potential application. In this section, we introduce the non-resonant and resonant Raman spectra of MoS_2 nanosheets and investigate how the Raman modes depend on the number of layer of MoS_2 nanosheets.

(1) Non-resonant Raman spectra of MoS_2 layers

Raman spectroscopy has been widely used as an accurate, versatile and non-invasive technique of thickness characterization for 2D layered materials [18, 77-81]. For MoS_2, under off-resonance condition, four first-order Raman active modes are observed with frequencies of 32 cm^{-1} (E_{2g}^2), 286 cm^{-1} (E_{1g}), 383 cm^{-1} (E_{2g}^1) and 408 cm^{-1} (A_{1g}) in bulk MoS_2. The origin of E_{2g}^2 mode is the vibration of a S–Mo–S layer against adjacent layers [82, 83]. The E_{1g} mode is forbidden on a basal plane in the back-scattering experiment according to its Raman tensor [84]. The E_{2g}^1 mode (in-plane) is led by the two S atoms with opposite vibration to Mo atom and the A_{1g} mode (out-of-plane) origins from the vibration of two S atoms towards opposite directions with Mo atom stationary [82, 83]. The frequencies of these two Raman modes highly depend on the number of layers of MoS_2. But the denotations of these modes are different in monolayer and bulk MoS_2 due to their different symmetries [47, 48, 66]. We simply discuss the Raman modes of E_{2g}^1 and A_{1g} here, as these two modes are widely used to identify the number of layer of MoS_2 in the literature [18, 48, 80, 85]. The number of layer (N) dependent frequencies for E_{2g}^1 and A_{1g} modes of MoS_2 nanosheets is shown in Figure 1.8(a). The E_{2g}^1 and A_{1g} modes show the opposite variation trends with the decreasing thickness of MoS_2 nanosheets. Based on the classical model for coupled harmonic oscillators, both of the frequencies of these two modes would stiffen in bulk when compared with that of 1L MoS_2 because the interlayer vdW interactions increase the effective restoring forces acting on the atoms. But the E^1_{2g} mode becomes strong with the number of layers increasing. This unexpected trend of E^1_{2g} mode indicates that not only the van der Waals forces exist in MoS_2 nanosheets since this classical model only consider the van der Waals interactions [18, 48]. The previous works attributed this abnormal trend of E^1_{2g} mode to the long-range Coulomb term, which decreases dramatically in the bulk MoS_2 due to the dramatical increase of the dielectric tensor [48].

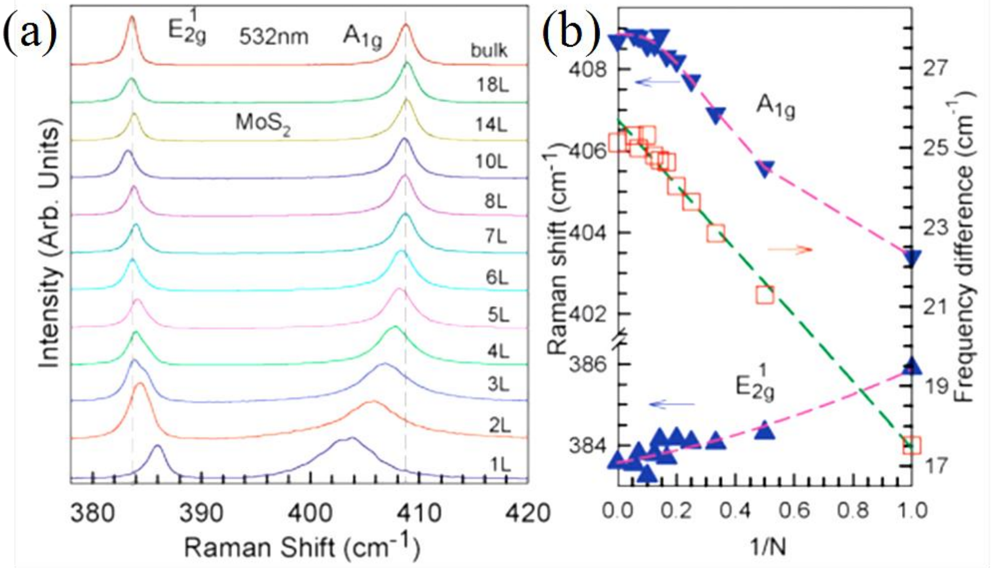

Figure 1.8 *(a) Raman spectra of MoS_2 nanosheets when excited by 532nm laser lines, including 1L, 2L, 3L, 4L, till bulk phase. Two vertical lines show the frequencies of E^1_{2g} and A_{1g} modes for bulk MoS_2. (b) Frequencies of E^1_{2g} and A_{1g} mode and the frequency difference between them as a function of reciprocal of N. N represents the layer number of MoS_2 nanosheets [47].*

(2) Resonant Raman spectra of MoS_2 layers

Figure 1.9 presents the resonant Raman spectra of MoS_2 with different number of layers. It is obvious that some new Raman modes are observed in the resonant spectra of MoS_2 due to strong electron–phonon couplings [80, 85]. The extra Raman frequencies are ~178cm^{-1} (A_{1g}(M)–LA(M)), ~420cm^{-1} (B_{2g}^2 + E_{1u}^2(Γ-A)), ~465cm^{-1} ((2LA(M) (~450cm^{-1}) and A_{2u}(Γ) (~465cm^{-1})), ~572cm^{-1} (2E_{1g}(Γ)), ~600 cm^{-1} ((E_{2g}^1(M) + LA(M))) and ~643cm^{-1} (A_{1g}(M) + LA(M)) [80, 83, 85-87]. Moreover, a mode marked as 'c' (~377 cm^{-1}) could be clearly identified from the E_{2g}^1 mode. As shown in Figure 1.9, in the Raman spectrum of single layer MoS_2, this mode is a little broad but it becomes sharp for MoS_2 layers with n≥2 cases. This mode is belonged to the transverse optical (TO) branch (Δ6 branch along c axis [87-89]) with a wave vector near the Γ point. Some previous work assigned this peak as the E_{1u}^2 symmetry [87]. However, from the IR spectra of MoS_2, the position of the E_{1u}^2 mode was found on the higher-energy side of the E_{2g}^1 mode [82]. Therefore, this mode cannot be assigned as E_{1u}^2 mode. Another mode in the resonant Raman spectra of MoS_2 appears at ~ 409 cm^{-1}, which is assigned as B_{1u} symmetry in bulk MoS_2 [87, 88]. This Raman inactive mode only appears under resonance condition and it is the Davydov couple of the A_{1g} mode [90]. An additional Raman mode near 230 cm^{-1} is observed for n≥2 cases. From lattice dynamic calculations [91], this mode can be identified as the first order LA(M) mode. This mode had been reported by Freyet al. for MoS_2 nanoparticles [86] and was attributed as disorder-induced scattering from the zone edge M point. This assignment has been demonstrated experimentally in inelastic neutron scattering [28], and a new peak near 230 cm^{-1} was shown in the phonon density of states. Therefore, this mode in a few MoS_2 layers could be used to predict the structural defect-induced scattering. In the high wave number, the modes with frequency at 526 cm $^{-1}$ (E_{1g}(M) +LA(M)) was shown in bulk MoS_2, where the mode assignments were studied by previous reports [86]. The new bands (not seen in bulk MoS_2) are clearly observed in samples with n≥2 cases in respect of the bulk MoS_2 are: ~ 554 cm^{-1} (marked as Q in Figure 1.9), 588 cm^{-1} (P) and 628 cm^{-1} (S). However, the assignments of these three peaks remain unknown [85].

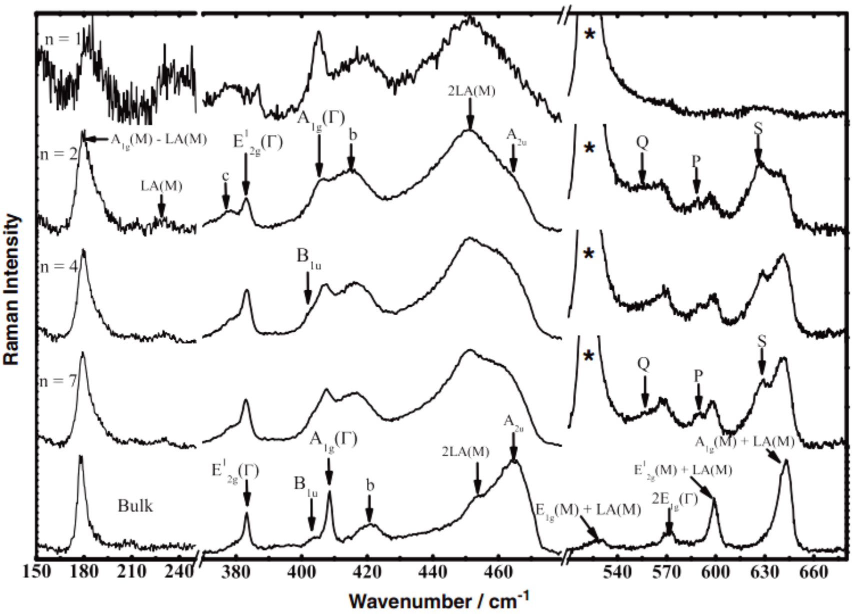

Figure 1.9 *Resonant Raman spectra of MoS_2 with different number of layers (n), under the excitation of 633nm laser line. The Raman mode marked * in figure origins from the SiO_2/Si substrate and thus this peak is completely absent in the spectrum of bulk MoS_2 due to the finite penetration depth [85].*

1.3 Introduction to PL spectroscopy

1.3.1 Mechanism of PL

Photoluminescence spectroscopy, similar to Raman spectroscopy, is a contactless and nondestructive technique to probe the electronically energy structure of materials. In a photo-excited emission process, electron-hole pairs are produced when the sample is excited. They would reach the quasi-thermal equilibrium faster than the time it takes for the recombination of electrons and holes if the electrons and holes are thermalized among themselves. However, these electrons and holes often have different quasi-equilibrium distributions. They can recombine radiatively, and produce the spontaneous emission. In general, as shown in Figure 1.10, a typical PL process should involve the following three steps:

(1) Excitation: electron-hole pairs generated by the excitation from an external light.

(2) Thermalization: The excited electron and hole pairs relax towards the quasi-thermal equilibrium distributions.

(3) Recombination: The relaxed electron-hole pairs recombine radiatively and the emission is produced.

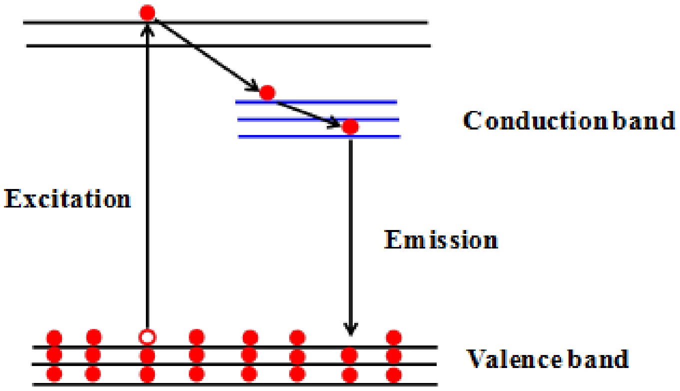

Figure 1.10 *Schematic diagram of emission process with the typical three steps [92, 93].*

As discussed above, the PL spectroscopy could provide direct information on the electronic structure of the detected material. Photons with particular energy that are absorbed by sample provide evidence of the electronic structure of the samples. For a perfect semiconductor, electron-hole pairs could thermalize and accumulate at the conduction band minimum and the valence band maximum, and they recombine with an emission, as shown in Figure 1.11(a). If the impurity is introduced in semiconductor materials, the defect energy levels would form near the conduction band or valence band. Depending on the type of impurities introduced, they could act as donor or accepter of electrons in crystals. Then these defects energy level could attract the local charge because of the impurity nucleus or defects, as shown in Figure 1.11(b) and (c). If these trapped electron and hole pairs could recombine radiatively, the emitted energy could represent the energy level of the defects or impurity. The deep level, as shown in Figure 1.11(d), tends to play a stop-over role in making electron transition from conduction band to valence band and thus facilitate nonradiative recombination process.

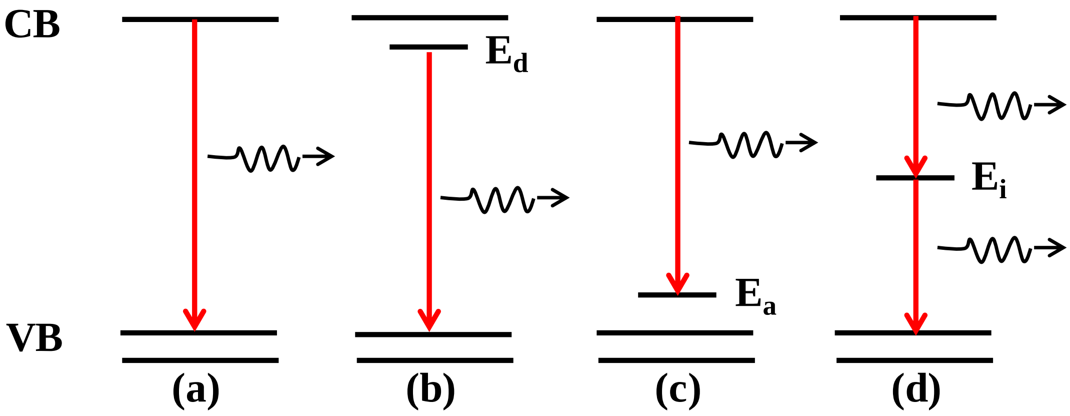

Figure 1.11 *(a) band-to-band recombination via radiative paths; (b) donor to valence band and (c) conduction band to acceptor via radiative paths. (d) non-radiative recombination via an intermediate state.*

Ideally, the photo-excited electron and holes are expected to bind each other by Coulomb interaction and then they form excitons. Meanwhile, due to the radiative annihilation of excitons, the free exciton peak appears in the emission spectra. If a certain number of donors and acceptors were doped into sample, the excitons generated could be attracted to the location of these impurities via van der Waals interaction. In general condition, these impurity energy levels are shallow level and lies near the edge of conduction or valence band, they are efficient to trap excitons to from bound excitons at low temperature.

(1) Free exciton emission

The free excitons have larger radiuses and they are delocalized states which can move freely throughout the crystal. Thus the binding energy of free exciton is very small, with typical values ~0.01eV. Since $k_B T$ (~0.025 eV at room temperature) means the maximum energy of a thermally excited phonon at temperature T, where k_B is Boltzmann's constant [94]. So the free exciton is not stable at room temperature. Moreover, they seldom could be observed except in very pure samples. Because the impurities release free electrons and holes which can screen the Coulomb interaction in the exciton and thus reduce the binding forces and then the charged impurities could generate electric fields and ionize the excitons.

(2) Bound exciton emission

The bound excitons have a smaller size when compared with the size of the unit cell, which make their localized states tightly bound to specific atoms. Thus, the binding energy is larger (~0.1-1eV) than that of free exciton, which makes them stable at room temperature. Compared with free excitons, the bound excitons are not "free" to move through the crystal but they can hop from one site to another site.

(3) Trion

Charge exciton-electron complex (trions) was predicted in 1958 [95] and experimentally found in CdTe based quantum well structures in 1993 [96]. A negative trion consists of two electrons and one hole and a positive trion consists of two holes and one electron. When the presence of free electrons is residual in semiconductors, excitons could interact with the surrounding charges and binding together to form charged excitons [95-97]. Trions in monolayer MoS_2 are stable at room temperature due to their remarkably large binding energies, with a larger binding energy (~ 20 meV) nearly an order of magnitude when compared with that in other materials [98-100]. The reason for such a giant binding energy is due to the greatly enhanced Coulomb interactions in monolayer MoS_2, which is a consequence of reduced dielectric screening in confined two dimensional crystals and the relatively heavy carrier band masses associated with the Mo *d*-manifolds [98].

1.3.2 PL spectroscopy of MoS_2 layers

As mentioned above, MoS_2 becomes a direct bandgap material when the number of layer decreases to monolayer from bulk. So the PL intensity in single layer MoS_2 is expected to be stronger than that of multilayer MoS_2 samples. Mak et al, and Splendiani et al, first showed the PL spectrum of monolayer, bilayer and few layer MoS_2 nanosheets [17, 59].

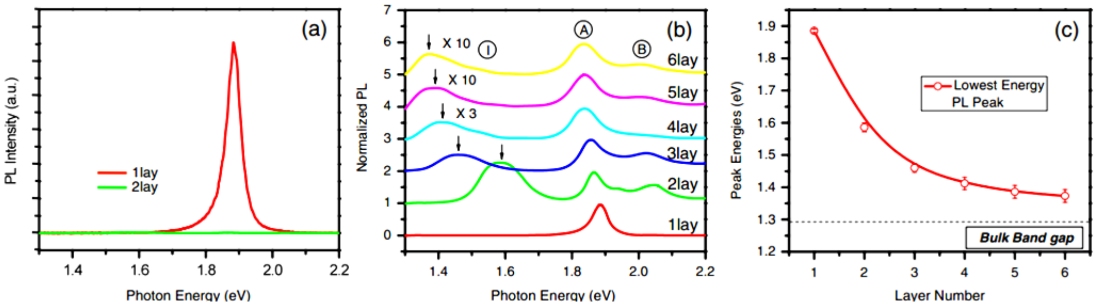

***Figure 1.12** (a) PL spectra for single layer and bilayer MoS_2 samples; (b) Normalized PL spectra of MoS_2 layers (for n=1–6) with normalization by the intensity of peak A; (c) Bandgap energy of MoS_2 layers for n= 1–6, inferred from the energies of the PL peaks shown in Figure (b). The dashed line shows the value of indirect bandgap of bulk MoS_2 [17].*

As presented in Figure 1.12, the PL spectra of MoS_2 nanosheets with different thicknesses were investigated. We can observe that the PL intensity from 1L MoS_2 is very strong when compared with that of bilayer samples (Figure 1.12(a)). Figure 1.12(b) shows that the PL spectra of MoS_2 when its number of layers varies. The origins of the A, B peaks observed are widely accepted as the spin orbital splitting (SOS) at the top of valence band, as shown in Figure 1.13 [17]. The peak I is attributed to the indirect bandgap recombination reduced emission. It is observed that from Figure 1.12(c) that the position of PL peak "I" is obviously dependent on the layer number of MoS_2, and thus these peaks could also be used to identify the number of layer of MoS_2 nanosheets. But for the origin of this indirect bandgap recombination process, there is a little debate on it [42, 43, 101, 102]. Then the origin of this indirect bandgap transition is confirmed by subsequently researchers [103, 104], as shown in Figure 1.13.

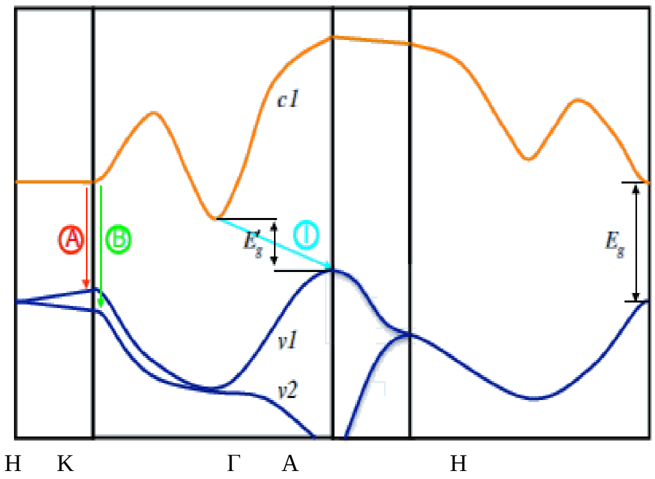

Figure 1.13 *Band structure of MoS_2. The SOS is shown at K point. E_g is the band gap for single layer MoS_2 and Eg' is the bandgap for bulk MoS_2 [17].*

Although the bandgap of single layer MoS_2 calculated by density functional theory (DFT) is ~1.9eV, which seems match with the experimentally energy of PL emission well [17, 42]. However, this method fails to describe photoemission since the Kohn-Sham energies do not formally correspond to quasi-particle energies. Ramasubramaniam et al. combine many-body GW and BSE calculations to correct the quasi-particle band structures and optical properties of single layer MoS_2 [105]. The confirmed bound exciton in single layer MoS_2 is shown in excellent agreement with experimental results [106, 107]. The previously experimental studies reported that the direct band to band transitions dominant the optical transition in MoS_2. In this case, the recombination process is directly related to the electronic bandgap and the PL peak position could represent the bandgap of MoS_2. When we consider the excitonic effect, as reported in the previous studies, the photon-excited electrons and holes were bonded each other by Coulomb interactions and form excitons. If the binding energy is higher enough when compared with the environmental perturbations, PL spectrum would have pronounced excitonic features. Especially, in such a 2D material, Coulomb interactions are dramatically enhanced due to the spatial confinement and the reduced dielectric screening [108]. Therefore, the excitonic effects will dominate the optical properties of MoS_2 nanosheets.

Besides the excitonic effects observed in theoretical calculations and experimental measurement, the electron-bounded excitons, called trions, were also observed in the previous reported PL spectra of single layer MoS_2 [98]. It was reported that the binding energy of the trions in monolayer MoS_2 is ~20meV. Such a giant binding energy affects the trions emission significantly even at room temperature. When the gate-voltage is applied, as shown in Figure 1.14, both the exciton and trion emissions could be identified in the PL and absorption spectrum of doped single layer MoS_2 at room temperature (RT), which are highly dependent on doping concentration. It is obvious that the exciton photoluminescence is highly dependent on the applied gate voltage. The variation of PL spectra is due to a reduction of spectral weight of the exciton emission with electron doping. The gated PL spectra of single layer MoS_2 (10K) was measured but such a strong gate voltage dependent tunability of the exciton PL was not observed, because the exciton emission at low temperature results from hot photoluminescence before exciton-trion reaches equilibrium. While at RT, it is from populations thermally excited from the trion states. Similar phenomena are also observed experimentally [109, 110]. The observation of trion opens a way for the fundamental research on many-body interactions and possible application in optoelectronic and valleytronic field.

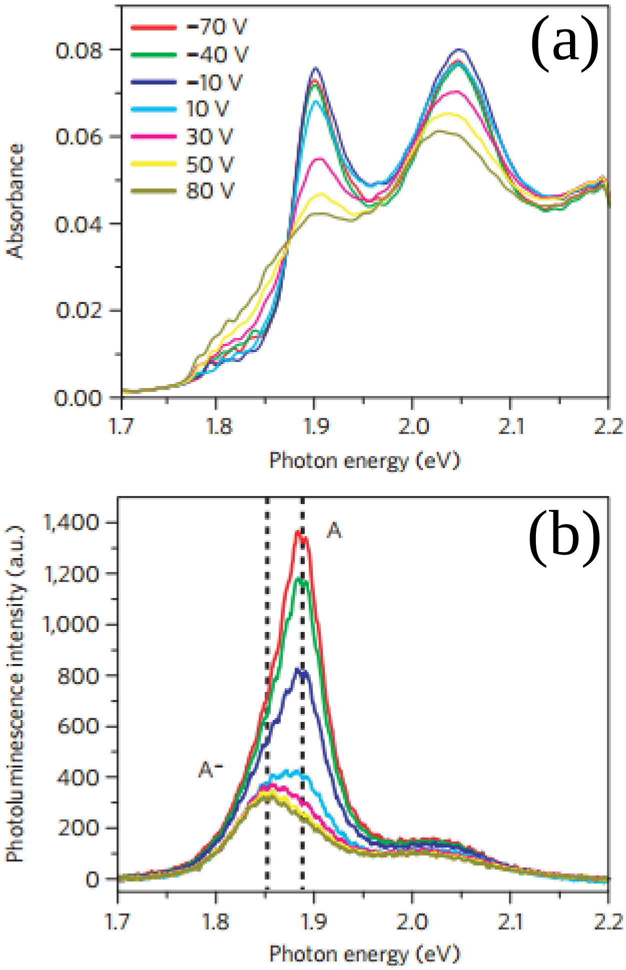

Figure 1.14 *The absorption (a) and photoluminescence (b) spectra of monolayer* MoS_2 *with various back-gate voltages applied. Both the exciton (A) and trion* (A^-) *peaks can be resolved [98].*

1.4 The motivation and organization of this thesis

In this thesis, we presented the fabrication of MoS_2 layers by mechanical exfoliation, and chemical vapor deposition, and investigated the electronic structures of MoS_2 layers by Raman and PL spectroscopy, as well as its application on surface enhanced Raman scattering technique. The motivation of this thesis is as follows:

The absence of natural band gap in graphene prevented its further development on its electronic applications. MoS_2, as a new rising 2D material attracted the attention of researchers, especially for its special physical characters. In order to expand my research objects (not only mechanically exfoliated MoS_2 sample), I have used CVD technique to grow monolayer MoS_2 and got some preliminary results. The samples were characterized using AFM, Raman, PL, X-ray photoelectron spectroscopy, as well as electrical properties, which will be discussed in detail in Chapter 2.

One significant physical characteristic of MoS_2 is the strong spin orbital splitting at the top of valence band, which makes MoS_2 promising for its applications in spin electronics and quantum information processing and so on. Some previous works reported that the energy difference between the two exciton peaks in the PL spectra of MoS_2 is corresponding to the energy of spin orbit splitting. However, the identification of these two exciton emissions is still controversial. Especially for the A exciton emission, its PL intensity could be enhanced dramatically by the introduction of defects, which may identify the PL emission is related to the exciton trapping by defect states. Occasionally, only one PL peak could be detected at the room temperature for single layer MoS_2. Furthermore, the energy difference between these two excitons does not show obvious number of layers dependence, which is conflict with the calculation results on the value of spin orbit splitting. However, till now, there is no an experimental method effectively to detect such an intrinsic spin orbital coupling in MoS_2. While the direct observation of SOS may open a new and convenient way to study the spin physics in MoS_2. In this thesis, resonant Raman technique is used to detect the value of spin orbital splitting since it is very sensitive to the matching between the valence band splitting and the energy of the phonons involved, which will be discussed in Chapter 3.

MoS_2 has been widely investigated in transistors, gas sensors, lithium ion batteries, and hydrogen production, etc. Furthermore, the recent works reported that when MoS_2 exposed to triethylamine, it could be used as a chemical sensor and displays a selective reactivity to a wide range of analytes due to the charge distribution induced by the perturbations on the surface of MoS_2. Therefore, the surface modification plays an important role for the strong interaction between MoS_2 and detected molecules. Some experiments have also been reported to modify the surface activity of substrate, such as nitrogen doping, UV/Ozone oxidized treatment and fluorinate functionalization on graphene oxide. In this work, we observed an improved Raman enhancement of Rhodamine 6G (R6G) molecules deposited on oxygen (argon) plasma treated MoS2 nanosheets, which will be discussed in Chapter 4 in details on the experimental results and mechanism of enhancement.

Recent works reported that the PL intensities of monolayer CVD grown MoS_2 were very strong when compared with that of the mechanically exfoliated sample. The latter one is expected with good crystal quality and should have a strong PL intensity, because various defects, such as point defect, dislocations or grain boundaries, are reported in CVD samples. Therefore, the conclusions reported recently were in opposite to the conventional conclusion that the optical quality at RT could be used to evaluate the crystal quality. Especially, the plasma treated monolayer MoS_2 shows a stronger PL intensity than that of as-prepared sample, which implies that the defects could enhance the intensity of PL emission in monolayer MoS_2. The Chapter 5 will explain the enhancement mechanism in CVD grown MoS_2 samples.

Organization of this thesis: In this thesis, we introduce the especially physical properties of MoS_2 layers. The Raman and PL spectra were introduced first, and the previous reports on the Raman and PL studies of MoS_2 layers in Chapter 1. Then the fabrication methods of MoS_2 layers and the experimental techniques were introduced in Chapter 2. Our preliminary results on the CVD grown MoS_2 samples were also displayed briefly. Followed by that, we introduced the resonant Raman spectroscopy by UV laser excitation in Chapter 3. The giant SOS induced by SOC in monolayer MoS_2 was explored by resonant overtone and combination modes. In Chapter 4, we investigated the probe of defects in MoS_2 by SERS effect and found the defects in single layer MoS_2 facilitated the charge transfer between R6G molecules and defective MoS_2. Chapter 5 compared the PL spectra of mechanically exfoliated and CVD grown monolayer MoS_2 samples. This Chapter explained the reason why the PL intensity of CVD grown MoS_2 monolayer was anomalously strong when compared with that of ME sample.

Chapter 2
Experimental techniques

2.1 Fabrication of MoS_2 layers

Till now, three common methods have been used to fabricate single layer MoS_2, mechanical exfoliation (ME) method [16, 111], chemically exfoliated (CE) method [112-114], and CVD method [115-118]. The following table lists the advantages and disadvantages of three different methods, respectively. In this study, mechanically exfoliation and CVD methods are used.

Methods	Crystal Quality	Yield of Single Layer	Size
ME	Very high	Low	Hundreds of nm to a few μm
CE	Poor	Low	Hundreds of nm
CVD	High	High	A few μm to wafer scale area

***Table 2.1** Comparison of three common fabrication methods of MoS_2 layers. ME means mechanically exfoliated. CE and CVD represent chemical exfoliated and chemical vapor deposition methods, respectively.*

2.1.1 Mechanical exfoliation method

Since the discovery of graphene in 2004 by mechanically exfoliated methods [5, 7], this method displayed by Novoselov *et al.* has been widely employed to get the atomic layer of layered materials, because it is a simple and fast technique.

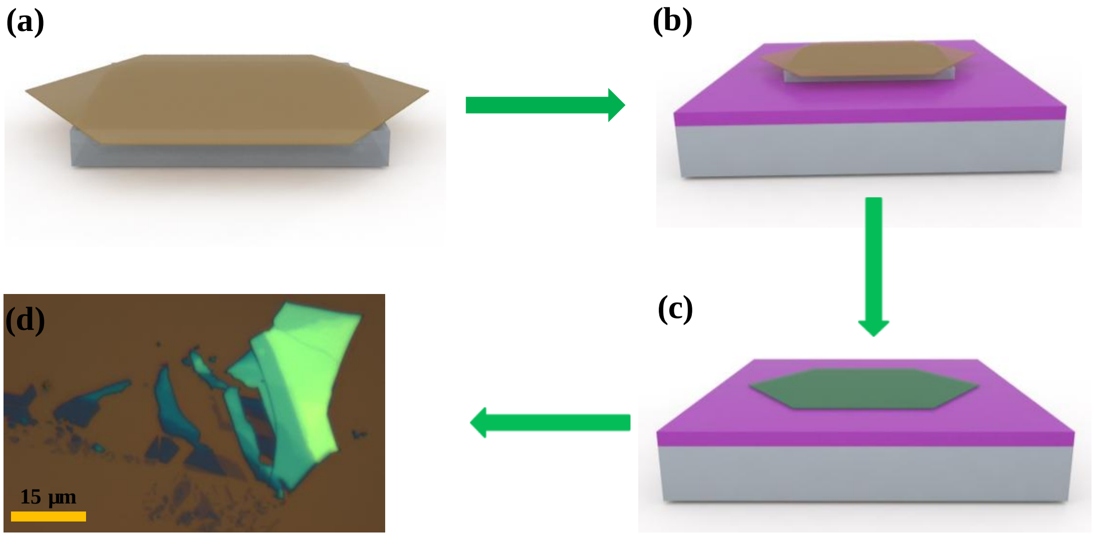

Figure 2.1 *Schematic diagram of fabrication of* MoS_2 *sheets from* MoS_2 *crystal by ME methods. (a)* MoS_2 *nanosheets are peeled off from* MoS_2 *crystal using scotch tape. (b) Stick the tape together with* MoS_2 *nanosheets on a 270 nm* SiO_2/Si *substrate. (c)* MoS_2 *sheets left on the surface of* SiO_2/Si *substrate after the remove of the tape. (d) Optical image of a typical* MoS_2 *nanosheets on a 270 nm* SiO_2/Si *substrate.*

The substrates used in our experiments are silicon substrates covered with 270nm silicon oxide layer. This thickness of silicon oxide gives us a good optical contrast among the MoS_2 nanosheets with different thicknesses. The process of ME technique is schematically shown in Figure 2.1. A thin MoS_2 with hundreds of layers is successively exfoliated from MoS_2 crystal (supplied from SPI) by Scotch tape and then stick the tape onto a 270 nm SiO_2/Si substrate. After removing the tape, MoS_2 nanosheets with different number of layers can be observed on the substrate and visualized under the optical microscope. Figure 2.2(a) shows a typically monolayer MoS_2 sample fabricated by ME methods, and Figure 2.2 (b) is its corresponding atomic force microscopy (AFM) images.

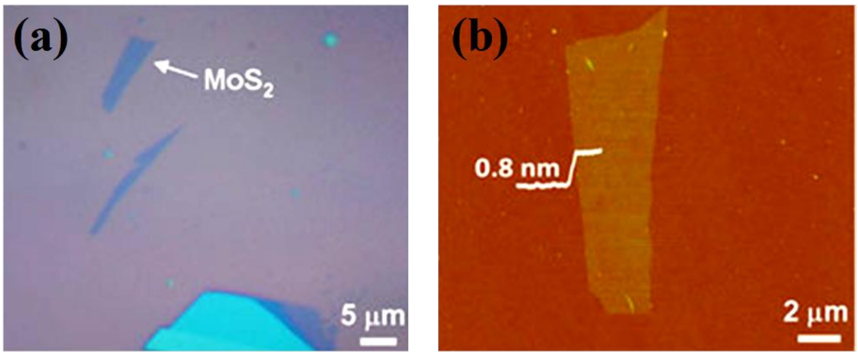

Figure 2.2 *(a) Optical graph of a typical single layer MoS_2 sample fabricated by mechanically exfoliation; (b) The corresponding AFM image of the MoS_2 sample shown in (a) [27];*

2.1.2 Chemical vapor deposition method

In this section, we investigated how the MoS_2 layers can be synthesized by CVD methods. Till now, the CVD synthesis of monolayer MoS_2 could be performed by different sources as the precursor of Mo and S [119-121]. The most used method is that sulphur and MoO_3 powders are simultaneously put into the furnace, with a SiO_2/Si substrate located face-down above the MoO_3 powder as deposition target. Usually the triangular and near-triangular MoS_2 sheets could be obtained by this method, with a domain size from several micrometers to more than one hundred micrometers. Another method used rhomboidal MoO_2 microplates and deposited them on SiO_2/Si substrates first. Then the MoS_2 nanosheets could grow on the substrate under an atmosphere of sulphur at 650-850^{0}C. However, the problem of these methods is the limited domain sizes [122].

Thus, single layer MoS_2 with a larger domain size should be focused on improving the CVD growth of MoS_2 layer to meet the requirement of the practical applications.

It has been demonstrated that the limiting factor for MoS_2 growth on bare SiO_2/Si arises from a complicated nucleation process [120]. The orientations of domains of MoS_2 nanosheets are found to be random, which are most likely modified by the isotropic nature on the surface of substrate: amorphous SiO_2 substrates [120]. Another key factor is the partial pressure (PP) of the reactive gases which could be tuned by tuning the evaporation temperature of S and MoO_3 powder. Therefore, a stable growth environment is critical for the growth of MoS_2 films [123]. Thus the targeted substrate is located face down above the ceramic boat containing MoO_3. This configuration could create a relatively stable environment and provide a high concentration of gaseous MoO_{3-x} precursors for growth of MoS_2 [119]. Yu et al. designed a set-up to get a stable environment with a small quartz tube sealed in a larger one [124]. Recently, a 4-inch high uniform wafer-scale film of monolayer MoS_2 was grown directly on the insulating SiO_2 substrates, with excellent electrical performance over the whole films [125]. The growth process is conducted in a metal-organic chemical vapor deposition (MOCVD) with $Mo(CO)_6$ and $(C_2H_5)_2S$ as the reaction sources, respectively. By controlling the PP of each reactant, the concentration of each reactant could be precisely controlled during the growth. The reason for the growth of large-scale monolayer MoS_2 film with high crystal quality is that MOCVD technique could supply an ideally stable environment by controlling the nucleation density and intergrain stitching.

Another series of CVD growth methods are also reported that Mo(MoOx) based precursors are initially deposited and then sulphurised/decomposed into MoS_2. These methods can be used as an effective technique to prepare large area MoS_2 thin films, but the shortcomings of these methods are difficult to obtain large scale MoS_2 thin films with a uniform thickness, which could be the result of the uncontrollable deposition in terms of the amount and uniformity, and the inefficient sulphurisation on grown substrates. Moreover, the grain boundaries of MoS_2 thin films grown by this method are abundant and complex so they usually have a relatively smaller domain size.

2.1.3 Our preliminary results

(1) CVD grown MoS_2 layers

Our samples were grown using MoO_3 and sulfur as precursor on a clean SiO_2/Si wafer with a 270 nm SiO_2 thickness. The set up of CVD grown technique in our work is shown in Figure 2.3. The MoO_3 powder was well distributed on the surface of one wafer which is placed at the center of a ceramic boat and the targeted wafer was located on the top of the boat with a face-down way. Another ceramic boat filled with sulfur powder was placed near the boat with MoO_3 powder. Considering the different melting point of MoO_3 and sulfur, the sulfur is placed at the edge of the furnace where the temperature of furnace is around the melting point of sulfur when the temperature around center area of furnace reached to the growth temperature of monolayer MoS_2. The furnace was flowed by pure Argon gas at 200sccm for 20min to get a pure Argon atmosphere in furnace and then, during the grown of MoS_2 process, the gas flow was reduced to 20 sccm in order to get a relatively stable environment during the growth of crystal process. During the heating process, the temperature was increased to 500℃

first with a rate of 30℃/min, and reached to 900℃ with a reduced rate at 5℃/min. Then the temperature was sustained at 900℃ for 15min and finally, the furnace was cooled down naturally. The whole grown process is under the atmospheric pressure.

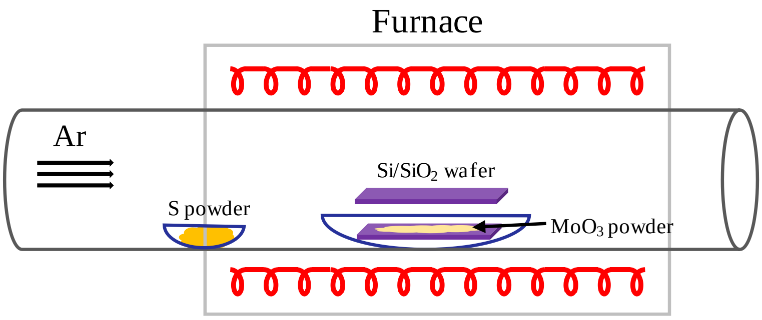

Figure 2.3 *The set-up of the CVD furnace designed in our work. In order to implement the effective sulfidization, the MoO*$_3$ *and S powder were separately placed with suitable temperatures.*

(2) Characterization:

Optical images are taken on a Nikon microscope with a 100 × objective lens. PL spectra with 457 nm as excitation wavelength were conducted on a WITEC CRM200 Raman system with 150 line mm^{-1} grating. Raman mappings were measured on the same system with 1800 line mm^{-1} grating. The thicknesses of MoS$_2$ samples were confirmed by AFM with a tapping mode (Nanoscope II, Digital Instrument-Veeco, USA).

The procedure of device fabrication is as follows: the experiment begins with the SiO$_2$/Si substrates with MoS$_2$ grown on it. Firstly, the photo-resist (AZ5214) is spin coated on the substrate. After baking on hot plate, the electrode patterns are defined by photolithography (including alignment, exposure and developing). Then 5nm Cr and 50 nm Au was deposited by thermal evaporation under high vacuum. After metal deposition, lift-off was carried out by emerging the substrate into acetone. The final step is thermal annealing at 200℃ under a mixture of hydrogen and argon atmosphere to improve the contact performance. Electrical measurements were conducted by HP4156B Precision Semiconductor parameter Analyzer.

(3) Experimental results and characterization

Figure 2.4 displays the experimental results: the optical images of severally typical monolayer MoS_2 samples grown on the prepared SiO_2/Si substrate. Some samples with triangular shape have begun to merge into together. Most samples observed here is with triangular edge. According to Wulff theory, MoS_2 belongs to the hexagonal crystal system, so the samples with triangular, hexagonal, and dodecagonal edge shapes could be observed theoretically [126, 127]. The shape evolution could be from dodecagonal shape to the hexagonal shape, as well as the triangular shape with the variation of formation energy [128]. The latter two cases (hexagonal, and dodecagonal shape) are hard to be formed due to the high formation energy [128]. In Figure 2.4 (e), a typical MoS_2 triangle is observed in the AFM image. The height profile shows that the thickness of the sample is around 0.8nm, which corresponds to the previous reported values [16-18, 59]. The measured thickness of MoS_2 is a little bigger than the theoretical thickness of 1L MoS_2, which is due to the substrate effect [18].

Figure 2.5 (a-c) shows the Raman and PL mapping of a typical CVD grown MoS_2 sample. The Raman mappings were constructed by the integrated Raman peaks E_{2g}^{1}, and A_{1g} respectively, and the PL image (Figure 2.5 (c)) was integrated by the A exciton emission peak. From the Raman and PL mapping, we can observe that the sample is uniform and no additional layer on it. Figure 2.5 (d) shows the single Raman (PL) spectra of MoS_2 excited by 457nm laser line. The monolayer MoS_2 sheet exhibits two prominent Raman peaks: E^1_{2g}, and A_{1g}, at 384.63cm^{-1} and 405.58 cm^{-1}, respectively. The frequency difference between the two prominent peaks is ~20.9cm^{-1}, which is higher than that of ME single layer MoS_2 sample reported [18]. The local strain may contribute to the increase of frequency difference between these two Raman modes. The PL spectrum shows two typical emission peaks marked as A and B peaks.

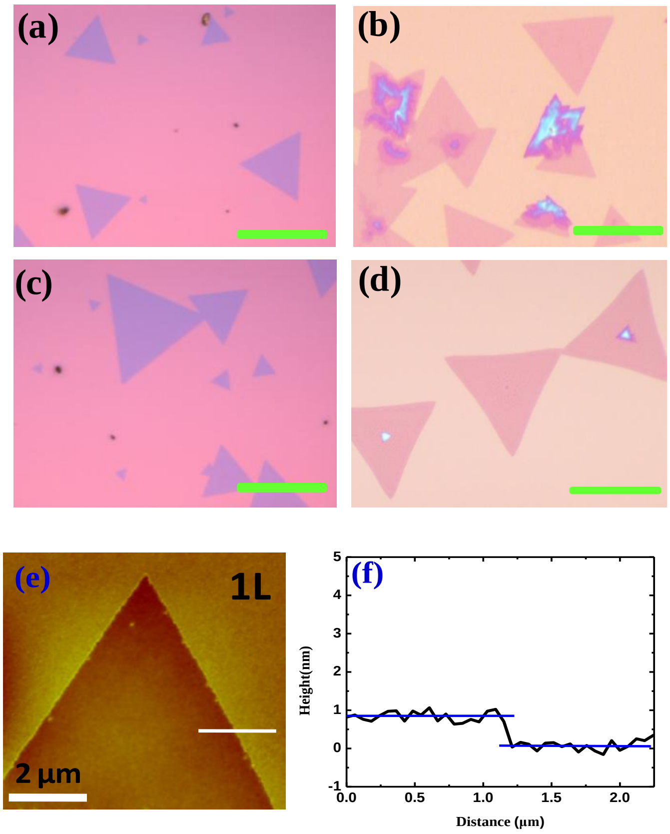

Figure 2.4 *(a-d) Several optical images of monolayer MoS_2 nanosheets on SiO_2/Si substrate, the scale bar is 30µm. (e) AFM image of a typical monolayer MoS_2. (f) The cross sectional height profile, corresponding to the white line shown in image (e). The thickness of the MoS_2 triangle is ~0.8nm.*

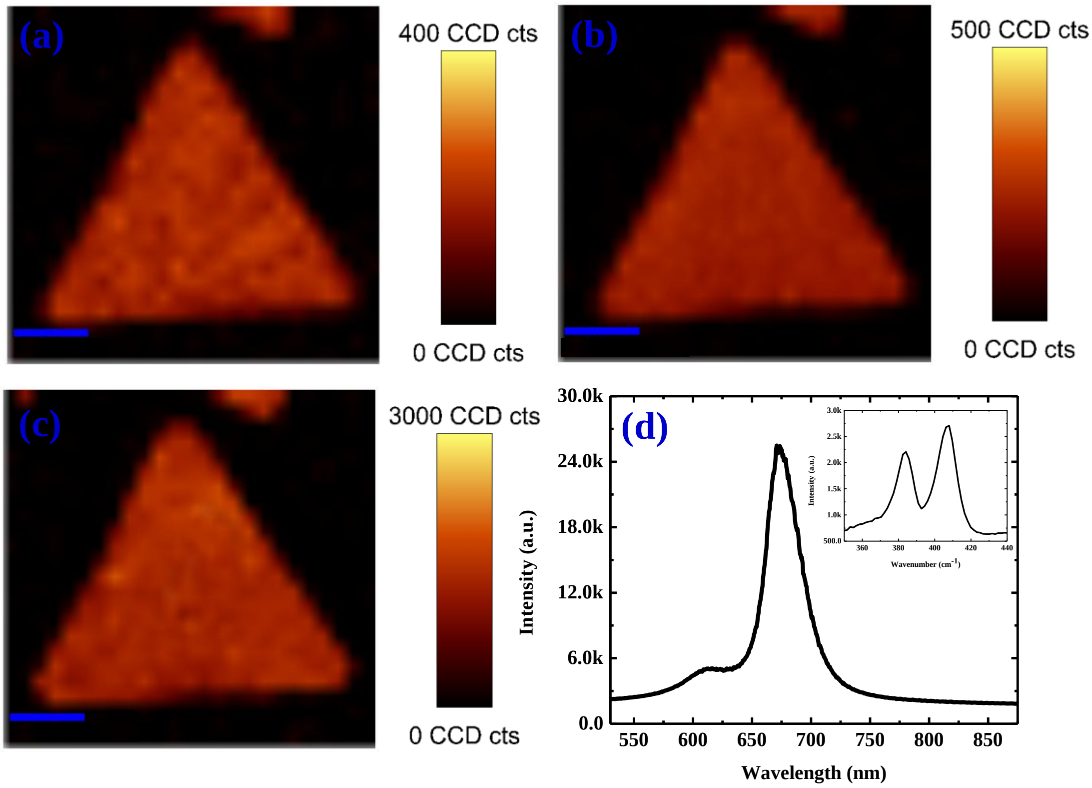

Figure 2.5 *(a-b) The Raman mapping of a typical* MoS$_2$ *triangle integrated with* E_{2g}^1, and A_{1g} *Raman modes, respectively. (c) The corresponding PL mapping conducted with A exciton emission peak. (d) Raman and PL spectra of single layer* MoS$_2$*. The scale bars shown in figures are ~5 µm. The scanning steps for Raman and PL mapping are ~1 µm.*

The origin of these two peaks has been known as optical transitions at K point because of the SOS at the top of valence band. Obviously, the intensity ratio of A to B peaks is higher than that of ME single layer MoS$_2$ sample. The reason for this optical phenomenon will be discussed in Chapter 5.

The samples were prepared with the following steps for TEM characterization: firstly, the samples were spin coated with PMMA A4, at 1500 rpm, resulting in polymer film on the surface of prepared samples. Secondly, the samples were immersed in 30%

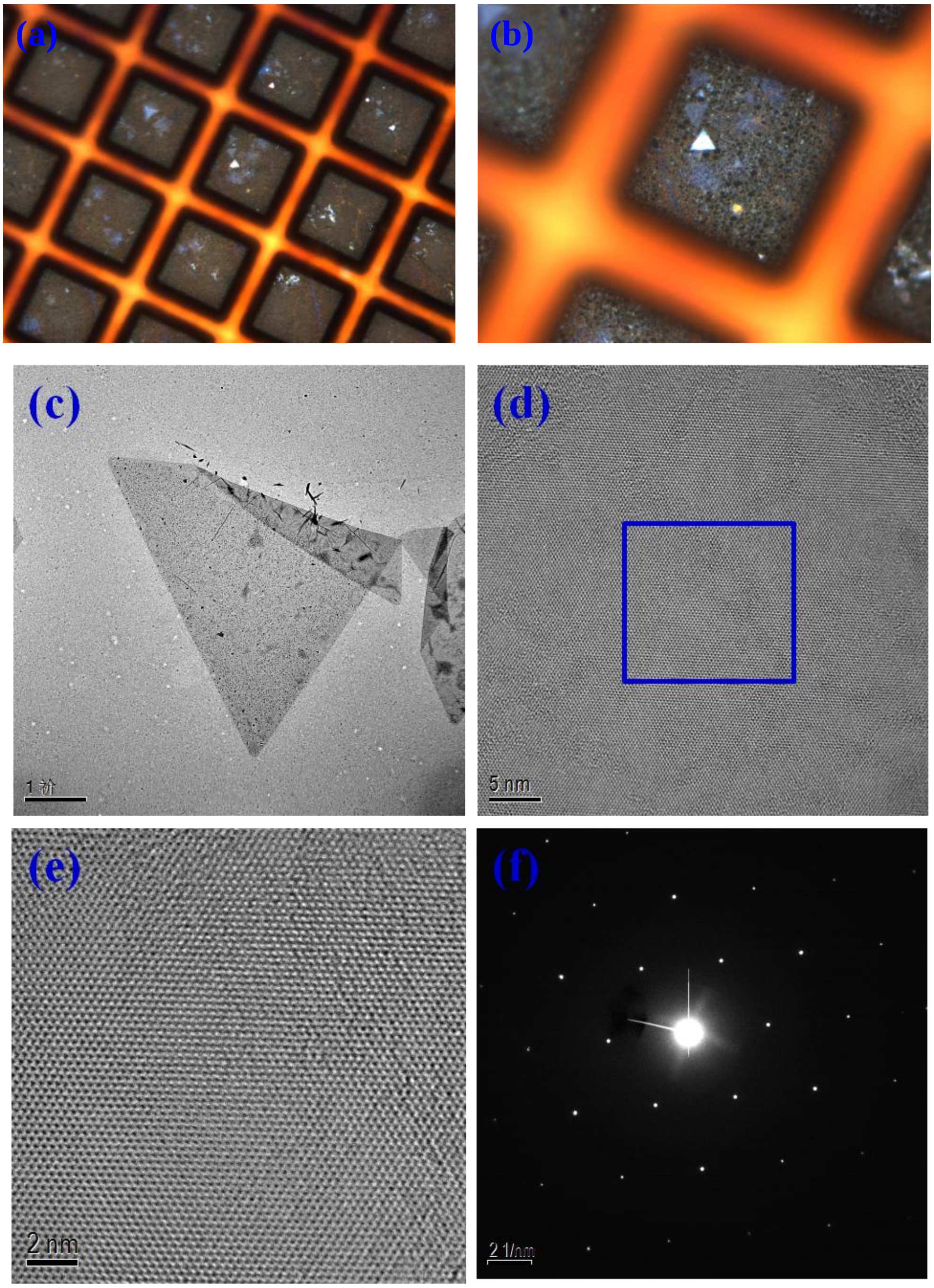

Figure 2.6 *(a-b) Optical images of a TEM grid with many monolayer* MoS_2 *triangle adhered on it; (c) TEM image of a typically monolayer* MoS_2*. (d) TEM image of single layer* MoS_2 *in figure (c). (e) The enlarged high-resolution TEM image of the marked area in figure (d). (f) The selection area electron diffraction pattern taken from the same sample.*

KOH solution. The SiO_2 would be etched and then the PMMA film with MoS_2 sample adhered on it together floated in KOH solution. The floated PMMA film with sample was transferred to deionized (DI) water for several times and then scooped by a prepared TEM gird and dried. PMMA was washed off with acetone and isopropanol. Figure 2.6 (a-b) shows the optical images of TEM grid with transferred MoS_2 samples on it. It is obviously that there are many MoS_2 samples with triangular shape on the holey carbon film. Figure 2.6 (c) shows the transmission electron microscopy (TEM) image for the monolayer MoS_2. Figure 2.6 (d) and (e) show the high resolution TEM images and the enlarged HR-TEM image of the marked area shown in figure (d) is shown in figure (e). Figure (f) is the selected-area electron diffraction (SAED) pattern corresponding to the selected area. The SAED pattern revealed the hexagonal lattice structure of MoS_2 grown.

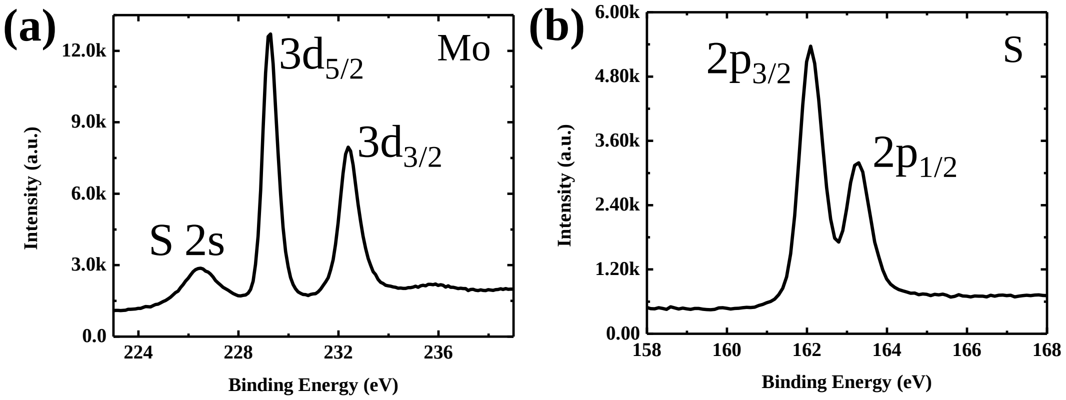

Figure 2.7 *The XPS spectra of monolayer* MoS_2 *for (a) Mo 3d, where the two peaks at 229.25 and 232.32 eV, are assigned as the doublet Mo* $3d_{5/2}$ *and Mo* $3d_{3/2}$*. (b) S 2p, where the binding energy at 162.12 and 163.27 eV are assigned as S* $2p_{3/2}$ *and S* $2p_{1/2}$*, respectively. The XPS data was measured by Kratos Axis Ultra DLD X-ray photoelectron spectroscopy (XPS) spectrometer with monochromatic Al Kα(1486.69 eV).*

The X-ray photoelectron spectroscopy (XPS) for monolayer MoS_2 samples confirms the chemical bonding states of samples grown. As shown in Figure 2.7, the Mo *3d*, S *2s*, and S *2p* peaks of the XPS spectra are presented. The Mo *3d* spectra is composed by two peaks around 229.25 and 232.32 eV which correspond to Mo^{4+} $3d_{5/2}$ and Mo^{4+} $3d_{3/2}$ components of 2H-MoS_2, respectively. The S *2p* spectra consist of peaks around 162.12 and 163.27 eV. The binding energies are all consistent with the reported values for MoS_2 crystal [129].

Single layer MoS_2 FETs in our work were fabricated to evaluate the electrical performance, as presented by Figure 2.8. Figure 2.8 (a-b) shows the schematic diagram of our devices and the optical image of MoS_2 FETs in experiment.

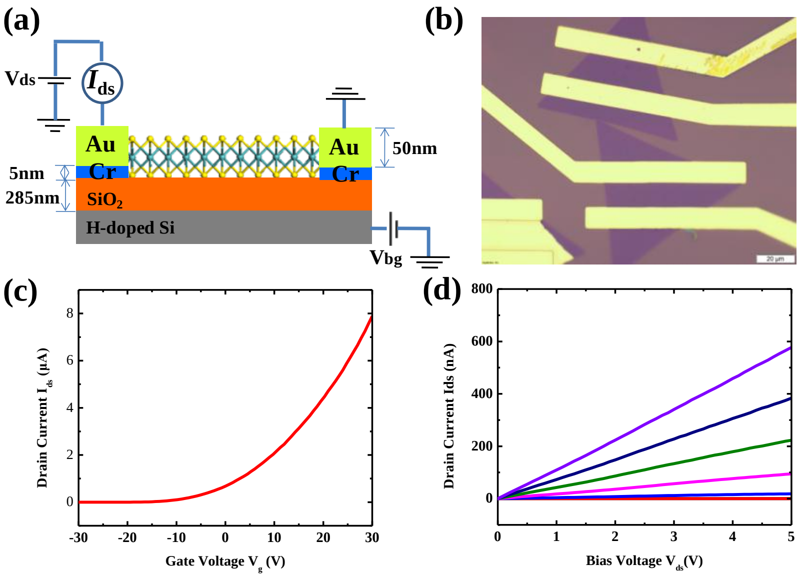

Figure 2.8 *(a) Three-dimensionally schematic diagram for the structure of fabricated transistor in our work. (b) Optical image of three transistors based on the single layer* MoS_2 *grown on* SiO_2*/Si substrate. (c)* I_{ds}*-*V_g *curve for a back-gated single layer* MoS_2 *transistors (*V_{ds}*= 1V) shown in figure (b). (d)* I_{ds}*-*V_{ds} *characteristics of the same device for* V_g*=-30V to 30V with step of 10V.*

From Figure 2.8(b), the channel width (W) and length (L) of our device are about 42.7 μm (mean value) and 14.5 μm, respectively. Figure 2.8 (c) and (d) show the electrical performance of a typical single layer MoS_2 FET (I_{ds}-V_g *and* I_{ds}-V_{ds}). The device displays the n-type FET behavior in ambient with a current on/off ratio of 10^6. According to the equations (2.1) and (2.2), the mobility (μ) and the on-state conductivity (σ_{on}) are ~11.2 cm^2/Vs (V_{ds}=1V) and 119.6 nA (V_g=30V), respectively, given $C_g=1.23\text{x}10^{-4}$ Fm^{-2} for an approximate calculation, which are consistent with previous reports [130, 131].

$$\mu = \frac{dI_{ds}}{dV_{bg}} \frac{L}{WC_g V_{ds}} \tag{2.1}$$

$$\sigma_{on} = \frac{I_{ds}}{V_{ds}} \frac{L}{W} \tag{2.2}$$

2.2 Confocal Raman microscope

Two confocal Raman systems are used in our experiments: WITEC CRM200, and Renishaw inVia Raman systems. Figure 2.9 displays the schematic diagram of the WITEC CRM200 system. The white light illumination system is described as follows in this figure: a tungsten halogen lamp is used as white light source to illuminate on the sample. The white light optical path is shown with yellow background. The laser irradiation system is described as: a 532(457, 633) nm laser is coupled into a single mode fiber and then is reflected by a holographic beam splitter (90:10), and then reflected to the sample after the focus of an objective lens. The sample is put on the stage which could be moved along *X*, *Y and Z* axes manually. This stage could also be moved precisely with a piezoelectronic-control along three axes. The maximum moving distance of this piezo stage is 200 μm along *x* and *y* directions and 20 μm along the *z*-direction. The Raman scattering light as well as the Rayleigh light are collected with backscattering mode. An edge filter is used to block the Rayleigh light. Then the Raman signals and a small fraction of Rayleigh signals go to the grating (1800/ 600/150 grooves/mm) and detected by a TE-cooled charge coupled device (CCD).

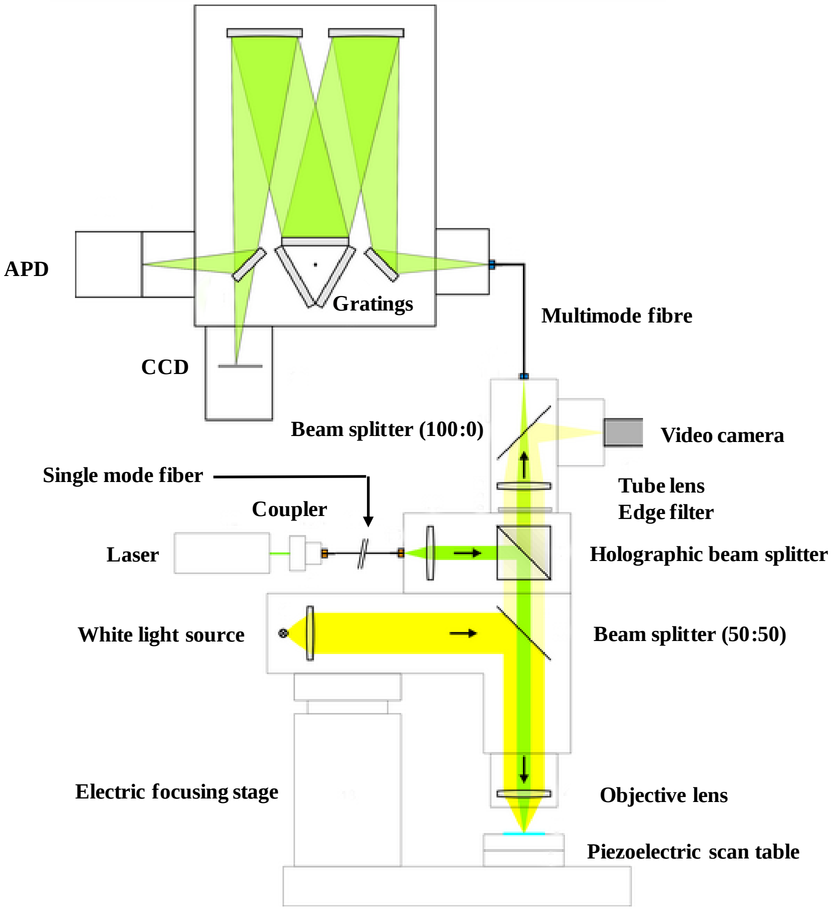

Figure 2.9 *Schematic diagram of confocal Raman system (WITEC CRM200). The optical path of white light illumination is displayed in yellow color and the optical path of laser illumination is displayed in green color.*

Another Raman facility used in our experiments is the Renishaw inVia Raman system, as shown in Figure 2.10, the backbone structure is the same as the described system above (WITEC CRM200) but with a little difference on the design. After entering the system, laser light passes through the spatial filter (a pinhole), which restricts the amount of unwanted scattered light collected from outside the focus of the laser beam, so that a good confocal arrangement is ensured. Then the light is directed to the microscope and focused on the sample by an objective lens. The scattered light from the sample is then collected by the objective lens and directed to the spectrometer after passing through the slit and dispersed by diffraction grating (2400 or 1200 grooves/mm).

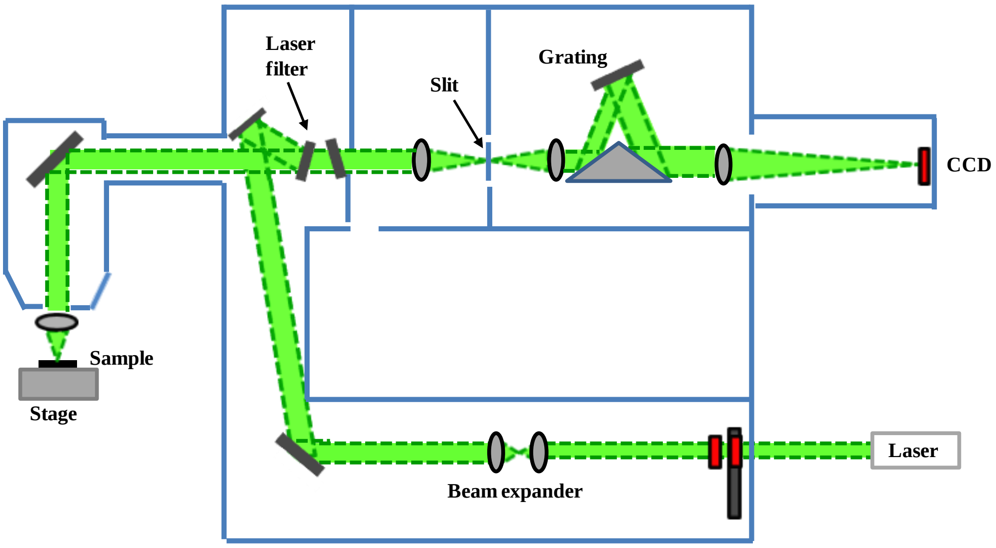

Figure 2.10 *Schematic diagram of confocal Renishaw inVia Raman system. A monochromatic light beam is focused on the measured sample and the scattering signals are directed through the optics of spectrometer and then collected by CCD detector.*

2.4 Conclusions

In this Chapter, we introduced the fabrication methods of MoS_2 layers used in our work and compared the three different fabrication methods (ME methods, CE methods and CVD methods). Our preliminary results on CVD grown samples were also presented in this section. Moreover, the common characteristic techniques, such as Raman, PL characterization, were introduced and their working mechanisms were discussed, respectively.

Chapter 3

Spin orbital splitting in MoS_2 revealed by second order resonant Raman spectroscopy

3.1 Introduction and motivation

3.1.1 The importance of spin orbital splitting

Before 1980, all states of matter in condensed matter systems could be classified by the symmetry of matter. After the discovery of quantum Hall (QH) state in 1980 [132], it was found firstly that a quantum state could have no spontaneously broken symmetry. In recent years, a new kind of topological state called quantum spin Hall (QSH) hall [133-136] effect was predicted theoretically [137, 138], which attracted the great interest of researchers in the field of spintronics. Since the spin degrees of freedom could be manipulated by electric methods without a magnetic field by this effect, not similar to the traditional logic devices which is purely based on charge current, QSH based spintronics devices could process and store information by the quantum channel. Therefore, it could operate with a low power consumption, fast computation speed and reversible quantum computations [139, 140]. The intrinsic QSH effect has hinted us to search for a matter with non-trivial states. Although the QSH edge states have been demonstrated experimentally in HgTe/CdTe [134, 137] and InAs/GaSb [141, 142] quantum wells, the practical application of such a QSH-based device is hampered by the following factors: (i) band gap is too small, which limits the operation of device at high temperatures. Thus the searching for large-gap QSH insulators is motivated; (ii) the small number of conducting channels leads to a small signal-to-noise ratio; and (iii) the lacking of available methods to realize the high on/off ratio [137, 143-149].

Recently, 2D materials have been demonstrated their potential on developing electronic devices [150]. Graphene was proposed that could supply an interesting theoretical mode due to the existence of QSH [151], which was expected to the realization of low-dissipation quantum electronic devices. However, this idea was unrealistic due to the small spin orbital splitting (SOS) in graphene [152, 153]. Luckily, a new class of 2D transition metal dichalcogenides (TMDCs) was proposed to have a larger spin orbital splitting (SOS) (~0.1 eV) [154]. MoS_2, as a typical TMD material, has been widely studied. As to the spin orbital coupling (SOC), Kramer's degeneracy $[E\uparrow(\boldsymbol{k}) = E\downarrow(\boldsymbol{k})]$ is established in the MoS_2 bulk by the combination of time-reversal $[E\uparrow(\boldsymbol{k}) = E\downarrow(-\boldsymbol{k})]$ and inversion symmetry $[E\uparrow(\boldsymbol{k}) = E\uparrow(-\boldsymbol{k})]$ [155, 156]. However, for monolayer MoS_2 system, it is expected to cause the energy bands to develop a larger SOS due to the broken of spin degeneracy of the valence band and conduction band along the direction of $\Gamma - K$.

3.1.2 The motivation of this work

As a typical material in TMD group, MoS_2 has attracted tremendous attentions in recent years [16, 18, 19, 157]. The band gap of MoS_2 layers varies from indirect for few-layer and bulk to direct for monolayer phase [18, 19]. Such a band gap evolution leads to the interesting electronic and optical properties in MoS_2. Another significantly physical feature in monolayer MoS_2 is its sizable SOS due to the absence of inversion symmetry. The spin degeneracy at the top of valence band along the direction *Γ*-*K* is broken because of the strong SOC [10]. The giant SOS makes monolayer MoS_2 desirable for many physical phenomena such as the spin-Hall effect [158], quantum spin-transfer [159], spin domain reversal [9], and magnetic phase transition [160]. Considering the important role of SOS in the application of MoS_2 on spintronics-based devices, it is challenge to develop an effective experimental method to detect and explore intrinsic SOS in MoS_2.

Previous attempts of exploring SOS mainly focus on the energy difference between A and B peaks appeared in the PL spectrum of MoS_2 [17, 59] and attributed this energy difference to the value of SOS. However, the origins of these two PL peaks (A and B) are still confused, especially for the involvement of an additional bound exciton peak, which is sensitive to the environment [44, 161]. Occasionally, only one emission peak appears in the PL spectrum of single-layer MoS_2 at the room temperature because of the quenching effect of bound excitons [17, 162]. Also the energy difference between A and B emission peaks is not dependent on the number of layers in the PL spectrum of MoS_2 layers, which is in conflict with the calculation results. Furthermore, the reported values of SOS do not match well with the energy difference between A and B PL peaks. Hence the discussion on its origin causes extensive debate as it may arise from either SOS at the top of valence band or defect induced luminescence [17, 44, 59]. Thus it is desirable to find a reliable way to probe the fine electronic band structure, EPC and SOS in MoS_2. The resonant Raman spectrum is very sensitive to the energy matching between the electronic bands and the energy of the phonons involved. In order to explore the SOC in MoS_2, the resonance Raman scattering, excited by a specific wavelength, would be an efficient and accurate method.

In this letter, Raman spectra in MoS_2 were systematically investigated by different excitation laser lines, including single-layer, bilayer, quad-layer, and bulk MoS_2. When the samples were excited by 325 nm laser line, the intensities of high-order modes ($2\mathrm{E}_{2g}^{1}$ and $2\mathrm{A}_{1g}$), as well as their combination modes (E_{2g}^{1}+A_{1g}) are obviously enhanced in few-layer MoS_2 layers compared with the intensities of them when excited by other laser lines. In this work, the observed Raman resonance was ascribed to the electron-two-phonon coupling based triply resonant Raman scattering (TRRS) process. The value of SOS provided a platform for the resonant Raman spectra of overtone and combination modes. However, we did not observe such a resonant behavior in bulk MoS_2. According to the calculation results on the value of SOS, bulk MoS_2 displays a larger value of SOS which cannot match the energy of the involved resonant phonons. The laser excitation energy dependent resonant Raman enhancement for overtone and combination phonon modes results in a new technique for the probing of SOS in single-layer MoS_2.

3.2 Experimental methods

The MoS_2 samples in this work were fabricated by mechanically exfoliated methods from MoS_2 crystal (SPI Supplies) by Scotch tape and then transferred them on Si/SiO_2 substrate. The Raman spectra excited by 488 nm laser was measured by a WITEC alpha 300R Confocal Raman system with 1800 mm^{-1} grating and the measurement excited by 457 nm laser and 633 nm were conducted in a WITEC alpha 200R with the same measurement parameters. Renishaw Invia Raman microscope integrated with 325 nm and 532 nm laser was also used to measure the Raman spectra of MoS_2 layers in this work. The values of power used here were kept below 0.5 mW to avoid heating effect for all involved laser lines.

The band structures of MoS_2 layers with different thicknesses are performed by first-principles calculations using Vienna ab initio Simulation Package (VASP), using the local-density approximation (LDA) [163, 164]. The calculation in this chapter is done by my collaborator Dr Yan Jiaxu. The cut-off energy for the basis set was 400 eV. The Brillouin-zone integration was performed scheme using a $36 \times 36 \times 1$ mesh within Monkhorst-Pack and the Methfessel-Paxton smearing with a width of 0.1eV. The energy relaxation for each strain step is continued until the forces on all the atoms are converged to less than 10^{-2} eV $Å^{-1}$.

3.3 Results and discussion

As discussed above, it has been widely reported that the electronic structures and vibrational properties of MoS_2 layers are different when their numbers of layers vary [42, 48]. Thus for comparison, we intentionally select MoS_2 samples with different number of layers in our experiment. Some techniques have been adopted to identify the thicknesses of MoS_2 nanosheets, such as AFM, PL, and Raman spectroscopy. Figure 3.1(a) gives the optical graph of a typical MoS_2 sample. It can be seen that the MoS_2 sheets with different thicknesses (areas A, B, C and D) present different optical contrast due to the multiple reflection effect [165, 166]. The Raman spectra for these areas are shown in Figure 3.1(b). As peak intensities and frequencies for E^1_{2g} and A_{1g} modes present obvious dependence on the thickness of MoS_2 nanosheets, thus the thickness of areas A, B and C should be 1, 2 and 4 layers, respectively, and the area D is bulk MoS_2 [18, 80]. The thickness of this sample was confirmed by AFM. Figure 3.1(c) shows the AFM image of MoS_2 sample shown in Figure 3.1(a). The corresponding height profile along the green line in Figure 3.1(c) is shown in Figure 3.1(d). Thus the thickness of areas A, B and C are indeed 1, 2, and 4 layers. It is worth noting that the thickness of single layer is about 0.65-0.8 nm on Si/SiO_2 substrate which highly depends on substrate varying from sample to sample because of the substrate effect [166, 167]. The thickness of the additional m layers is $\sim 0.65\times m$ nm, which is consistent with the calculated result of the adjacent layer-layer distance [168].

The Raman spectra of the MoS_2 layers with different thicknesses excited by various excitation lasers are shown in Figure 3.2. It is noted that, in the range of 750 to 840 cm^{-1}, three obvious Raman peaks appears when the sample excited by the 325 nm laser line. When the samples excited by other laser lines: 457, 488, and 532 nm lasers, we don't observe the high-order Raman modes in the targeted measurement range, which is unlike to the experimental results excited by 325 nm laser line.

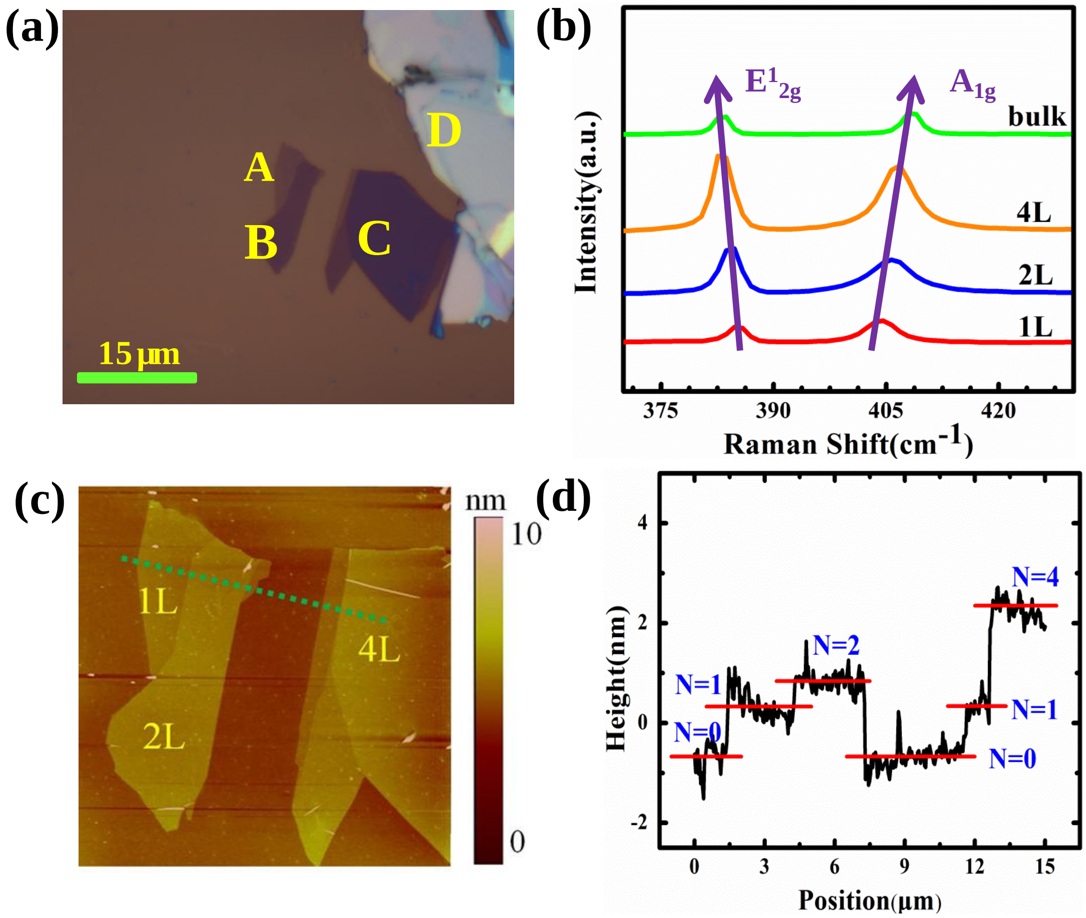

Figure 3.1 *(a) Optical graph of MoS$_2$ nanosheets, with 1L, 2L, 4L and bulk. (b) Raman spectrums of E$^1_{2g}$ and A$_{1g}$ modes for MoS$_2$ nanosheets with different thickness. (c) AFM image of MoS$_2$ nanosheets shown in Figure (a). (d) The corresponding height profile with the green lines shown in Figure (c).*

According to the previous studies on the assignment of these three Raman peaks, they are assigned as the second-order and combination modes of E$^1_{2g}$ and A$_{1g}$ modes [83, 169]. The overtone modes are usually very important to understand the mechanism of electron phonon coupling, as well as its electronic band structure. For the resonant Raman spectra obtained in this work, we attribute the enhanced scattering intensity of high-order modes to the electron-two-phonon involved EPC process [170-172]. Four steps are involved for such a resonant Raman behavior, as shown in Figure 3.3(b): (1)

electron is excited from the v_2 band to the conduction band c_i (schematically represented by c_i); (2) the hole left in the v_2 band is scattered by a phonon with momentum ***q*** to the v_1 band via an interband transition, and then the hole is scattered by another phonon with momentum ***-q*** to the top of the v_1 band via an intraband transition process (3); (4) the excited electron decays to the top of v_1 band and recombines with the scattered hole in (2) and (3). Thus, this process is also called TRRS process.

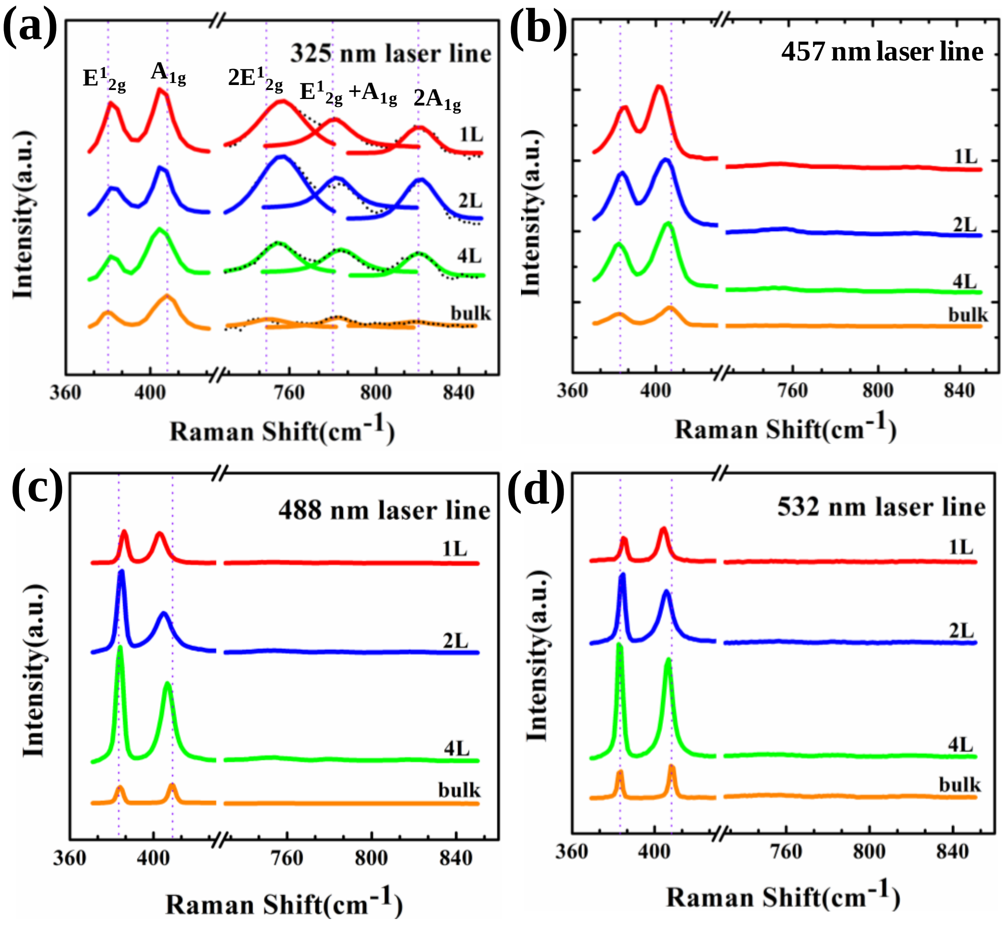

Figure 3.2 *The Raman spectra of different thickness MoS_2 layers of its first order modes (E^1_{2g} and A_{1g} modes) and their corresponding second order ($2E^1_{2g}$ and $2A_{1g}$) and combination modes ($E^1_{2g}+A_{1g}$) when using 325, 457, 488 and 532 nm laser lines, respectively.*

As described above, the crucial factor to fulfill the TRRS process is that the energy splitting $\Delta E_{SO} = E(\upsilon_1) - E(\upsilon_2)$ should match well the sum of two involved first-order phonon energies (E^1_{2g} and A_{1g} modes). Particularly, in single-layer MoS_2, ΔE_{SO} comes exclusively from SOS without interlayer coupling. The key factor to fulfill the conditions of SOS is a result of the lack of inversion symmetry in single-layer MoS_2 [Figure. 3.3(a)], while for its bilayer case, inversion asymmetry is introduced, the splitting energy at the top of valence band led by SOC is very small, and such a splitting energy shown at the top of valence band is the combination effects of SOC and interlayer coupling [43].

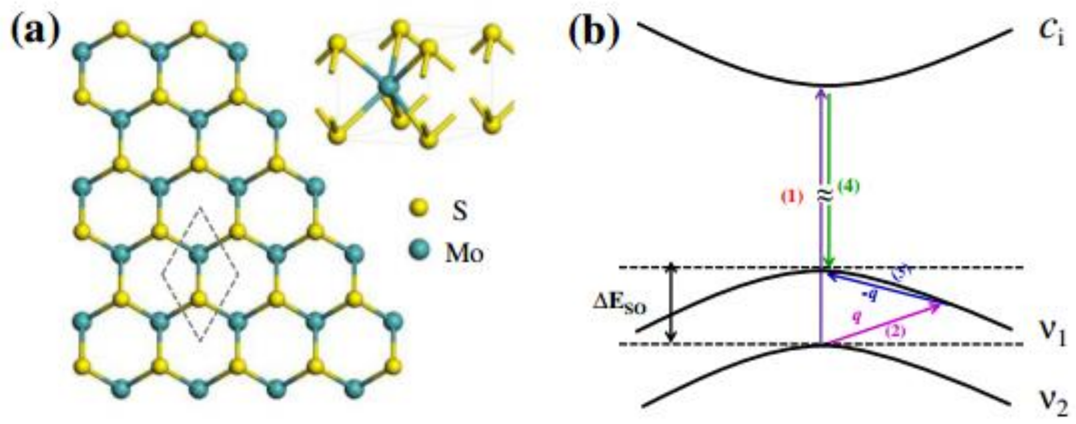

Figure 3.3 *(a) Atomic structure of monolayer MoS_2 (top view). The black lines represent the unit cell of monolayer MoS_2 in the ab plane. The inset in the upper right figure, the unit cell of monolayer MoS_2 is shown with the broken of inversion symmetry. (b) Proposed schematic diagram for the TRRS process in MoS_2; v_1, v_2 indicate the splitting at the top of valence band led by SOC, and ci represents a possible final states for the optical transition in conduction band.*

Therefore, it seems that the energies of involved resonant phonons in single layer MoS_2 could be used to identify the energy of SOS. To clarify the mechanism of the resonant Raman spectra observed in this work, one issue is needed to be considered: which electronic transition is allowed between the valence and conduction band when 325 nm laser is used as excitation source?

The electronic band structures of MoS_2 layers with different thicknesses (monolayer, bilayer, bulk MoS_2 as representative in this work) have been calculated by considering SOC effect using the Vienna ab initio simulation package (VASP), within the local-density approximation [163, 164]. From Figure 3.4, it is obviously that the valence band maximum in each electronic band splits into two bands marked as v_1 and v_2 bands. Furthermore, in the conduction band, another two bands appears due to the SOC induced splitting, named as c_5 and c_6 bands. The energy between $v_1(v_2)$ bands and $c_5(c_6)$ bands is around 3.8 eV, which is corresponding to the energy of excitation wavelength.

Now the problem is to determine exactly which transition ($v_{1(2)}$ to $c_{5(6)}$ bands) is allowed. In order to solve this problem, the spin indexes of these four involved electronic bands are considered. As shown in Figure 3.4 (a), the red and blue lines represent the spin-up and spin-down states, respectively, where both transitions from v_2 to c_6 bands and from v_1 to c_5 are allowed since only transitions between electric bands with the same spin indexes are allowed. According to our calculation results, the energy difference between v_2 and c_6 electronic band (3.87 eV) can match with the incident photon energy (~3.81 eV) when samples excited by 325 nm laser. However, the energy of incident photon does not match well with the v_1 to c_5 transition (3.62 eV).

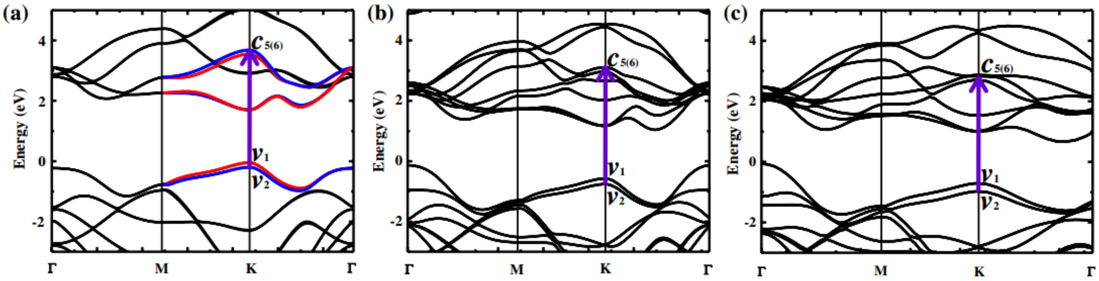

Figure 3.4 *The electronic band structures of* MoS_2 *layers with considering the SOC effect: (a) single layer, (b) bilayer, and (c) bulk* MoS_2*. The color lines represent the spin indexes of the involved electric states. The red (*v_1 *and* c_5 *) and blue lines (*v_2 *and* c_6 *) represent the spin-up and spin-down states, respectively. The purple arrow shown in each graph represents electronic transition from* v_2 *to* c_6 *bands resulting from the excitation of 325 nm laser, which is corresponding to the process (1) described in Figure 3.3(b). In this figure, we only show the helicity (*σ_+*) case as an example.*

The partial charge densities (PCD) of the involved bands are calculated to further confirm whether this transition from v_2 band to c_6 band conforms to the selection rules. As shown in Figure 3.5, at the top of valence band, v_1 and v_2 bands shown in single-layer MoS_2 case are mainly composed by *d* orbitals of Mo atoms, which is consistent with previous reports [44, 154, 173]. In conduction bands, c_5 band mainly originates from the *d* orbitals of Mo atoms and c_6 band is composed by the combination of *d* orbitals of Mo atoms and the *p* orbitals of S atoms. Since the rule of electronic transition requires that the difference of the azimuthal quantum number should be 1, the only possible optical transition is the Mo (*d*) orbitals in the v_2 band to the S (*p*) orbital in the c_6 band. This transition with spin indexes is reported firstly and observed in our work, which could be further studied by optical helicity, together with the spin valley coupling, although the previous work reported this optical transition from v_1 and v_2 to c_6 band may be attributed to the α and β excitons emissions [174], which is not the discussion scope of this work.

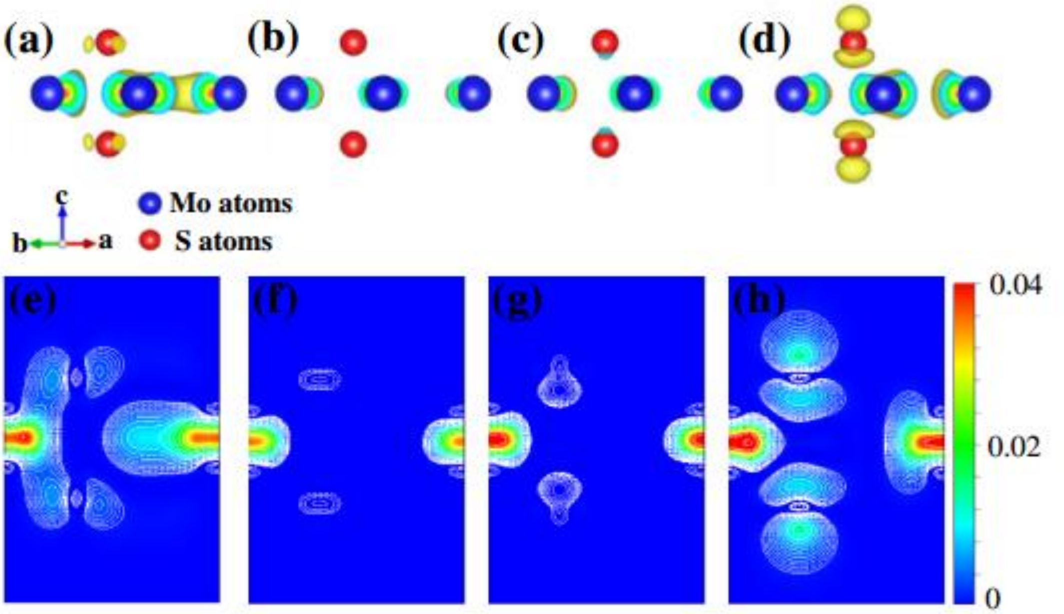

Figure 3.5 *(a)–(d) three dimensional PCD graphs for electronic bands (a) v_2, (b) v_1, (c) c_5, and (d) c_6 in single-layer MoS_2, respectively. (e)–(h) two dimensional PCD graphs corresponding to (a)–(d), respectively.*

Till now, the whole physical process for the TRRS becomes clear: (1) an electron is excited by absorbing a photon from the v_2 band to the c_6 band at the K point in the Brillouin zone; (2) the hole left in the v_2 band after the electron excited is scattered by a phonon with momentum *q* to the v_1 band by inter-band transition [175]; (3) the hole is scattered by another phonon with momentum -*q* scatters to the top of the v_1 band by intra-band transition to form an exciton together with the electron in the c_6 band [176];

(4) meanwhile, the excited electron decays into the top of valence band and the electron-hole pair recombines at the top of the v_1 band with a photon emitting. In this TRRS process, the Fröhlich interaction induced electron scattering by E_{2g}^{1} phonon must be involved to fulfill the condition of Raman enhancement of the second order modes ($2E_{2g}^{1}$). Otherwise, the Raman intensity of the $2E_{2g}^{1}$ mode cannot be enhanced [171, 172]. The whole TRRS process involved electron-two-phonon coupling results from the deformation potential induced inter-band transition and Fröhlich interaction induced intraband transition. Considering the energy and momentum conservation in TRRS process, the energy transitions for these three different Raman modes can be written as equations (3.1) to (3.3), respectively:

$$E_{\text{laser}} = E_{\text{exciton}} + 2E_{E^{1}2g} \qquad (3.1)$$

$$E_{\text{laser}} = E_{\text{exciton}} + 2E_{A1g} \qquad (3.2)$$

$$E_{\text{laser}} = E_{\text{exciton}} + E_{E^{1}2g} + E_{A1g} \qquad (3.3)$$

In order to satisfy momentum conservation, the overall momentum of the two involved phonons must be zero in each case discussed above. Since both E_{2g}^{1} and A_{1g} modes are almost dispersionless in momentum space along the Γ-M direction in momentum space [48, 85, 177], which is very convenient for the observation of TRRS process in our work. Besides the momentum space, the energy conservation should also be considered. As shown in Figure 3.3 (b), the phonon involved in the process (2) in the TRRS process must have the suitable energy (ΔE_{SO} /2) and momentum **q** simultaneously to scatter the hole from the v_2 band to the v_1 band. The dispersionless phonon curve in MoS_2 means that many phonons may exist with similar energy and momentum but opposite direction. A phonon with the right momentum could always be found to ensure momentum conservation as long as the phonon energy could matches well with a suitable energy.

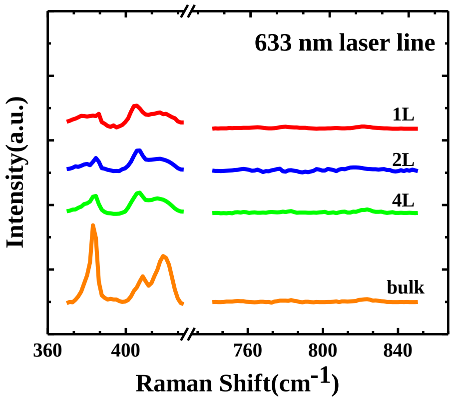

Figure 3.6 *The Raman spectra of MoS$_2$ samples with different layer numbers excited by 633 nm laser lines, respectively. All the Raman spectra have been normalized by the intensity of A$_{1g}$ peak of bulk samples.*

Actually, the energy gap between v_2 band and c_1 band (1.89 eV) is very close to the energy of 633nm laser (1.96 eV). In Figure 3.6, it shows the Raman spectra of different layered MoS$_2$ excited by 633nm laser. However, we cannot observe the obvious resonance for overtone and combination modes. To explain this question, we have to take account of the selection rule of electronic transition. As the conduction-band minimum states are made of the dz^2 orbital of the Mo atoms, and the separated bands is degenerate at K point due to the inactive SOC, the transitions are allowable ($v_1 \rightarrow c_{1(2)}$, $v_2 \rightarrow c_{1(2)}$) from the viewpoint of spin indexes. However, when we take account of the partial charge density, as discussed above, conduction-band minimum is dominated by Mo dz^2 orbitals, and density of states of v_1 and v_2 bands are mainly composed by the *d* orbitals of Mo atoms with very little mixing of the *p* orbitals from S atoms, as shown in Figure 3.7. Therefore, the photon induced resonant electronic transition ($v_1 \rightarrow c_{1(2)}$, $v_2 \rightarrow c_{1(2)}$) is not high when considering the selection rule ($d \rightarrow d$ transition is not allowed), which gives rise to the ignorable TRRS for second order and combination modes at the wave number range (760-820 cm^{-1}). Therefore, the c_i band shown in Figure 3.3 (b) in the manuscript is not an arbitrary band in this triply resonant Raman process, but it is the one that need to fulfill many aforementioned transition conditions.

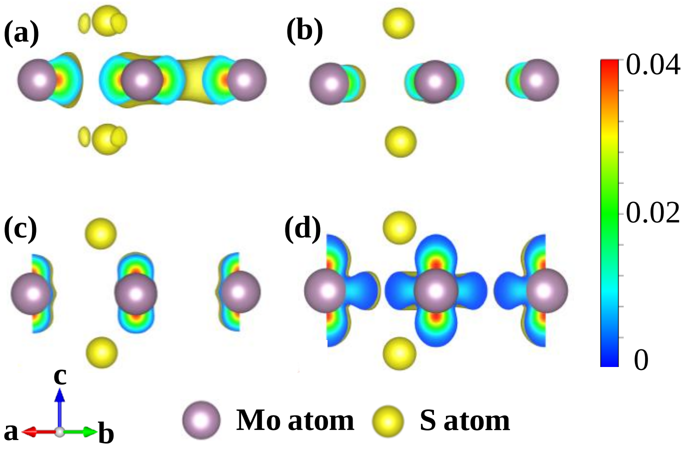

Figure 3.7 *3D partial charge densities for (a)* v_2*, (b)* v_1*, (c)* c_1 *and (d)* c_2 *bands. The charge density contours start from 0.001e/a.u.3 and increase successively by a factor of* $10^{1/10}$*.*

The observation of abnormally enhanced intensities of overtone and combination modes in the TRRS process makes a significant step towards the aim of exploring the SOS in single-layer MoS_2. Perdew-Burke-Ernzerhof, Heyd-Scuseria-Ernzerhof, and GW approximation have been performed in previous calculation results to investigate the value of SOS but the calculation results are various, between 146 and 193 meV [105]. In our calculation work, the value of SOS is ~152 meV, which is within the reported range in the literature. Experimentally, due to TRRS when 325 nm laser was used as excitation source, three high-order Raman modes were obviously observed with phonon energies within the range of 93 meV (2 E_{2g}^1) to 102 meV (2A_{1g}), which could give a value of SOS ~100 meV for monolayer MoS_2. For bilayer and multilayer MoS_2, the origin of band splitting at the top of valence band is from the combination effect of SOC and interlayer coupling [105, 178]). Furthermore, the spin is degenerate at the top of valence bands due to the inversion and time reversal symmetry, which means each of the separated band (v_1 or v_2) at k and k'valley contains both spin-up and spin-down indexes where different spin-polarized indexes come from different individual layers. Therefore, the interlayer coupling within the same spin states needs to commute with SOS [179]. The bulk MoS_2 possesses much larger separated energy at the top of valence band [Figure 3.4(c)], which means energy match is lost between splitting of energy at the top of valence band and energy of the two phonons involved, thus the probability of TRRS in bulk MoS_2 is reduced and intensities of overtone and combination modes in bulk MoS_2 is very weak.

Table 3.1. The values of ΔE_{SO} calculated by various methods.

Calculation Method	PBE (1)	HSE (2)	G_0W_0(3)	Our result (LDA)
ΔE_{SO} (meV)	146	193	164	152

3.4 Conclusion

The dramatically enhanced intensities of the overtone and combination Raman modes of E^1_{2g} and A_{1g} modes in few-layer MoS_2 were experimentally observed when the samples excited by 325 nm laser. According to the theoretical results calculated by the first-principle calculations with considering SOC effect, we proposed such a resonant Raman enhancement resulted from the Fröhlich-interaction and deformation potential-interaction involved electron-two-phonon TRRS process. The SOS located at valence band maximum (at *K* point) played a crucial role in the Raman resonance. Furthermore, the value of SOS in single-layer MoS_2 was defined experimentally, which matched with our calculation results well. Therefore, the resonant Raman spectra based on the TRRS technique could provide a novel and convenient way to study the SOC effect in MoS_2, which is important to develop the MoS_2-based spintronic devices in future [44, 178].

Chapter 4

Plasma modified MoS_2 nanosheets for surface enhance Raman scattering

4.1 Introduction

Surface Enhanced Raman Spectroscopy (SERS) is a Raman spectrum based technique that could dramatically enhance Raman signal from detected molecules when these molecules adsorbed onto specially-prepared substrate [180-184]. The advantages of SERS are its surface selectivity and highly sensitivity. In a general Raman measurement, after the photons of the excitation laser illuminating on the sample, the Raman signal of bulk materials overwhelms the Raman signal from the molecule at the surface of bulk materials. While due to the high selectivity of SERS, the Raman signals resulting from the detected molecules on the surface of bulk present a dramatically enhancement and could be detected directly by overwhelming the Raman signal from bulk [185].

Till now, it is widely acceptable that two mechanisms are used to explain the SERS phenomenon in the literature [184, 185]: electromagnetic enhancement and chemical enhancement. The former is dominant and the enhancement depends on the presence of features of metal surface, while the enhancement effect of the latter contributes only one (or two orders) of magnitude which is related to the electronic states of adsorbates and substrates [185]. The chemical enhancement could be used in many research fields, such as biological systems, and other absorbate-surface interactions.

It is well known that the Raman scattering intensity is proportional to the square of the magnitude of electromagnetic field (E) incident on the detected molecules [184, 186]:

$$I_R \propto E^2 \tag{4.1}$$

where I_R is the intensity of the Raman scattering, and E is the total electromagnetic fields coupling with the detected molecule; and where

$$E = E_a + E_p \tag{4.2}$$

E_a is the electromagnetic field on the detected molecule with the absence of any roughness features, E_p is the electromagnetic field emitting from the particulate metal surface's feature.

As to the mechanism of chemical enhancement, it is less understood till now than the electromagnetic enhancement. One explanation is that the molecules adsorbed on the surface of the substrate interact with the surface which contributes to the chemical enhancement between them [185]. Another reason is the molecular orbital of the absorbates broaden into the conducting electrons of the substrates, and change the surface chemistry of the substrates [187].

MoS_2, as a new typical 2D layered material, has been widely investigated in many fields [16, 25-35, 188]. Moreover, 2D materials usually have some considerable attention for their atomic-level flat surface [189], high biocompatibility [190, 191], selective enhancement [192], and so on. Based on these special properties, the analogue of MoS_2, graphene, has been widely used as a 2D active substrate for the detection of organic molecule and DNA [189, 190, 192, 193]. Moreover, graphene can be used to separate the electromagnetic (EM) enhancement and chemical charge transfer enhancement (CT) [192], because plasmon frequency of graphene is in terahertz range [194]. As to MoS_2, besides these promising advantages of graphene mentioned above, MoS_2 has a variable band structure with its number of layers increasing [18, 195]. Besides, the structure of single layer MoS_2, different from graphene, is a sandwiched S-Mo-S three-layer structure [16]. Here we will explore whether MoS_2 nanosheets could be used as an ultrathin active platform for SERS.

Some recent experiments have been designed to tune the SERS effect for graphene substrate, such as nitrogen doping improved sensitivity of sensing [196], UV/Ozone oxidized treatment due to the oxygen containing groups [192]. Especially the graphene oxide fluorinated by CF_4 plasma, has confirmed the hypothesis that the disorder or defect induced local dipole on substrate surface could play an important role in enhanced Raman signal of molecular [197]. In this work, we reported that Raman signals of R6G molecules could be enhanced dramatically when measured on the MoS_2 nanosheets pre-treated by oxygen plasma treated (OT) and argon plasma treatment (AT). Compared with the Raman signal on pristine (P) MoS_2 nanosheets, Raman signals of R6G molecular measured from treated MoS_2 substrates are enhanced by 14 times. We attribute the introduction of defects changes the locally electronic and chemically properties and thus improve the charge transfer between defective MoS_2 and R6G molecules, which contribute to the Raman enhancement of R6G molecular.

4. 2 Experimental results

In our work, MoS_2 nanosheets were mechanically exfoliated from a nature MoS_2 crystal (SPI Supplies) by scotch tape. The exfoliated samples were treated firstly by oxygen (argon) plasma with a constant dose of oxygen (argon) at 80 sccm for 5 seconds. To create the proper amount of defects but without seriously damaging the sample, the power is very mild. Then, the plasma treated MoS_2 samples were immersed in 10^{-6} mol/L solution of R6G molecule for 2h. Another MoS_2 sample without plasma treatment is taken for reference. The Raman spectra excited by 532 nm laser line were taken on Renishaw inVia Raman Microscopy configured with a CCD array. The laser power measured in this work was kept below 0.2 μW. All of the Raman spectra were collected by a Leica objective lens (100x with NA=0.85). The grating used for Raman measurement is 2400 line mm^{-1} with a spectral resolution ~0.8 cm^{-1}. The PL spectrum was taken on WITEC CRM200 Raman system with 532 nm laser as excitation light and the grating used is 150 mm^{-1}.

First principle calculations were used to carry out the simulation work implemented in VASP [163]. The Perdew, Burke, and Ernzerfhof (PBE) potentials were used in all of calculations in this chapter. The requirement of convergence is with the cut off energy at 400 eV. The types of defects, the chemisorption sites of O, as well as the frequency at gamma point is simulated using a $5 \times 5 \times 1$ mesh within Gamma centered grids for 3x3x1 supercell. The convergence energy in the self-consistent is 10^{-5} eV. The charge transfer between MoS_2 and R6G are calculated by the sample methods but with a supercell 5x5x1 for MoS_2. The Brillouin-zone integration was performed scheme using a $1 \times 1 \times 1$ mesh within Gamma centered grids. The energy relaxation for each strain step is continued until the forces on all the atoms are converged to less than 10^{-2} eV $Å^{-1}$.

4. 3 Results and discussions

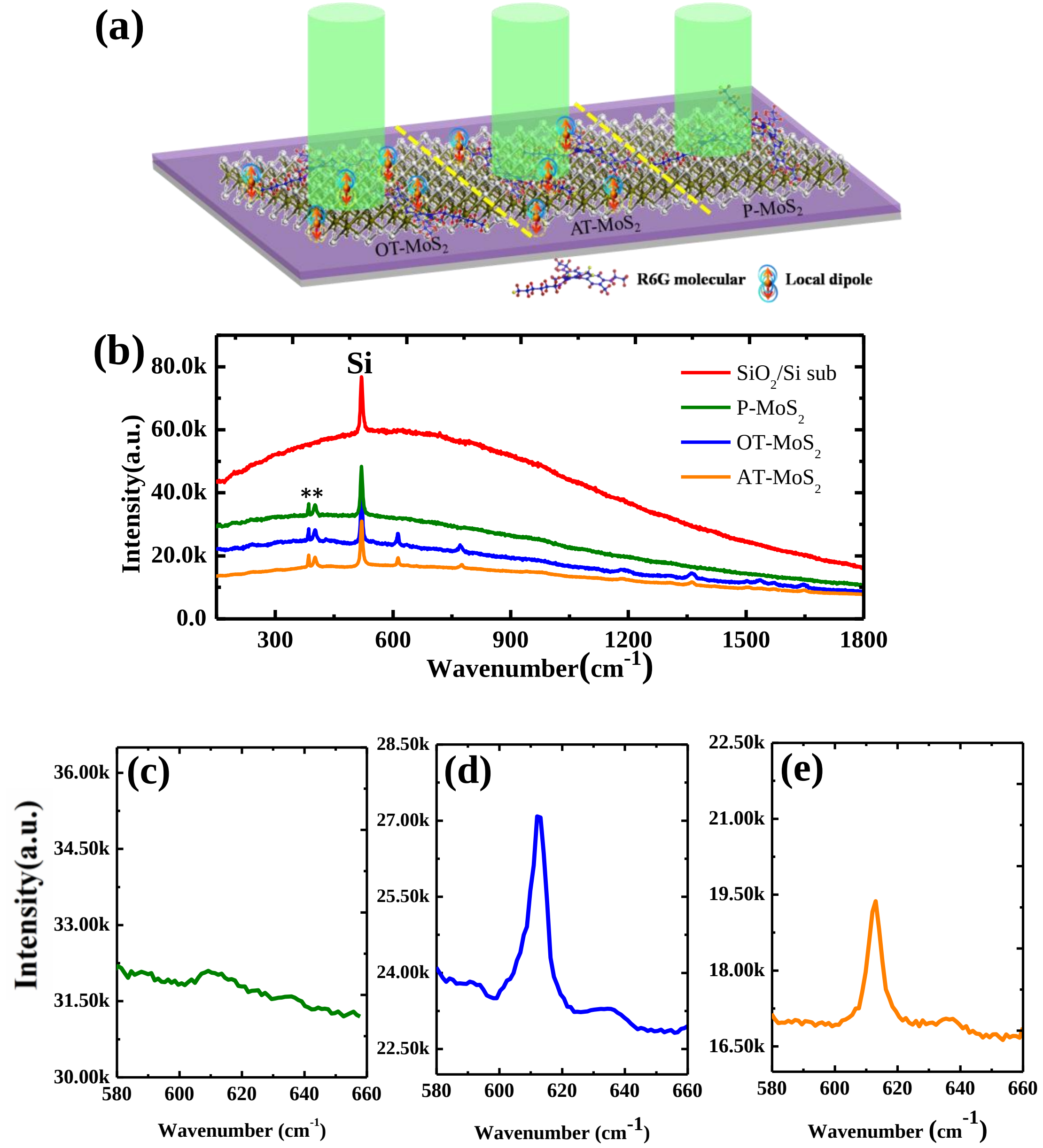

Figure 4.1 *(a) Schematic diagram of the R6G molecules on 1L P-*MoS_2*, OT-*MoS_2*, and AT-*MoS_2*, respectively; (b) Raman signals of R6G molecules measured on the given four substrates. (c-e) Enlarged Raman spectra of R6G molecule in the range of 580 - 660* cm^{-1} *of 1L P-*MoS_2*, and OT(AT)* MoS_2*, respectively. The Raman peaks originate from* MoS_2 *nanosheets denoted by asterisks (*).*

The schematic diagram of R6G molecules deposited on 1L P-MoS_2, OT-MoS_2 and

AT-MoS_2 are shown in Figure 4.1(a), respectively. The corresponding Raman spectra for these three cases are shown in Figure 4.1(b). In order to emphasis the quenching effect on fluorescence background from R6G molecules by MoS_2 nanosheets, the Raman spectrum of R6G molecules on SiO_2/Si substrate is also given for reference. From Figure 4.1(b), it is obvious that the Raman spectrum of R6G molecules on 1L P-MoS_2 sample is very weak and almost ignorable although the fluorescence background from R6G molecules is suppressed. However, the intensities of Raman modes from R6G molecules on both OT-MoS_2 and AT-MoS_2 substrates are enhanced with much more obvious quenching of fluorescence background of R6G molecules when compared to that of R6G molecules on P-MoS_2. The previous works presented that the structural disorder could improve the charge transfer process between adsorbates and detected molecules, and thus enhanced the Raman intensities of detected molecules [192, 196, 197]. Since the thickness of 1L MoS_2 is only ~0.65 nm, the defects are easily introduced during the plasma treatment process, thus the defects induced charge redistribution in 1L MoS_2 should be the key factor to enhance the intensity of Raman modes of R6G molecules. In order to verify the proposal above, we will explain it by studying variation of the surface properties and optical spectra of MoS_2 nanosheets before and after plasma treatment.

Figure 4.2 shows the Raman and PL spectra of P-MoS_2 and OT (AT)-MoS_2 nanosheets. It can be seen obviously from the Raman spectra that the value of frequency difference between E^1_{2g} and A_{1g} modes becomes larger for the oxygen (argon) plasma treated samples. The similar effects on chemically exfoliated monolayer MoS_2 nanosheets was observed because of the existence of defects [56].

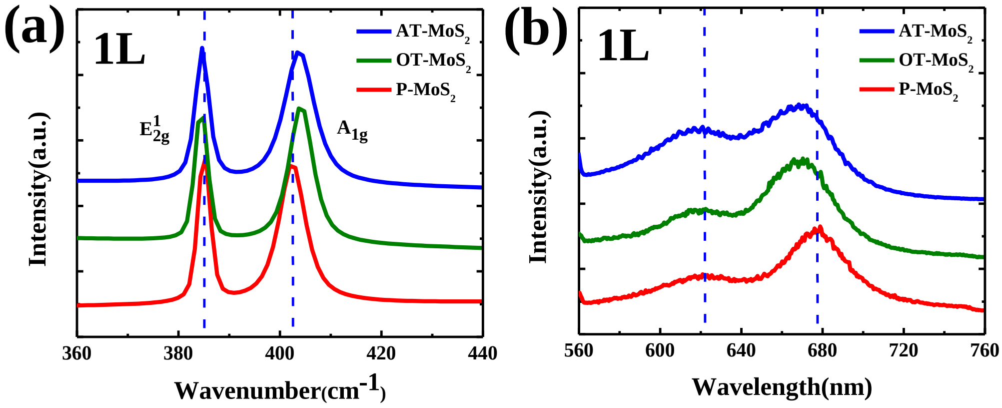

Figure 4.2 *Raman spectra of 1L (a) P-MoS_2 and OT(AT)-MoS_2. The corresponding PL spectra of 1L P-MoS_2 and OT(AT)-MoS_2 are shown in (b). The blue dashed lines represent the Raman and PL peak positions from P-MoS_2 samples, respectively.*

MoS_2 nanosheets grown by CVD technique also show a larger frequency difference between E^1_{2g} and A_{1g} modes when compared to that of MoS_2 samples prepared by ME method [198, 199]. All of these works attributed such a larger frequency difference to the structure disorder in atomically thin MoS_2 nanosheets. The AFM images of 1L P-MoS_2 and OT (AT)-MoS_2 nanosheets are displayed in Figure 4.3. Obviously, the surface of 1L OT (AT)-MoS_2 becomes rough when compared to that of P-MoS_2. The mean square roughness values for these three kinds of samples are 0.171 (P-MoS_2), 0.543 (OT-MoS_2) and 0.621nm (AT-MoS_2), respectively. Since the surface mean square roughness was increased, the surface disorder is indeed introduced into the surface of MoS_2 nanosheets during oxygen (argon) plasma treatment process [199, 200].

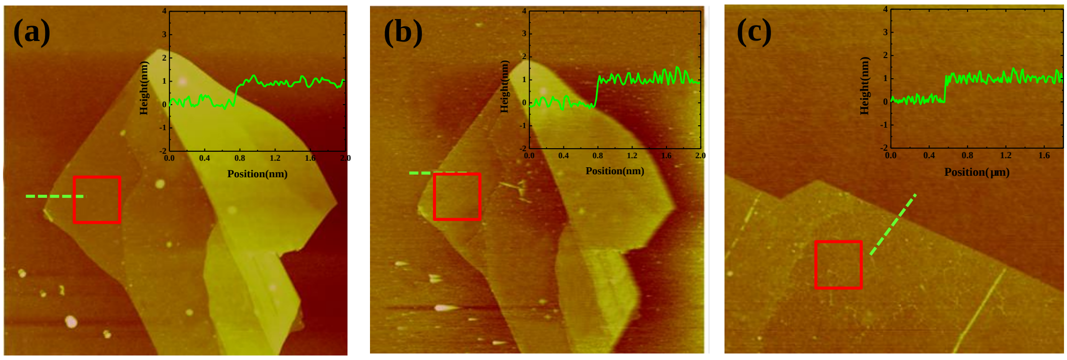

Figure 4.3 *AFM images of 1L P-MoS_2 and OT (AT)-MoS_2 nanosheets. The insets are the height profiles of these three samples, corresponding to the dashed lines shown in these three figures. The red squares in each figure means the selected area of calculating the mean roughness values.*

In particular, the E^1_{2g} mode doesn't show obvious shift but A_{1g} mode shows an obvious blue shift for plasma treated sample when compared with the pristine samples. Moreover, the peak width of A_{1g} mode in AT-MoS_2 is larger than that of the pristine sample while the peak width of A_{1g} mode in OT-MoS_2 is almost the same as that of the pristine one. Both of these features mean that the doping behaviors for these two different plasma treatments are different. Actually, the argon plasma treatment is a physical process to destroy the pristine structure of MoS_2 while the oxygen plasma is a chemical etching process. In order to investigate how the defects affect the optical properties of MoS_2, in this work we considered the possible point defects in plasma treated MoS_2, a single S vacancy, a single Mo vacancy and two S vacancies at the same side and different sides, as shown in Figure 4.4. The formation energy is defined as follows [201]:

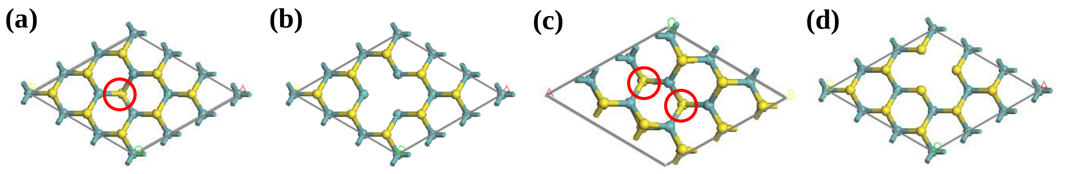

S Vacancy: 1.31 eV S_2 Vacancy: 8.07 eV S_2 Vacancy: 8.25 eV Mo Vacancy: 12.29 eV

Figure 4.4 *Formation energy of considered point defects in plasma treated single layer* MoS_2*. (a) single S vacancy; (b) double S vacancies at different side; (c) two S vacancies at the same side; (d)single Mo vacancy.*

$$\varDelta E_{\mathrm{Form}}=E_{\mathrm{System}}-N_{\mathrm{S}}\times E_{\mathrm{S\_ML}}-N_{\mathrm{Mo}}\times E_{\mathrm{Mo\_ML}}$$

$$E_{\mathrm{S\_ML}}=E_{\mathrm{S(single)}}+1.5E_{\mathrm{Bond}}$$

$$E_{\mathrm{Mo\_ML}}=E_{\mathrm{Mo(single)}}+3E_{\mathrm{Bond}}$$

$$E_{\mathrm{Bond}}=(E_{\mathrm{ML}}-E_{\mathrm{Mo(single)}}-2E_{\mathrm{S(single)}})/6 \tag{4.3}$$

where E_{S_ML} and E_{Mo_ML} are the single atom energy of Mo and S in a perfect monolayer, respectively. It is obvious that the single S vacancy is the most common defect due to its lowest formation energies. For oxygen plasma treatment sample, the O adsorption on the surface of MoS_2 should be also considered since the oxygen plasma may contain several ions and neutrals, such as O, O^+, O^-, O^{2+}, O^{2-}, but the ions are in a minority in most of plasma traditions [202]. Because the Raman spectra shown in Figure 4.2 (a), and the AFM images shown in Figure 4.3, don't show obvious structural disorder [203], in the work, we only considered the two cases: oxygen doping and adsorption of O. Oxygen doping is considered as substituting one S atom with O atoms and the oxygen adsorption is to add an O atom on top of S atom, as shown in Figure 4.5. Actually, we have considered the different adsorption sites and got the conclusion that the most favorable adsorption site is to add an O atom on top of S atom (Figure 4.6). Where

$$E_f = E_{MoS_2O} - E_{MoS_2} - E_O \tag{4.4}$$

E_f means the binding energy of O and MoS_2, while E_{MoS_2O}, E_{MoS_2}, E_O represents the energies of system with O adsorption, MoS_2, and single O atom.

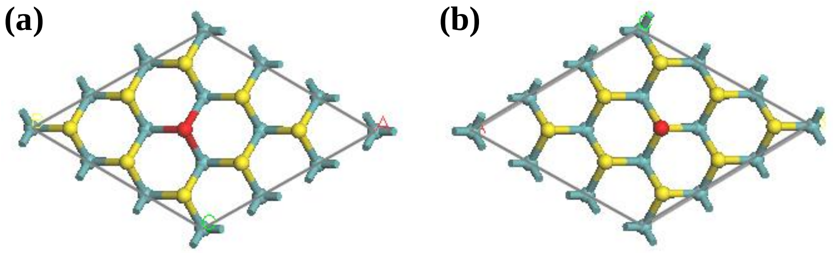

Figure 4.5 *(a) One S atom is substituted by O atom; (b) (2) an O atom is added on top of an S atom (the most favorable adsorption site. Other adsorption site is shown in Figure 4.6)*

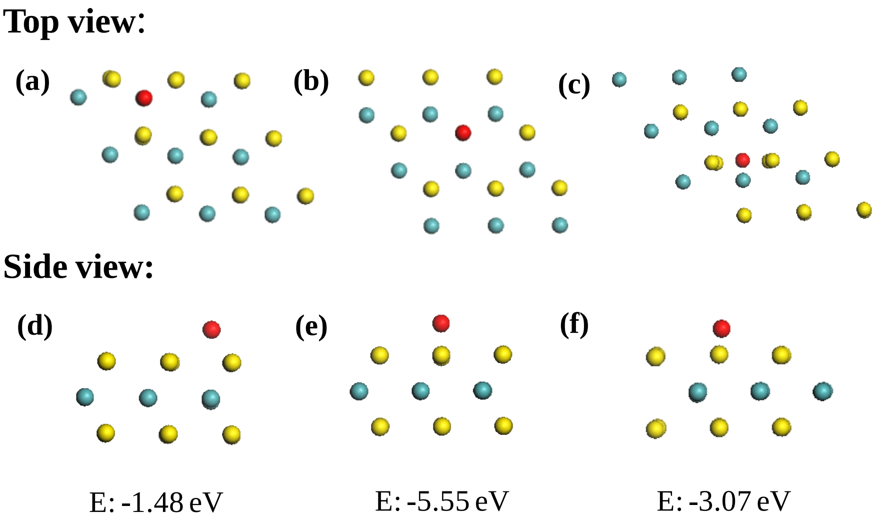

Figure 4.6 *Top view (a-c) and side view (d-f) of different O adsorption sites in 3x3x1 supercell. The stable adsorption site is on top of the S atom.*

In order to investigate whether substitute or adsorption plays a dominant role in oxygen plasma treatment process, we calculate the phonon frequencies of the E^1_{2g} and A_{1g} modes in these two cases. As shown in Table 4.1, the A_{1g} modes show blue shift for these two cases while, for E^1_{2g} mode, it shows a red shift for substitute doping and doesn't show obvious red shift for adsorption doping of O. When compared with the Raman spectra shown in Figure 4.2 (a), it could be inferred clearly that the adsorption of O on the surface of MoS_2 is the predominant doping way in defective way of oxygen plasma treated MoS_2.

Furthermore, Figure 4.2 (b) shows the PL spectra of 1L P-MoS_2 and OT (AT)-MoS_2 nanosheets. The positions of PL peaks taken from OT- and AT-MoS_2 show obvious blue shift when compared to that of P-MoS_2. Such a blue shift shown in PL spectra of T-MoS_2 is proposed that the band filling effect at the top of valence band contributes to this blue shift. The similar phenomena were reported in disordered InN micro-crystals [204], CdSe [205], and AlGaN/GaN [206, 207]. Since structure disorder is normal a chemically unstable site in atomically thin 2D material and these unstable site is easy to be adsorbed by adsorbates in air [208].

Cases	E_{2g} (cm^{-1})	A_{1g} (cm^{-1})
MoS_2	378.58	396.4
MoS+O	374.62	402.43
MoS_2+O	377.24	403.61

Table 4.1 *The frequency of E^1_{2g} and A_{1g} modes in monolayer MoS_2 with different doping form:* substitute *and adsorption of O on the surface of MoS_2.*

Most of previous works reported in detail how adsorbates affected the optical and electrical properties of MoS_2. The strong electro-negativity of the adsorbates on the surface of MoS_2 nanosheets leads to the p-doping effect to MoS_2 [209, 210]. In other words, the electron occupation level at the top of valence band is reduced due to the p doping effect of the adsorbates. In our work, the blue shift of PL peak observed in PL spectra of T-MoS_2 is due to the holes filling at the top of valance band, which increases the additional electronic transition energy. Interesting, when the optical spectra of OT (AT)-MoS_2 were measured in the vacuum environment (~$1x10^{-2}$ mbar), the blue shifted PL peak of T-MoS_2 compared to that of P-MoS_2 shows a red-shift. Particularly, as shown in Figure 4.7, the positions of PL peak taken from T-MoS_2 could shift towards the position as similar as that of P-MoS_2, which reveals the fact that the adsorbates on the surface of T-MoS_2 are desorbed in vacuum. Furthermore, once the samples were exposed in air again, an obviously blue-shift of PL peak position is observed again. Such a reversible shift observed in PL spectra of T-MoS_2 indicates that the adsorbates in air is weakly adsorbed at the unstable sites of T-MoS_2 [208].

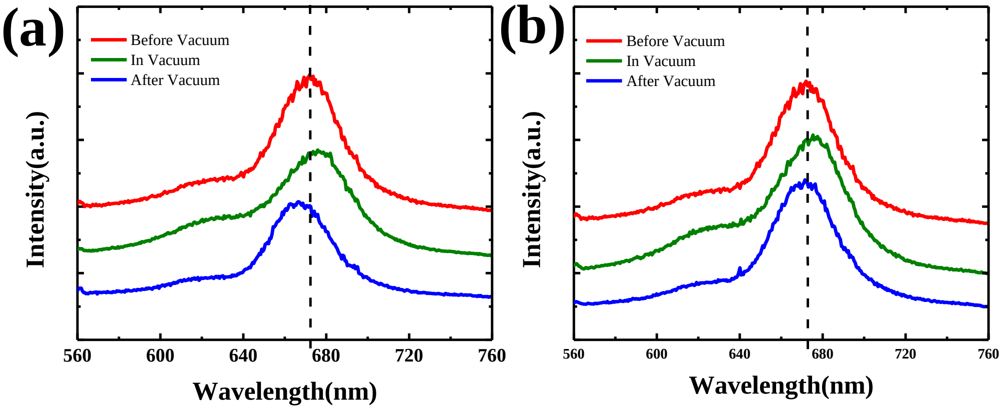

Figure 4.7 *PL spectra of 1L (a) OT-MoS_2 and (b) AT-MoS_2 samples. The red, green and blue lines represent the PL spectrum measured in air, in vacuum at $1x10^{-2}$ mbar and in air again.*

Next, the interactions between the R6G molecules and P(T)-MoS_2 are explored to investigate how the Raman signals are enhanced on T-MoS_2 nanosheets. In order to simplify the discussion here, only OT-MoS_2 nanosheets are discussed on behalf of T-MoS_2. As shown in Figure 4.8, the PL spectra of P-MoS_2, OT-MoS_2, and OT-MoS_2 samples with R6G molecules deposited on them were measured, respectively. After the deposition of R6G molecules on OT-MoS_2, the PL peak position of OT-MoS_2 shows a red-shift. As to this phenomenon, one possible reason is the occurrence of charge transfer between R6G molecules and OT-MoS_2.

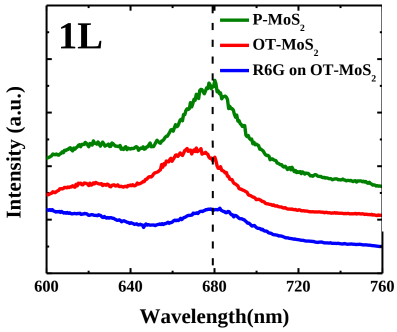

Figure 4.8 *PL spectra of P-MoS_2, OT-MoS_2, and R6G on OT-MoS_2, respectively. a) 1L MoS_2 case; b) 2L MoS_2 case; c) 3L MoS_2 case. The black dashed line represents the PL position of P-MoS_2 in each case.*

The density functional theory (DFT) was used to calculate the charge transfer between pristine (defective) MoS_2 and R6G molecule, as shown in Figure 4.9. The charge transfer between R6G molecule and pristine MoS_2 is 0.064e and that between R6G molecule and defective MoS_2 is 0.158e. In the case of chemical enhancement induced SERS, the charge transfer between the substrate and detected molecules plays a vital role. The increased separation between positive and negative charges results in an increase in molecular polarisability which has been related to a larger Raman scattering cross sections [211].

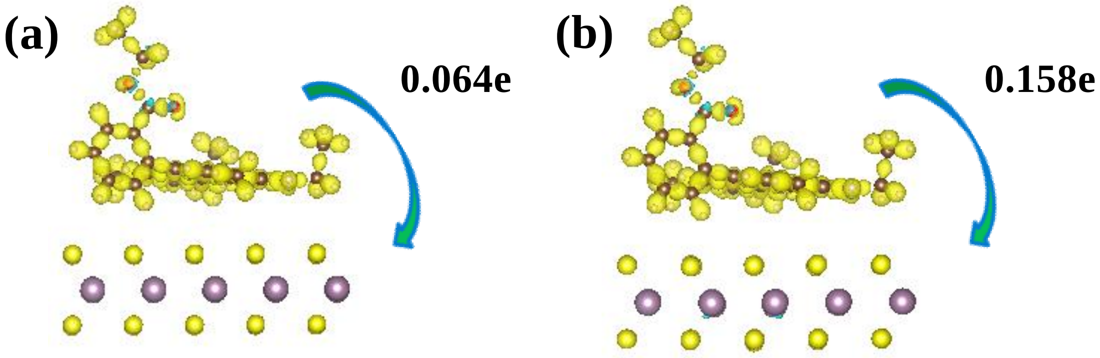

Figure 4.9 *Charge transfer between R6G molecules and pristine* MoS_2 *(a) and defective* MoS_2 *(b). Isosurface values are* $8x10^{-4}$ *e/*$Å^3$*.*

As to how the charge transfer Δq affects the polarisability, we could deduct from the relationship between the electrical field and the induced dipole moment.

$$P = \alpha \cdot E \qquad (4.5)$$

where α called as polarisability.

and $P = qr$. (q: charge, r: position operator, E: electric field) (4.6)

Thus, we can write the polarisability as $\alpha = q\,D$ (4.7)

Here, we define $D=r/E$, representing the displaceability of the charge. If we assume a ground-state charge transfer, we may write

$$(\alpha_{R6G})_{CT} = D_{R6G}\,(q_{R6G} - \Delta q) \qquad (4.8)$$

$$(\alpha_{S})_{CT} = D_{S}\,(q_{S} - \Delta q) \qquad (4.9)$$

the suffixes A and S denoting detected molecules (R6G) and substrate (MoS_2), respectively [93]. Δq represents the amount of charge transferred. The total polarisability of the system is the sum of both detected molecules and substrate. To calculate Raman scattering of detected molecules, we need to derive the total polarisability with respect to the normal coordinate Q_A.

$$\left(\frac{\partial\alpha(\mathrm{total})}{\partial Q_A}\right)_{CT} = \frac{\partial\alpha_A}{\partial Q_A}\left(1-\frac{\Delta q}{q_A}\right) + \frac{\partial\Delta q}{\partial q_A}\left(D_s - D_A\right) \tag{4.10}$$

(Here we assume Ds does not depend explicitely on Q_A, and total charge is conserved). Since the ground-state charge transfer is small, $\Delta q/q_A$ should be negligible, and formula (6) could be expressed as:

$$\left(\frac{\partial\alpha(\mathrm{total})}{\partial Q_A}\right)_{CT} = \frac{\partial\alpha_A}{\partial Q_A} + \frac{\partial\Delta q}{\partial q_A}\left(D_s - D_A\right) \tag{4.11}$$

Thus, the Raman polarisability of the complex system has a high relation with the charge transferred.

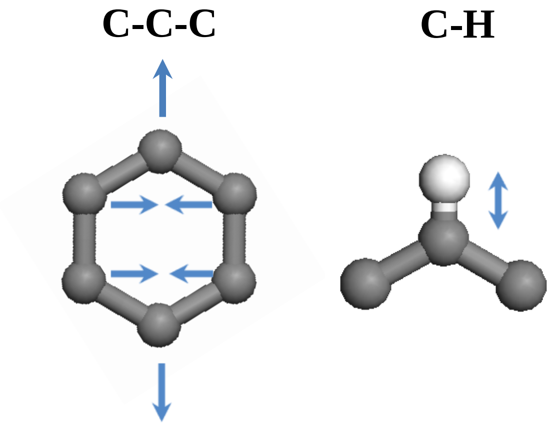

Figure 4.10 *Schematic of vibrational mode for in-plane deformation C-C-C vibration mode and C-H vibration mode of R6G molecules.*

Till now, the strong charge transfer between defective MoS_2 and R6G molecules is clarified. Moreover, the chemical structure of R6G molecule is similar to that of MoS_2, and the in-plane deformation C-C-C vibrational mode would be strongly enhanced because of the vibrational coupling between the R6G molecule and MoS_2. This explains the reason why the 612cm^{-1} peak is enhanced more than other modes shown in Figure 4.1, because this mode is assigned to the in-plane deformation C-C-C vibration (the assignment of R6G Raman modes are shown in Table 4.2), as shown in our experimental Figure 4.10, while the deformed in-plane C-H vibration does not show such a strong enhancement.

SERS Peaks (cm^{-1})	Peak Assignment
612	C-C-C ip
772	C-H op
1185	C-H ip
1306	arom C-C str
1362	arom C-C str
1502	arom C-C str
1570	arom C-C str
1647	arom C-C str

***Table 4.2** The assignment of vibration modes for R6G molecular is shown in this table. "ip" means in plane. "op" means out of plane. "arom C-C str" means aromatic C-C stretching vibration.*

Due to the contribution of defects on the enhanced SERs effect, thus SERS technique could be used to detect the possible defect in MoS_2 layer. As shown in Figure 4.11, the Raman mapping of single layer MoS_2 integrated with A_{1g} peak of MoS_2 is shown in figure 4.11 (a), which was taken on Witec 200 Raman system. The laser power was kept below 0.5mW to avoid heating effect on sample. From the mapping (Figure 4.11(a)), it shows the sample is uniform. However, when R6G molecules deposited on it, the Raman mapping integrated with the Raman modes from R6G molecules are shown in Figure 4.11 (b-d). Figure 4.11 (d) shows the single spectrum taken from the points A, B, C, respectively. The marked peaks I, II, III were used to integrated the Raman mapping (b), (c) and (d), respectively. Thus the defect induced enhance Raman scatting could be used as a well technique to probe crystal quality.

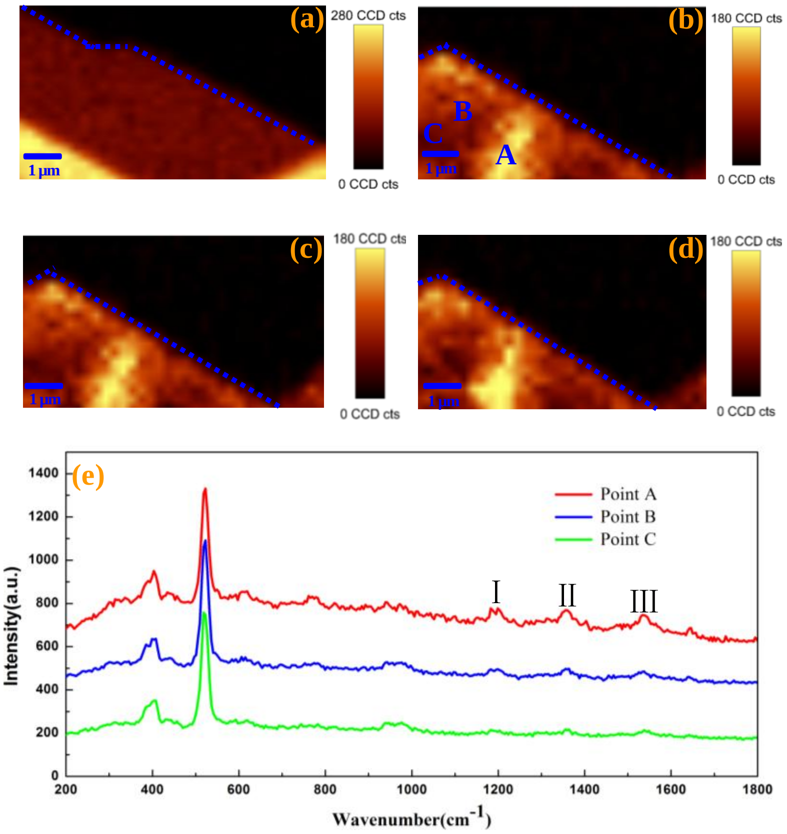

Figure 4.11 *(a) Raman mapping of single layer* MoS_2 *integrated with* A_{1g} *peak of* MoS_2*. (b-d) Raman mappings of the same samples integrated with the marked three peaks, I, II, III, shown in Figure (e). (e) The single Raman spectrum measured at the A, B, C points, respectively, shown in (b).*

4. 4 Conclusions

This work reported the SERS effect for R6G molecules observed on T-MoS_2 nanosheets. The Raman and PL spectra of both P-MoS_2 and OT (AT)-MoS_2 samples were systematically investigated, which revealed that the existence of defects in MoS_2

nanosheets. The disordered surface structures resulted in the introduction of defects which contributed to the enhanced charge transfer between R6G molecules and defective MoS_2. The first principle calculations on the charge transfer further confirm the improved charge transfer between R6G and MoS_2. The investigation of the interaction between MoS_2 (both P-MoS_2 and OT(AT)-MoS_2) and organic molecules provides a new way for the potential practical applications of MoS_2 nanosheets, such as molecule detection and biological detection.

Chapter 5

Origin of Strong PL spectra in CVD grown monolayer MoS_2

5.1 Motivation

Due to the limited size of mechanically exfoliated MoS_2 nanosheets, chemical vapor deposition (CVD) growth technique has been expected to grow large-area single layer MoS_2, as compared to the limited size of mechanically exfoliated (ME) MoS_2 [115-117, 119, 120]. The previous studies have reported several methods for growth of MoS_2 layers. Interestingly, CVD grown single layer MoS_2 nanosheets show a strong PL emission compared to that of ME samples, which is attributed to the high crystal quality of CVD samples [117, 199, 212, 213]. However, such an explanation is conflicted with the common sense that the exfoliated samples from the bulk phase should have high purity and crystal quality.

Actually, various defects, such as point defect, dislocations or grain boundaries, are reported in CVD samples [214-217]. In semiconductor materials, point defects in lattice, especially vacancies, can play an efficient role in trapping electrons, holes and excitons, and thus strongly affect the transport and optical behaviors of the host materials. If the bound excitons recombine radiatively, a PL peak would emit with the lower energy than the band gap edge transition [218]. The role of defects becomes more important in reduced-dimensionalities systems because of the tightly localized electron wave function [219]. Especially, the plasma treated monolayer MoS_2 shows a stronger PL intensity than that of as-prepared sample [220], which implies that the defects could enhance the intensity of PL emission in monolayer MoS_2. Given this measurement in atmospheric environment, it is hard to get the conclusion that the defects contribute to the enhanced PL intensity of MoS_2. Another paper performed an in-situ optical measurement in vacuum (~10^{-4} Torr) using a turbo-molecule pump [221]. They found the enhancement of PL intensity only be observed with the presence of pure N_2 gas, but cannot be observed on defective MoS_2 nanosheets without N_2 gas. Paradoxically, Wu et al. reported that the PL intensity of MoS_2 shows an obvious enhancement in the O_2 gas and air environment [222], rather than in N_2 gas. It is worth noting that all previous studies only focus on the ME MoS_2 sample. Till now, there is no comparable study on the optical spectra between CVD grown and ME MoS_2 samples. In this work, we compared the PL spectra of CVD grown and ME MoS_2 samples and measured the PL spectra of CVD grown and ME MoS_2 samples in vacuum and air, respectively, to investigate the effect of adsorbates. The electrical performance of CVD and ME MoS_2 samples shows their n type FETs behaviors and confirms the p doping effect of adsorbates on MoS_2. The behaviors of trion emission address the p doping effect of adsorbates, leading to the enhanced PL intensity in CVD grown MoS_2 sample. Combined with the calculation on the charge transfer between pristine (defective) MoS_2 and adsorbates, this work clarifies the strong PL emission of CVD grown MoS_2 samples and paves a way to engineer the PL intensity of the atomic MoS_2 layer, which provides a possibility of MoS_2 sample as light emitting devices.

5.2 Experimental section

Two groups of MoS_2 samples were used in this experiment. One group of MoS_2 samples were prepared by ME method from nature MoS_2 crystals (from SPI) and then transferred onto 270nm SiO_2/Si substrates, and the other group of MoS_2 samples were grown by CVD method by placing sulphur and MoO_3 powders in the furnace, with a SiO_2/Si substrate located face down above the MoO_3 powder. Raman and PL spectra were conducted on a Witec CRM 200 confocal microscopy Raman system. The excitation laser source was 532nm laser with a spot size about 500nm. To avoid damaging and heating by high power laser, the laser power was attenuated and the out power measured from the objective lens was controlled below 0.5mW. The accumulation time for PL and Raman spectra was 5s and 30s, respectively. The Raman signals were collected by an Olympus 100 × objective lens (NA =0.95) and dispersed by 1800 line mm^{-1} gratings before directed into CCD. The measurement condition of PL spectra is the same as that of the measurement of Raman spectra except the grating density with 150 line mm^{-1} for PL measurement. The vacuum experiments were carried out in a sealed LINKΛM stage combined with a controllable vacuum-level pump.

Both of these two groups of MoS_2 samples were deposited on 270nm SiO_2/Si substrates. The electrical contacts were fabricated by photolithography, and then followed by the pattern deposition of 10nm titanium and 120nm gold using thermal evaporation methods and then the lift off process followed. The final step was thermal annealing at 200℃ under a mixture of hydrogen and argon atmosphere to improve the contact performance. Electrical measurements were carried out with HP4156B Precision Semiconductor parameter Analyzer.

The charge transfer between MoS_2 and O_2 is calculated by first-principles calculations realized by Vienna ab initio Simulation Package (VASP), using the Perdew, Burke, and Ernzerfhof (PBE) potential. The cut-off energy for the basis set was 400 eV. The Brillouin-zone integration was performed scheme using a $5\times5\times1$ mesh within Gamma centered grids for a 4x4x1 supercell of MoS_2. The energy relaxation for each strain step is continued until the forces on all the atoms are converged to less than 10^{-2} eV $Å^{-1}$.

5.3 Result and discussion

As shown in Figure 5.1, the PL intensity of CVD grown monolayer MoS_2 is stronger (~16 times) than that of ME MoS_2 samples under the same measurement conditions. The first possible factor on the enhanced PL intensity is that the strain effect of substrate. It is well known that CVD grown samples are inevitably affected by the local strain because of the difference of thermal expansion coefficients between deposited MoS_2 layers and the substrates during cooling processes [115, 223, 224]. Such a strain effect of substrate leads to the frequency difference between E_{2g}^1 and A_{1g} modes of CVD grown monolayer MoS_2 larger than that of ME 1L MoS_2. The previous studies have investigated the strain effects on the PL spectra of MoS_2 layers [224-227]. No matter the tensile strain or compressive strain applied to MoS_2 layers, the intensities of PL spectra of MoS_2 indeed vary (increase with compressive strain applied and decrease with tensile strain applied), but the position of PL emission also changes a lot when strain is applied. The position of PL could shift towards higher energy (compressive strain) or lower energy (tensile strain) obviously, which is different from the comparison of PL spectra from CVD grown and ME MoS_2 sample shown in this Figure 5.1. In our work, the positions of PL peaks of both CVD grown and ME monolayer MoS_2 are almost identical. Moreover, when the strain applied to MoS_2, A_{1g} modes are unchanged and the E^1_{2g} mode shows an obvious red-shift [228, 229]. However, the E^1_{2g} and A_{1g} modes of CVD grown MoS_2 samples, show a red-shift and blue-shift, respectively, when compared with that of ME samples. Thus, the strain effect on Raman spectrum of CVD grown MoS_2 could be excluded here. Another possible reason contributing to enhanced PL intensity in CVD grown sample may be the introduced defects in it. As mentioned above, the defects can trap the exciton and act as a recombine center and thus, if they could recombine radiatively, the light emission will occur with energies lower than the energy of bandgap.

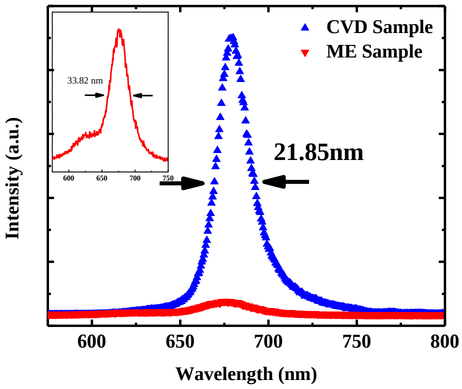

Figure 5.1 *Comparison of PL spectra between single layer ME and CVD grown* MoS_2.

However, in Figure 5.1, we didn't observe the extra excitonic peaks. Since the previous study reveals that the defects engineering and surface adsorption could contribute to the enhanced PL intensity of ME MoS_2 [220, 221]. Therefore, the reason why the PL intensity of CVD grown MoS_2 sample are dramatically stronger than that of ME MoS_2 sample is naturally inferred that the amounts of defects in CVD grown MoS_2 is much larger than that in ME MoS_2. The stoichiometry of the ME and CVD grown MoS_2 nanosheets has been characterized with energy dispersive spectroscopy (EDS) spectrum (Oxford INCA, England integrated on FESEM, JSM-7600F, JEOL), as shown in Figure 5.3. The S/Mo ratio is close to 2 (1.97) for the ME MoS_2 sample while for CVD grown MoS_2, the S/Mo ratio is only 1.83, which means more defect in CVD grown MoS_2.

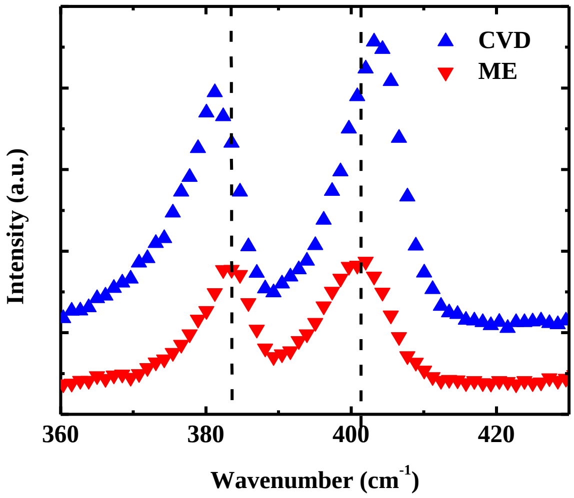

***Figure 5.2** Comparison of Raman spectra between ME and CVD grown single layer MoS_2:*

Moreover, the PL spectra of CVD grown and ME MoS_2 sample were measured in air and vacuum, respectively. As shown in Figure 5.4, the PL spectra of CVD grown monolayer MoS_2 measured in vacuum show obvious decrease of intensity which means the adsorbates adsorbed on the surface of MoS_2 highly affect the PL intensity of CVD grown MoS_2 sample. While for ME MoS_2 sample, when measured in vacuum and in air, respectively, its PL spectra don't show obvious variation on PL intensity.

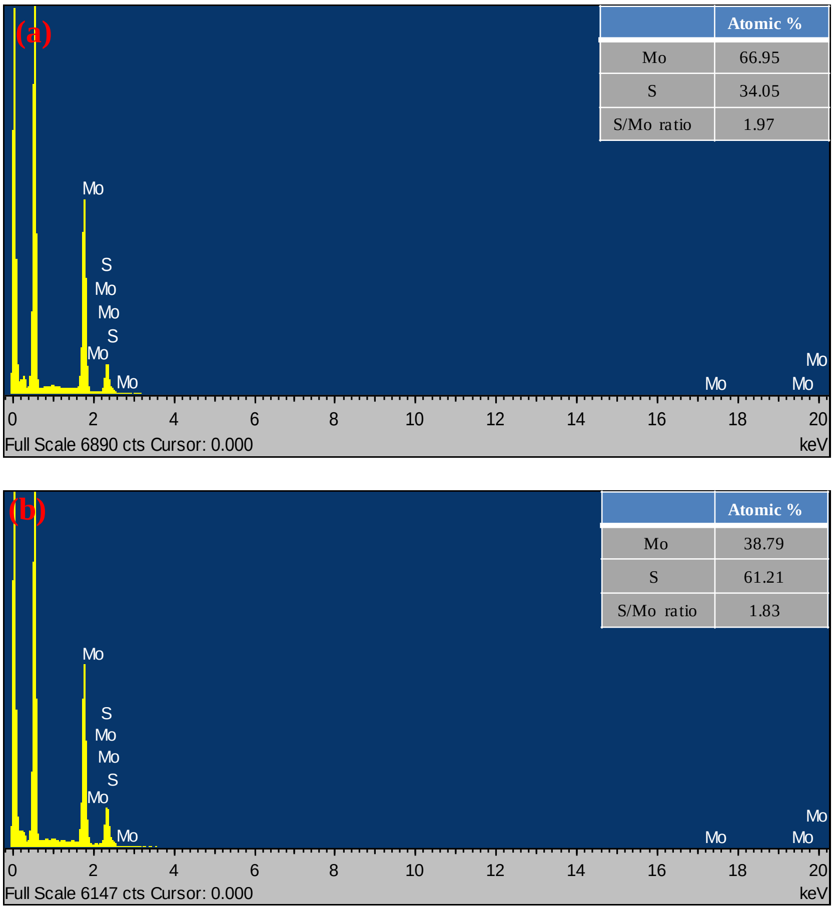

	Atomic %
Mo	66.95
S	34.05
S/Mo ratio	1.97

	Atomic %
Mo	38.79
S	61.21
S/Mo ratio	1.83

Figure 5.3 *SEM-EDS spectrum of single layer MoS_2. (a) ME MoS_2. (b) CVD grown MoS_2 sample. Inset shows the atomic percentage of S and Mo atoms in MoS_2 nanosheets.*

This result urges us to infer that more defects exist in CVD grown MoS_2 sample compared to the ME MoS_2 sample, thus the adsorption amount is greater in CVD grown MoS_2 sample than that of ME MoS_2 sample, since the samples mechanically exfoliated from natural crystal usually presents a better crystal quality than that of CVD grown samples. Therefore, the next questions are how the adsorbates affect the optical properties (PL) of CVD grown MoS_2 samples and why such an effect from adsorbates becomes little in vacuum.

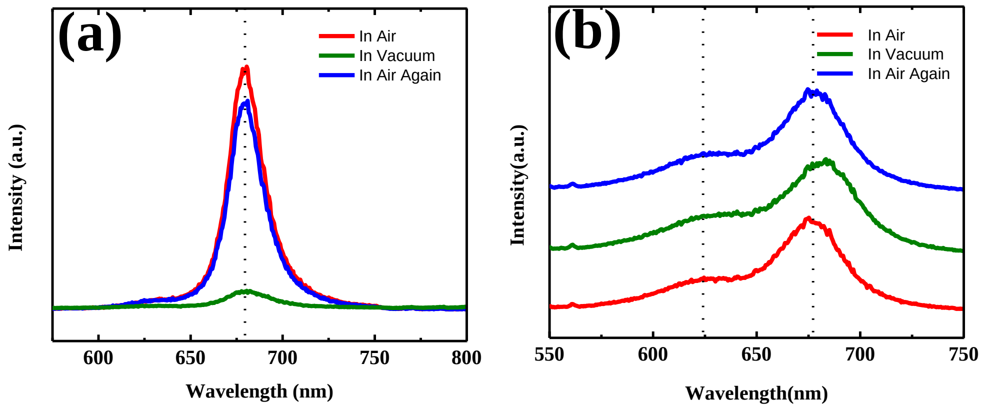

Figure 5.4 *PL spectra of CVD grown (a) and ME (b) MoS_2 samples measured in air, in vacuum and in air again.*

The Raman spectra of two groups of MoS_2 samples are investigated, shown in Figure 5.5. During the vacuum releasing process, there is no obvious change for E^1_{2g} mode (almost fixed at ~384.2cm^{-1}) in these two cases (ME and CVD grown samples), but with a clear blue-shift for A_{1g} mode from 401.1cm^{-1} to 402.3cm^{-1} for the CVD grown MoS_2 sample and no obvious change in ME sample (Figure 5.5 (a)). This result is different from the reported strain effect on the Raman spectra of monolayer MoS_2 sample [228]. The sensitivity of A_{1g} mode (out of plane) and the inertness of E^1_{2g} mode (in plane) to the adsorbates are related to their distinct vibration directions. We propose that the additional Coulomb potential imposed by the adsorbates could couples strongly with the A_{1g} phonon and then make the variation of A_{1g} mode much more obvious. In order to understand such a variation trend for E^1_{2g} and A_{1g} mode, a comprehensive study of electron-phonon coupling (EPC) as a function of concentration of electron doping has been investigated. The EPC of a mode ν with momentum q (with frequency ω_{qv}) is expressed as [230]:

$$\lambda_{qv} = \frac{2}{\hbar\omega_{qv}N(\epsilon_f)}\sum_{k}\sum_{mn}\left|g_{k+q,k}^{qv,ij}\right|^2 \times \delta(\epsilon_{k+q,i} - \epsilon_f) \times \delta(\epsilon_{k,j} - \epsilon_f) \quad (6.1)$$

where ω and $N(\epsilon_f)$ *are* the phonon frequency and density of states at the Fermi energy, respectively. ω_{qv} represents the frequency of a mode v with momentum q. The matrix element of ECP is given by

$$g_{k+q,k}^{qv,ij} = (\frac{\hbar}{2M\omega_{qv}})^{\frac{1}{2}}\langle\psi_{k+q,i}\left|\Delta V_{qv}\right|\psi_{k,j}\rangle \quad (6.2)$$

where $\psi_{k,j}$ represents the electronic wave function with wave vector k for band j, and M is the ionic mass. ΔV_{qv} is the variation of the self-consistent potential related to a phonon with wave vector q, branch v, and frequency ω_{qv}. Our results in Figure 5.5 (a) show the A_{1g} mode displays a blue-shift while the E^1_{2g} mode keeps almost unchanged. According to the symmetrical group theory, the A_{1g} mode has symmetrical lattice variation. Therefore, all electronic states with nonzero expectation value in equation (5.2) would contribute to the perturbation of the A_{1g} mode, which gives a strong EPC in equation (5.1).

The similar variation trend for A_{1g} mode has been reported on top gated Raman spectra from a single layer ME MoS_2 sample [231]. The in situ Raman spectrum measurements shows the softening of the A_{1g} mode with electron doping, while the E^1_{2g} mode remains unchanged. The authors believed that the A_{1g} mode could couples stronger with electrons, thus the electron doping results in the occupation of the conduction band minimum at *K* point which mainly consist of the character of d_{z^2} of Mo atom. Therefore the electron states $(|\psi(r)|^2)$ nearby also varies according to the

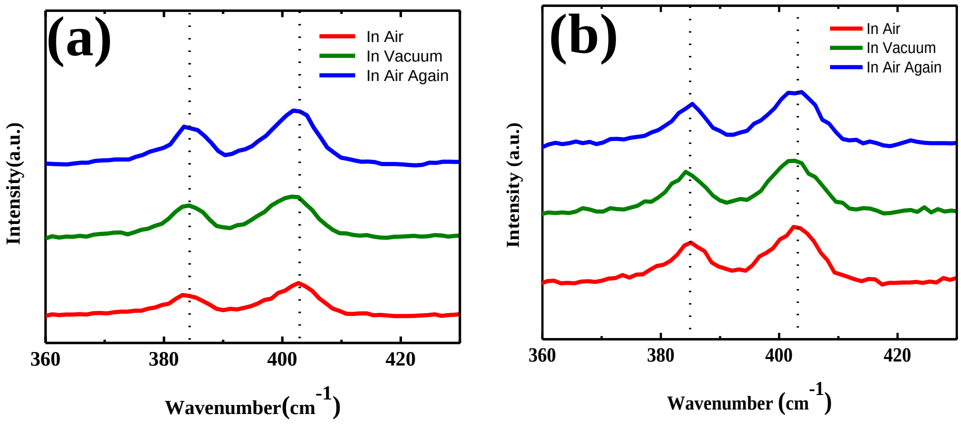

Figure 5.5 *The Raman spectra of CVD grown (a) and ME (b) monolayer* MoS_2 *samples measured in air, in vacuum and in air again.*

electron doping, which will leads to a change of the ECP for A_{1g} phonon due to the orthogonality of A_{1g} mode, as shown in equations (5.3) and (5.4), while the E^1_{2g} mode coupling with electrons weekly depends on doping. In this result, when the sample measured in air, the A_{1g} mode shifts toward high-energy direction compared with that measured in vacuum, which means a p doing effect of absorbates in air. In order to directly display the doping effect of adsorbates in air on the physical properties of MoS_2 sample, single layer MoS_2 FETs in our work were fabricated following the schematic graph shown in Figure 5.6 (a). The experimental details have been introduced in the experimental section. The inserted titanium thin film was used to decrease the contact resistance due to its low work function [232]. Figure 5.6 (b) and (c) show the electrical performance of single layer ME and CVD grown MoS_2, respectively. The two groups of MoS_2 samples based FETs both display n type channel behavior due to the increased current by the positive gate voltages. The electrical measurements were carried out in air and then followed by measurement in vacuum. The vacuum pressure was set at 10^{-2} mbar in our experiments. It is found that the threshold voltage shifts towards the positive direction.

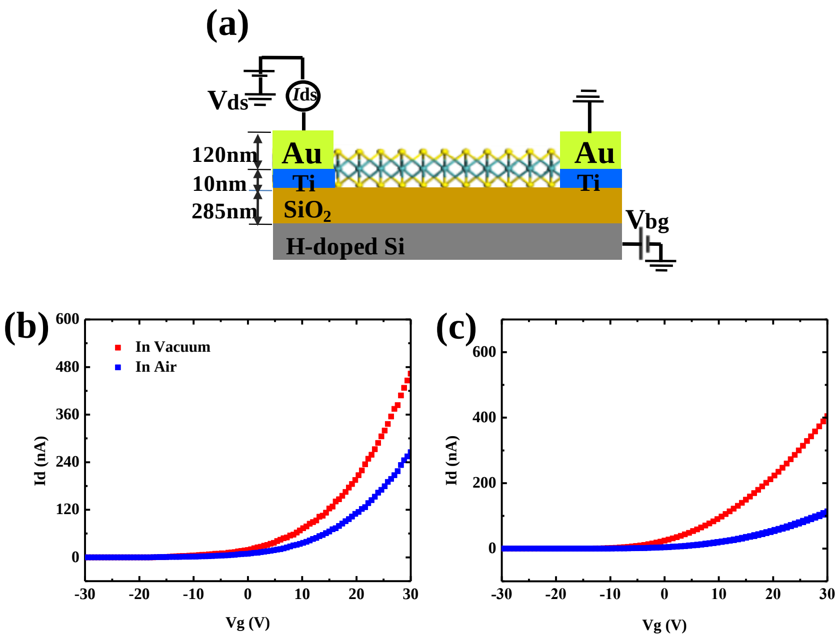

Figure 5.6 *(a) The schematic illustration of transistor based on ME and CVD grown single layer* MoS_2. I_d *-*V_g *characteristics of ME (b) and CVD grown (c)* MoS_2 *transistors for* V_{bg}*= -30V to 30V in step of 10V measured in air and vacuum, respectively. The fixed source-drain voltage is 1V.*

Since the devices exhibit n-type transistor, this shift reveals that the adsorbates in air into sulfur vacancies or defects sites on MoS_2 plays a p doping effect on CVD grown and ME monolayer MoS_2 samples.

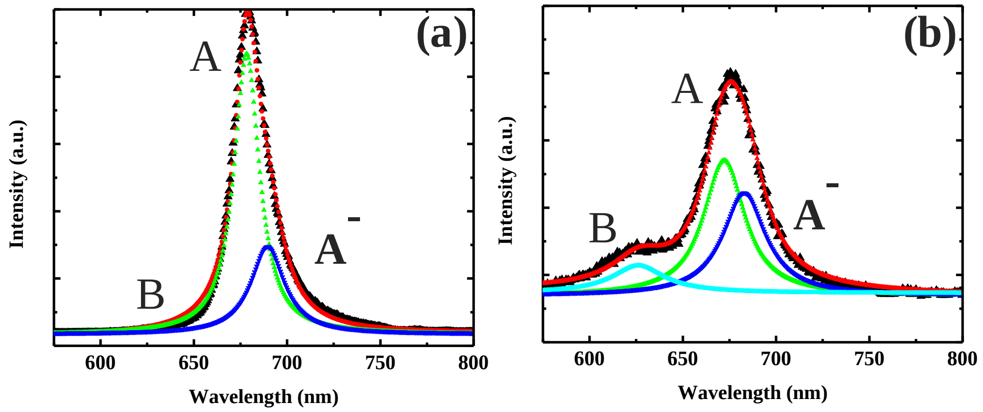

Figure 5.7 *The curve fitting results of PL spectra taken from CVD grown* MoS_2 *samples. (a) in air; (b) in vacuum;*

Now the problem need to be clarified is how the p doping effect of adsorbates from air affects the optical properties of CVD grown MoS_2 samples. When going back the PL spectra itself, we find that the peak emission from A exciton recombination is not symmetrical and a shoulder could be observed on the right side of this peak. The previous studies reported that the peak A may include two emission peaks, and they are from the recombination of exciton and trion, respectively. The gated PL spectra show that when the extra electron was injected in MoS_2, the feature of trion emission becomes clear [98, 99]. The chemical doping effects on the trion emission were also reported [233, 234]. When excess electrons are introduced to MoS_2 (this result has been confirmed by the n type behavior of CVD grown and ME MoS_2 samples based FETs), they will bind with photo-excited exciton (electron-hole pairs) to form trion. The negatively charged trions with bonded states of two electrons to a hole usually have finite binding energies, ~20meV, which makes them significant even at room temperature [98]. With the variation of carrier concentration in MoS_2 crystal introduced by the external doping, the exciton spectral weight in PL peak could be affected. In our experiment, due to the p doping effect of adsorbates in air, the amount of the excess electrons will be reduced and thus the PL emission from exciton will be enhanced. Such a transfer process could be described by a three-level model including the excitation, exciton emission and trion emission process, respectively [98, 234]. As shown in Figure 5.8, G represents the generation rate of optical excitons. The radiative decay rates of the exciton and trion are marked as Γ_{ex} and Γ_{tr}, respectively.

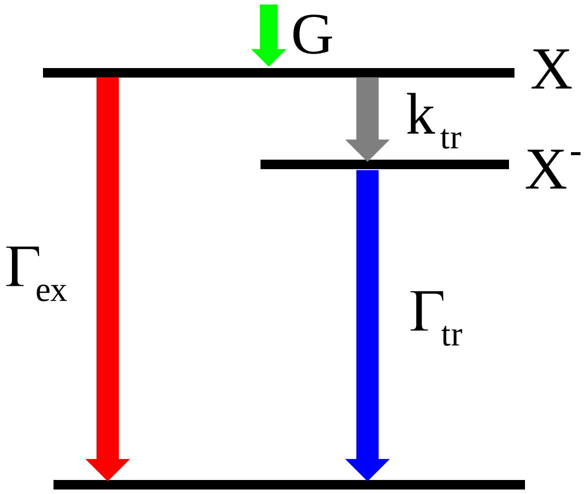

Figure 5.8 *Schematic of three-level energy diagram The radiatively decay rates of exciton and trion were denoted as* Γ_{ex} *and* Γ_{tr}*, respectively. G represents the generation rate of A excitons.* k_{tr} *is the formation rate of trion.*

When the mass action law is considered with trions together to evaluate the doped electron density in MoS_2 samples, the integrated intensity ratio of trion emission (I_{tr}) to electron emission (I_{ex}) can be expressed as [99, 234-236]:

$$\frac{I_{tr}}{I_{ex}} = \frac{\Gamma_{tr}}{\Gamma_{ex}} \left(\frac{\pi\hbar^2 m_{tr}}{4 m_{ex} m_e}\right) \frac{n_e}{k_b T} exp(\frac{E_b}{k_b T}) \tag{5.3}$$

m_{tr} and m_{ex} are the effective masses for trion and exciton, respectively. m_e is the effective mass of electrons. $\hbar$ is the reduced Planck's constant, k_b is the Boltzmann constant, T is the temperature, and E_b is the trion binding energy.

From the equation (5.3), it is obvious that the ratio of emission intensities between I_{tr} and I_{ex} is highly dependent on the carrier concentration. When the CVD grown MoS_2 samples were exposed in air, the p doping effect from the adsorbates in air reduced the concentration of electron, thus enhance the possibility of recombination of exciton. Till now, the physical picture on the reason why the CVD sample shows a strong PL intensity becomes clear. The amounts of defects in CVD sample is more, the amounts of adsorption is greater, and its PL intensity becomes stronger. Following this thought, if there is no adsorption on the surface of MoS_2, the PL intensity from ME and CVD grown MoS_2 samples should be almost the same.

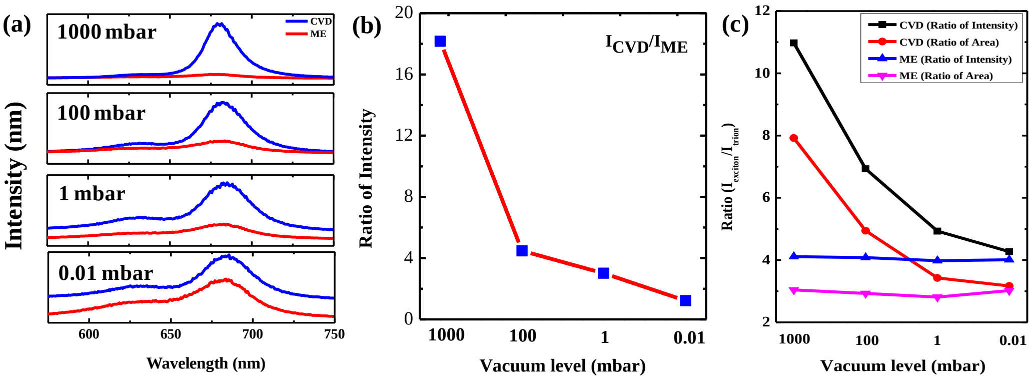

Figure 5.9 *(a) The PL spectra of CVD grown and ME MoS_2 samples at a series of different vacuum levels. (b) The ratio of PL intensities (CVD/ME) with the varied vacuum levels. (c) The intensity (area) ratios of $I_{exciton}/I_{trion}$.*

Figure 5.9 shows the ratio of PL intensities from CVD and ME MoS_2 samples at different vacuum levels, the variation trend from this figure shows that with the decrease of vacuum level, the ratio of PL intensities from CVD and ME samples are reaching to 1. This result further supports our proposal above.

For the components of adsorbates in air, we have calculated the charge transfer between O_2 (N_2) molecules and MoS_2 by first-principle methods. The configuration structure of O_2 (N_2) molecule adsorbed on perfect 4x4 super-cell of single layer MoS_2 are shown in Figure 5.10 (a) for O_2 and (b) for N_2. The adsorption sites in Figure 5.10 are the most favorable adsorption sites for O_2 and N_2, respectively. The possible other adsorption sites for O_2 on the surface of MoS_2 are shown in Figure 5.11. The charge transfer between O_2 and perfect MoS_2 is 0.045e (from MoS_2 to O_2, shown in Figure 5.10 (c)). While the amounts of charge transfer between N_2 and perfect MoS_2 is 0.008e (from MoS_2 to N_2, as shown in Figure 5.10 (d)). This suggests that O_2 molecules adsorbed on perfect MoS_2 are the major components of adsorbates. When we consider adsorbates on defective single layer MoS_2, the single sulfur vacancy on MoS_2 lattice is considered in our simulation as it is the most stable detective structure (Figure 5.4 in Chapter 5). The same super cell with a single S vacancy in 4x4 single layer MoS_2 with O_2 (N_2) adsorption is shown in Figure 5.12 (a) for O_2 and (b) for N_2. The charge transfer between O_2 molecule and MoS_2 with an S vacancy is 1.24e and that between N_2 molecule and MoS_2 with an S vacancy is 1.1e. Thus, the enhanced charge transfer from MoS_2 with an S vacancy to adsorbates (N_2 or O_2) reduces the extra electron concentration in defective MoS_2 sheets, and decreases the emission possibility of trion and increases that of exciton. From the charge transfer difference, it could be seen that the charge transfer is strongly localized at the defect site, which implies that the defect could be displayed a localization center. While, due to the high binding energy, such a localized exciton could trap electrons to form the stable localized exciton to avoid non-radiative recombination and thus enhance the PL intensity of MoS_2.

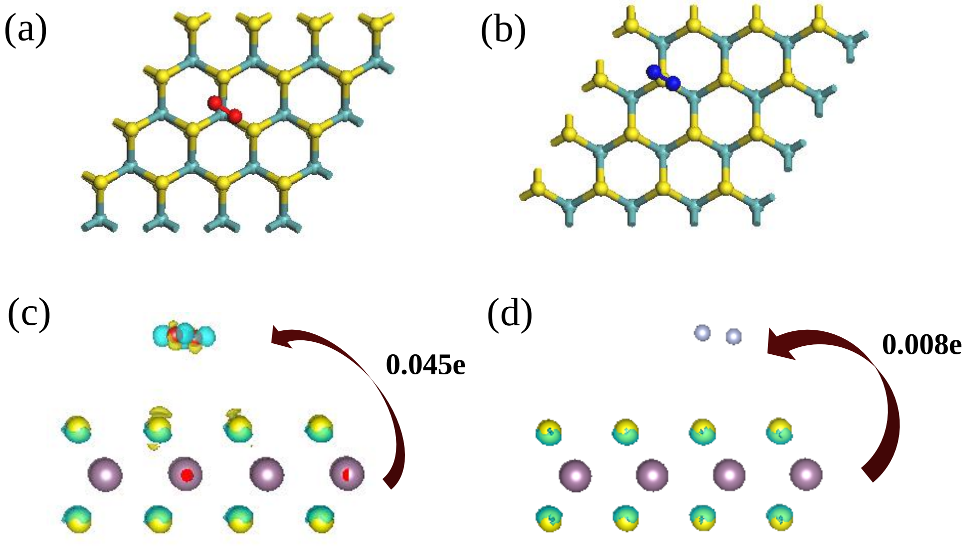

Figure 5.10 *The relaxed configuration structures and charge density difference of* O_2 *(a,c) and* N_2 *molecule (b,d) adsorbed on perfect single layer* MoS_2*. The positive and negative charges are shown in yellow and blue colors, respectively. Isosurface values are* $8x10^{-4}$ $e/Å^3$ *for (c) and (d).*

Top view:

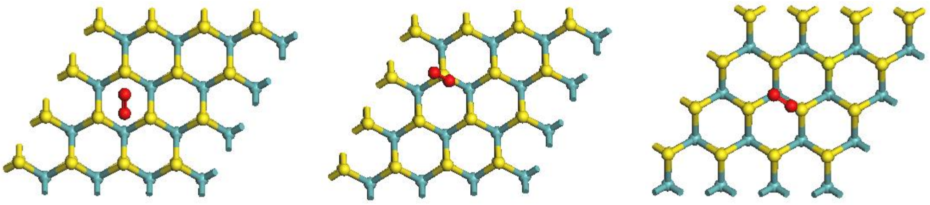

Side view:

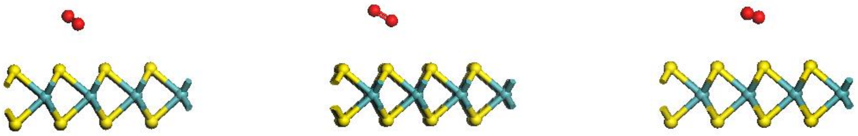

Figure 5.11 *Adsorption configurations. Top and side views of other possible adsorption sites of* O_2 (N_2) *on* MoS_2*.*

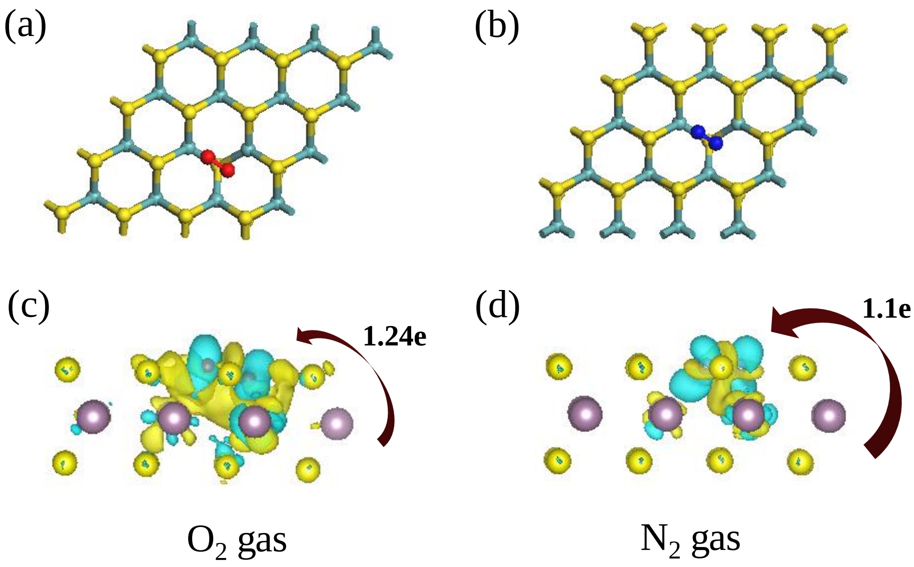

Figure 5.12 *The relaxed configuration structures and charge density difference of* O_2 *(a,c) and* N_2 *(b,d) molecule absorbed on single layer* MoS_2 *with a single S vacancy. The positive and negative charges are shown in yellow and blue colors, respectively. Isosurface values are* $2\text{x}10^{-3}$ *e/*Å^3 *for (c) and* $6\text{x}10^{-3}$ *e/*Å^3 *(d).*

From the discussion above, in the pristine single layer MoS_2, the interaction between O_2 and pristine MoS_2 plays a major role compared with that interaction between N_2 and pristine monolayer MoS_2, although such an interaction is very small and could be negligible. However, in the presence of S vacancies, both O_2 and N_2 show a strong charge transfer with the defective monolayer MoS_2. The discussion above clarifies the origin of adsorbates which could affect the physical properties of defective MoS_2.

5.4 Conclusions

By comparing the PL spectra of CVD grown and ME single layer MoS_2 sample, we found the strong PL emission from CVD grown MoS_2 sample. In order to investigate whether the CVD grown MoS_2 has a better or compatible crystal quality compared with ME MoS_2 sample, some possible reasons were investigated. We attributed the enhanced PL intensity of CVD grown sample to the adsorbates on the surface of MoS_2 by comparing their PL spectra measured in air and in vacuum. The following experiments, Raman, and electrical performance confirmed the p doping effects of adsorbates in air. Finally, the trion emission was introduced to explain the abnormally strong PL in CVD grown MoS_2. The first principle calculations were considered to investigate the charge transfer between MoS_2 and adsorbates and clarified the origin of adsorbates in air. This work can guide the future work on the engineering of PL emission of monolayer MoS_2.

Chapter 6
Summary and future plans

6.1 Summary

This thesis includes the fundamental studies of MoS_2, including the resonant Raman scattering and the comparison of photoluminescence (PL) spectra between chemical vapor deposition (CVD) grown and mechanical exfoliated (ME) MoS_2 and the potential application of MoS_2 in electronics and the substrate of surface enhanced Raman scattering (SERS) effect.

(1) Spin orbital splitting (SOS) revealed by resonant Raman scattering

The dramatically enhanced second order and combination Raman modes of E^1_{2g} and A_{1g} modes in monolayer and few layer MoS_2 excited by 325 nm laser were observed. When other laser lines used as excitation sources, 457 nm, 488 nm and 532 nm, respectively, no enhancement effect was observed for these three Raman modes. With considering spin orbital coupling effects, density functional theory based first principles calculation revealed the possible optical transition under 325nm laser excitation and the partial charge density of electronic bands confirmed the proposed model. The SOS at the top of the valence band is an essential prerequisite for the resonance of high-order Raman modes, and the energy value of SOS could be evaluated by such a resonant process.

(2) Plasma modified surface enhance Raman scattering (SERS) of R6G on MoS_2

In the second section, we revealed that the plasma treated MoS_2 nanosheets could be used as the substrate of SERS effect. The structural disorder created during plasma treating results in the generation of local dipoles, which contribute to the enhanced Raman signals from detected molecules. Therefore, the SERS effect could be used a method to probe the defects in MoS_2.

(3) Origin of strong PL in CVD grown monolayer MoS_2

In the first section, we revealed the fact that the strong PL emission from CVD grown MoS_2 is not its intrinsic behavior by measuring its PL spectra in vacuum and in air, respectively. It is obvious that the strong PL emission from CVD sample is due to the adsorbates in air. Such a doping effect affects the carrier concentration and then further affects the spectral weight of trion and exciton emission. Since the adsorbates are related to the active sites at the location of defects, so how to probe the defects in MoS_2 becomes important.

6.2 Future plans

(1) Construction of 2D hetero-structures and the exploration of their tailored properties

The 2D materials have displayed their interesting and abnormal physical properties and attract much more researchers to explore this research field [19, 237-239]. These crystals can be fabricated either by mechanically exfoliation from bulk materials [16, 18] or grown by several different methods, such as chemical vapor deposition [199], physical vapor deposition [240], atomic layer deposition [241, 242] or metal organic chemical vapor deposition methods [125]. The species of 2D materials are very great, expanding from metal, semiconductor, to insulator. But the physical properties they present are unique because of their special crystal structure. One of the ultimate goals for materials science is to develop novel architectures with tailored properties. However, these constructed materials do not exist in nature although they could usually present surprising breakthroughs with unusual dimensionality and complexity. The current strategies for the fabrication of artificial materials are as follows: (1) micro-mechanical exfoliation; (2) direct growth of stacked materials with different 2D materials; (3) substrate transfer technique [243-245].

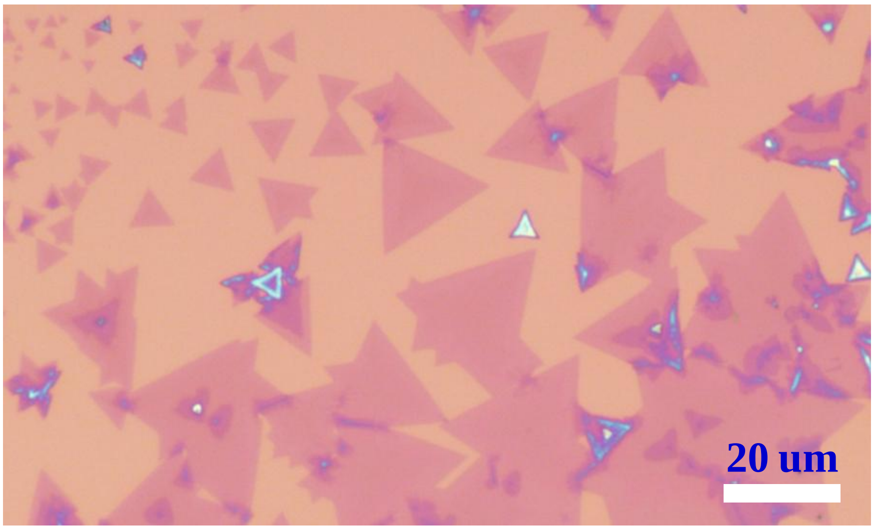

Figure 6.1 *The optical image of MoS_2/WS_2 hetero-junctions.*

As mentioned in chapter 2, CVD method has been employed to grow 2D materials in our current work. For the artificially complex materials, we have obtained several previous experimental results. As shown in Figure 6.1, the in plane hetero-junctions from MoS_2 and WS_2 monolayers were grown by our research group. The optical image of hetero-junctions was shown. Figure 6.2 showed the Raman and PL mapping of hetero-junctions, respectively. We hope that CVD method would be widely used to get much more hetero-junctions from different 2D materials. This study may pave the way for constructing artificial materials according to the practical application and open a new chapter in condensed matter research.

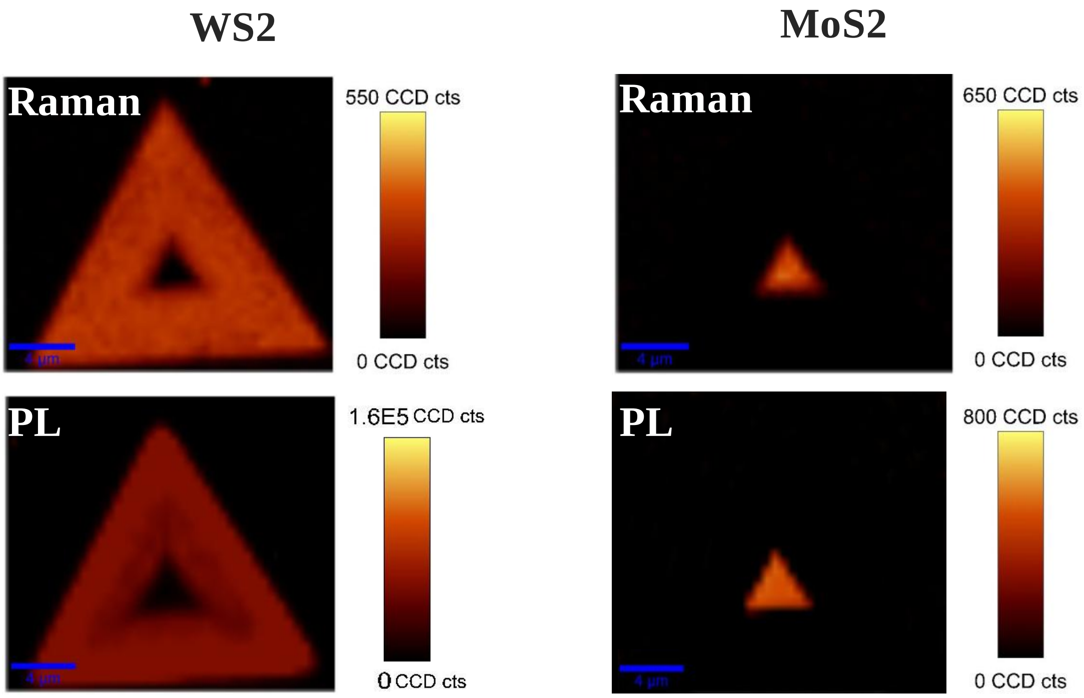

Figure 6.2 *Raman and PL mapping of a typical* MoS_2/WS_2 *hetero-junction. The left column shows the Raman and PL mapping of* WS_2 *and the right one shows that of* MoS_2*. Both of Raman mappings of* WS_2 *and* MoS_2 *were integrated by* A_{1g} *phonon, while both of PL mappings of* WS_2 *and* MoS_2 *were integrated by A exciton emission peak, respectively.*

(2) The behaviours of MoS_2 under high pressure

High pressure techniques have become one of the most probes to study the physical properties of materials under extreme conditions, particularly for the study of some phase change materials since most of them have necessary properties for the application in electronic memory devices [246-250].

Moreover, by studying the properties of materials under high pressure, some confusable problems under general conditions would be clarified. For example, the origin of indirect transition in multilayer MoS_2 layers has been confused on the location of conduction band minimum (CBM). Some calculations showed that the CBM was located at the K points while other results showed that it was at the point Λ in the Brillouin zone [42, 43, 101, 102]. While the PL spectrum of few layer MoS_2 measured under high pressure clarifies this confusion. We have got some results on the Raman and PL spectra of monolayer MoS_2 under high pressure, as shown in Figure 6.3.

We will continue our work to study the ultra-low frequency vibration modes under high pressure since the ultra-low frequency Raman mode is usually sensitive to the structure variation of materials.

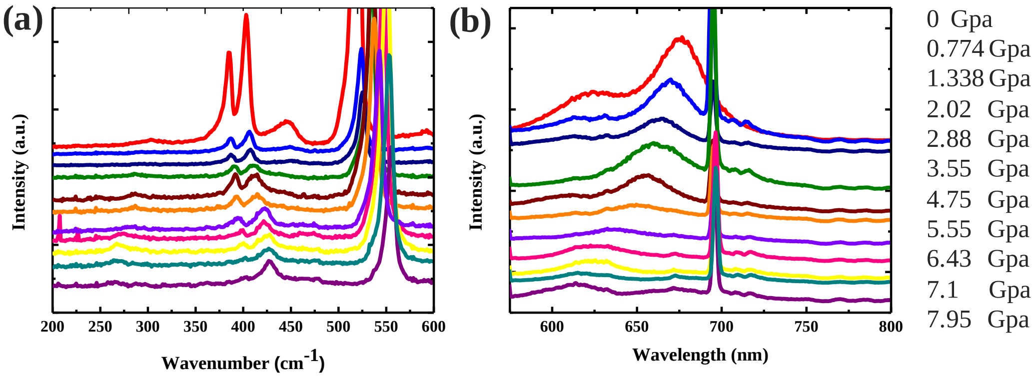

Figure 6.3 *Raman (a) and PL (b) spectra of single layer MoS_2 under different pressure level.*

References

1. Moore, G.E. *Progress in digital integrated electronics*. in *Electron Devices Meeting, 1975 International*. 1975.
2. Moore, G.E., *Cramming More Components Onto Integrated Circuits.* Proceedings of the IEEE, 1998. **86**(1): p. 82-85.
3. Lloyd, S., *Ultimate physical limits to computation.* Nature, 2000. **406**(6799): p. 1047-1054.
4. Rogers, J.A. and Y. Huang, *A curvy, stretchy future for electronics.* Proceedings of the National Academy of Sciences, 2009. **106**(27): p. 10875-10876.
5. Novoselov, K.S., et al., *Two-dimensional atomic crystals.* Proceedings of the National Academy of Sciences of the United States of America, 2005. **102**(30): p. 10451-3.
6. Castro Neto, A.H., et al., *The electronic properties of graphene.* Reviews of Modern Physics, 2009. **81**(1): p. 109-162.
7. Novoselov, K.S., et al., *Two-dimensional gas of massless Dirac fermions in graphene.* Nature, 2005. **438**(7065): p. 197-200.
8. Zhang, Y., et al., *Experimental observation of the quantum Hall effect and Berry's phase in graphene.* Nature, 2005. **438**(7065): p. 201-204.
9. Chernyshov, A., et al., *Evidence for reversible control of magnetization in a ferromagnetic material by means of spin-orbit magnetic field.* Nat Phys, 2009. **5**(9): p. 656-659.
10. Zhou, S.Y., et al., *Substrate-induced bandgap opening in epitaxial graphene.* Nature materials, 2007. **6**(10): p. 770-775.
11. Zhang, Y., et al., *Direct observation of a widely tunable bandgap in bilayer graphene.* Nature, 2009. **459**(7248): p. 820-823.
12. Han, M.Y., et al., *Energy Band-Gap Engineering of Graphene Nanoribbons.* Physical review letters, 2007. **98**(20): p. 206805.
13. Son, Y.W., M.L. Cohen, and S.G. Louie, *Energy gaps in graphene nanoribbons.* Physical review letters, 2006. **97**(21): p. 216803.
14. Li, X., et al., *Chemically Derived, Ultrasmooth Graphene Nanoribbon Semiconductors.* Science, 2008. **319**(5867): p. 1229-1232.
15. Jiao, L., et al., *Narrow graphene nanoribbons from carbon nanotubes.* Nature, 2009. **458**(7240): p. 877-880.
16. RadisavljevicB, et al., *Single-layer* MoS_2 *transistors.* Nat Nano, 2011. **6**(3): p. 147-150.
17. Mak, K.F., et al., *Atomically Thin* MoS_2*: A New Direct-Gap Semiconductor.* Physical review letters, 2010. **105**(13): p. 136805.
18. Lee, C., et al., *Anomalous Lattice Vibrations of Single- and Few-Layer* MoS_2*.* ACS nano, 2010. **4**(5): p. 2695-2700.
19. Wang, Q.H., et al., *Electronics and optoelectronics of two-dimensional transition metal dichalcogenides.* Nat Nano, 2012. **7**(11): p. 699-712.
20. Eda, G. and S.A. Maier, *Two-Dimensional Crystals: Managing Light for Optoelectronics.* ACS nano, 2013. **7**(7): p. 5660-5665.
21. Jariwala, D., et al., *Emerging Device Applications for Semiconducting Two-Dimensional Transition Metal Dichalcogenides.* ACS nano, 2014. **8**(2): p. 1102-1120.
22. Chhowalla, M., Z. Liu, and H. Zhang, *Two-dimensional transition metal dichalcogenide (TMD)*

nanosheets. Chemical Society Reviews, 2015. **44**(9): p. 2584-2586.

23. Tan, C. and H. Zhang, *Two-dimensional transition metal dichalcogenide nanosheet-based composites.* Chemical Society Reviews, 2015. **44**(9): p. 2713-2731.
24. Lv, R., et al., *Transition Metal Dichalcogenides and Beyond: Synthesis, Properties, and Applications of Single- and Few-Layer Nanosheets.* Accounts of Chemical Research, 2015. **48**(1): p. 56-64.
25. Wang, H., et al., *Integrated Circuits Based on Bilayer* MoS_2 *Transistors.* Nano Letters, 2012. **12**(9): p. 4674-4680.
26. Yoon, Y., K. Ganapathi, and S. Salahuddin, *How Good Can Monolayer* MoS_2 *Transistors Be?* Nano Letters, 2011. **11**(9): p. 3768-3773.
27. Li, H., et al., *Fabrication of Single- and Multilayer* MoS_2 *Film-Based Field-Effect Transistors for Sensing NO at Room Temperature.* Small, 2012. **8**(1): p. 63-67.
28. He, Q., et al., *Fabrication of Flexible* MoS_2 *Thin-Film Transistor Arrays for Practical Gas-Sensing Applications.* Small, 2012. **8**(19): p. 2994-2999.
29. Xiao, J., et al., *Exfoliated* MoS_2 *Nanocomposite as an Anode Material for Lithium Ion Batteries.* Chemistry of Materials, 2010. **22**(16): p. 4522-4524.
30. Hwang, H., H. Kim, and J. Cho, MoS_2 *Nanoplates Consisting of Disordered Graphene-like Layers for High Rate Lithium Battery Anode Materials.* Nano Letters, 2011. **11**(11): p. 4826-4830.
31. Shanmugam, M., C.A. Durcan, and B. Yu, *Layered semiconductor molybdenum disulfide nanomembrane based Schottky-barrier solar cells.* Nanoscale, 2012. **4**(23): p. 7399-7405.
32. Fortin, E. and W.M. Sears, *Photovoltaic effect and optical absorption in* MoS_2*.* Journal of Physics and Chemistry of Solids, 1982. **43**(9): p. 881-884.
33. Li, Y., et al., MoS_2 *Nanoparticles Grown on Graphene: An Advanced Catalyst for the Hydrogen Evolution Reaction.* Journal of the American Chemical Society, 2011. **133**(19): p. 7296-7299.
34. Xiang, Q., J. Yu, and M. Jaroniec, *Synergetic Effect of* MoS_2 *and Graphene as Cocatalysts for Enhanced Photocatalytic* H_2 *Production Activity of* TiO_2 *Nanoparticles.* Journal of the American Chemical Society, 2012. **134**(15): p. 6575-6578.
35. Kim, Y., J.-L. Huang, and C.M. Lieber, *Characterization of nanometer scale wear and oxidation of transition metal dichalcogenide lubricants by atomic force microscopy.* Applied Physics Letters, 1991. **59**(26): p. 3404-3406.
36. Schwierz, F., *Graphene transistors.* Nat Nano, 2010. **5**(7): p. 487-496.
37. Gargini, P. *The International Technology Roadmap for Semiconductors (ITRS): "Past, present and future".* in *GaAs IC Symposium, 2000. 22nd Annual*. 2000.
38. Zeng, H., et al., *Valley polarization in* MoS_2 *monolayers by optical pumping.* Nat Nano, 2012. **7**(8): p. 490-493.
39. SuzukiR, et al., *Valley-dependent spin polarization in bulk* MoS_2 *with broken inversion symmetry.* Nat Nano, 2014. **9**(8): p. 611-617.
40. Mak, K.F., et al., *The valley Hall effect in MoS2 transistors.* Science, 2014. **344**(6191): p. 1489-1492.
41. Yun, W.S., et al., *Thickness and strain effects on electronic structures of transition metal dichalcogenides: 2H-*MoX_2 *semiconductors (M=Mo, W; X=S, Se, Te)* Physical Review B, 2012. **85**(3): p. 033305.
42. Kuc, A., N. Zibouche, and T. Heine, *Influence of quantum confinement on the electronic*

structure of the transition metal sulfide TS_2. Physical Review B, 2011. **83**(24): p. 245213.

43. Cheiwchanchamnangij, T. and W.R.L. Lambrecht, *Quasiparticle band structure calculation of monolayer, bilayer, and bulk MoS_2.* Physical Review B, 2012. **85**(20): p. 205302.
44. Mak, K.F., et al., *Control of valley polarization in monolayer MoS_2 by optical helicity.* Nat Nano, 2012. **7**(8): p. 494-498.
45. Liang, Y., et al., *Interlayer-Expanded Molybdenum Disulfide Nanocomposites for Electrochemical Magnesium Storage.* Nano Letters, 2015. **15**(3): p. 2194-2202.
46. Kumar, A. and P.K. Ahluwalia, *A first principle Comparative study of electronic and optical properties of 1H – MoS_2 and 2H – MoS_2.* Materials Chemistry and Physics, 2012. **135**(2–3): p. 755-761.
47. Zhang, X., et al., *Phonon and Raman scattering of two-dimensional transition metal dichalcogenides from monolayer, multilayer to bulk material.* Chemical Society Reviews, 2015. **44**(9): p. 2757-2785.
48. Molina-Sánchez, A. and L. Wirtz, *Phonons in single-layer and few-layer MoS_2 and WS_2.* Physical Review B, 2011. **84**(15): p. 155413.
49. Sahin, H., et al., *Anomalous Raman spectra and thickness-dependent electronic properties of WSe_2.* Physical Review B, 2013. **87**(16): p. 165409.
50. Feng, J., et al., *Strain-engineered artificial atom as a broad-spectrum solar energy funnel.* Nat Photon, 2012. **6**(12): p. 866-872.
51. Malard, L.M., et al., *Observation of intense second harmonic generation from MoS_2 atomic crystals.* Physical Review B, 2013. **87**(20): p. 201401.
52. Zhu, H., et al., *Observation of piezoelectricity in free-standing monolayer MoS_2.* Nat Nano, 2015. **10**(2): p. 151-155.
53. Wu, W., et al., *Piezoelectricity of single-atomic-layer MoS_2 for energy conversion and piezotronics.* Nature, 2014. **514**(7523): p. 470-474.
54. Wypych, F., T. Weber, and R. Prins, *Scanning Tunneling Microscopic Investigation of 1T-MoS_2.* Chemistry of Materials, 1998. **10**(3): p. 723-727.
55. Enyashin, A.N., et al., *New Route for Stabilization of 1T-WS_2 and MoS_2 Phases.* The Journal of Physical Chemistry C, 2011. **115**(50): p. 24586-24591.
56. Eda, G., et al., *Photoluminescence from Chemically Exfoliated MoS_2.* Nano Letters, 2011. **11**(12): p. 5111-5116.
57. Shirodkar, S.N. and U.V. Waghmare, *Emergence of Ferroelectricity at a Metal-Semiconductor Transition in a 1T Monolayer of MoS_2.* Physical review letters, 2014. **112**(15): p. 157601.
58. Song, I., C. Park, and H.C. Choi, *Synthesis and properties of molybdenum disulphide: from bulk to atomic layers.* RSC Advances, 2015. **5**(10): p. 7495-7514.
59. Splendiani, A., et al., *Emerging Photoluminescence in Monolayer MoS_2.* Nano Letters, 2010. **10**(4): p. 1271-1275.
60. Alidoust, N., et al., *Observation of monolayer valence band spin-orbit effect and induced quantum well states in MoX_2.* Nat Commun, 2014. **5**.
61. Liu, G.-B., et al., *Electronic structures and theoretical modelling of two-dimensional group-VIB transition metal dichalcogenides.* Chemical Society Reviews, 2015. **44**(9): p. 2643-2663.
62. Zhao, W., et al., *Evolution of Electronic Structure in Atomically Thin Sheets of WS_2 and WSe_2.* ACS nano, 2013. **7**(1): p. 791-797.
63. Sundaram, R.S., et al., *Electroluminescence in Single Layer MoS_2.* Nano Letters, 2013. **13**(4): p.

1416-1421.

64. Tsai, M.-L., et al., *Monolayer MoS_2 Heterojunction Solar Cells.* ACS nano, 2014. **8**(8): p. 8317-8322.

65. Lopez-Sanchez, O., et al., *Ultrasensitive photodetectors based on monolayer MoS_2.* Nat Nano, 2013. **8**(7): p. 497-501.

66. Cai, Y., et al., *Lattice vibrational modes and phonon thermal conductivity of monolayer MoS_2.* Physical Review B, 2014. **89**(3): p. 035438.

67. Ataca, C., et al., *A Comparative Study of Lattice Dynamics of Three- and Two-Dimensional MoS_2.* The Journal of Physical Chemistry C, 2011. **115**(33): p. 16354-16361.

68. Wieting, T.J. and J.L. Verble, *Infrared and Raman Studies of Long-Wavelength Optical Phonons in Hexagonal MoS_2.* Physical Review B, 1971. **3**(12): p. 4286-4292.

69. Cai, Y., et al., *Infrared reflectance spectrum of BN calculated from first principles.* Solid State Communications, 2007. **141**(5): p. 262-266.

70. Cai, Y., et al., *First-principles study of vibrational and dielectric properties of beta-Si_3N_4.* Physical Review B, 2006. **74**(17): p. 174301.

71. C. V. Raman, K.S.K., *A new type of secondary radiation.* Nature, 1928. **121**: p. 501.

72. Mandelstam, G.L.a.L., *A new occurrence in the light diffusion of crystals.* Naturwissenschaften, 1928. **16**: p. 557.

73. Smekal, A., *Zur Quantentheorie der Dispersion.* Naturwissenschaften, 1923. **11**(43): p. 873-875.

74. Das, R.S. and Y.K. Agrawal, *Raman spectroscopy: Recent advancements, techniques and applications.* Vibrational Spectroscopy, 2011. **57**(2): p. 163-176.

75. Lyon, L.A., et al., *Raman Spectroscopy.* Analytical Chemistry, 1998. **70**(12): p. 341-362.

76. Venkateswarlu, K., *Relative intensities of stokes and anti-stokes Raman lines in crystals.* Proceedings of the Indian Academy of Sciences - Section A, 1941. **13**(1): p. 64-67.

77. Ferrari, A.C., et al., *Raman Spectrum of Graphene and Graphene Layers.* Physical review letters, 2006. **97**(18): p. 187401.

78. Graf, D., et al., *Spatially Resolved Raman Spectroscopy of Single- and Few-Layer Graphene.* Nano Letters, 2007. **7**(2): p. 238-242.

79. Koh, Y.K., et al., *Reliably Counting Atomic Planes of Few-Layer Graphene (n > 4).* ACS nano, 2011. **5**(1): p. 269-274.

80. Li, H., et al., *From Bulk to Monolayer MoS_2: Evolution of Raman Scattering.* Advanced Functional Materials, 2012. **22**(7): p. 1385-1390.

81. Berkdemir, A., et al., *Identification of individual and few layers of WS_2 using Raman Spectroscopy.* Sci. Rep., 2013. **3**.

82. Wieting, T.J. and J.L. Verble, *Infrared and Raman Studies of Long-Wavelength Optical Phonons in Hexagonal MoS_2.* Physical Review B, 1971. **3**(12): p. 4286-4292.

83. Chen, J.M. and C.S. Wang, *Second order Raman spectrum of MoS_2.* Solid State Communications, 1974. **14**(9): p. 857-860.

84. Loudon, R., *The Raman effect in crystals.* Advances in Physics, 1964. **13**(52).

85. Chakraborty, B., et al., *Layer-dependent resonant Raman scattering of a few layer MoS_2.* Journal of Raman Spectroscopy, 2012: p. 1097-4555.

86. Frey, G.L., et al., *Raman and resonance Raman investigation of ${\mathrm{MoS}}_{2}$ nanoparticles.* Physical Review B, 1999. **60**(4): p. 2883-2892.

87. Sekine, T., et al., *Dispersive Raman Mode of Layered Compound 2H-MoS$_2$ under the Resonant Condition.* Journal of the Physical Society of Japan, 1984. **53**(2): p. 811-818.

88. Livneh, T. and E. Sterer, *Resonant Raman scattering at exciton states tuned by pressure and temperature in 2H-MoS$_2$.* Physical Review B, 2010. **81**(19): p. 195209.

89. Wakabayashi, N., H.G. Smith, and R.M. Nicklow, *Lattice dynamics of hexagonal MoS$_2$ studied by neutron scattering.* Physical Review B, 1975. **12**(2): p. 659-663.

90. Verble, J.L. and T.J. Wieting, *Lattice Mode Degeneracy in MoS$_2$ and Other Layer Compounds.* Physical review letters, 1970. **25**(6): p. 362-365.

91. Sourisseau, C., et al., *Second-order Raman effects, inelastic neutron scattering and lattice dynamics in 2H-WS$_2$.* Chemical Physics, 1991. **150**(2): p. 281-293.

92. Shinde, K., et al., *Basic Mechanisms of Photoluminescence*, in *Phosphate Phosphors for Solid-State Lighting*2012, Springer Berlin Heidelberg. p. 41-59.

93. A.R. Peaker, H.G.G., *Low-Dimensional Structures in Semiconductors: From Basic Physics to Applications.* Series B： Physics 1991. **281**.

94. *Front Matter A2 - Wooten, Frederick*, in *Optical Properties of Solids*1972, Academic Press. p. iii.

95. Lampert, M.A., *Mobile and Immobile Effective-Mass-Particle Complexes in Nonmetallic Solids.* Physical review letters, 1958. **1**(12): p. 450-453.

96. Kheng, K., et al., *Observation of negatively charged excitons in semiconductor quantum wells.* Physical review letters, 1993. **71**(11): p. 1752-1755.

97. Finkelstein, G., H. Shtrikman, and I. Bar-Joseph, *Optical Spectroscopy of a Two-Dimensional Electron Gas near the Metal-Insulator Transition.* Physical review letters, 1995. **74**(6): p. 976-979.

98. Mak, K.F., et al., *Tightly bound trions in monolayer MoS$_2$.* Nature materials, 2013. **12**(3): p. 207-211.

99. Ross, J.S., et al., *Electrical control of neutral and charged excitons in a monolayer semiconductor.* Nat Commun, 2013. **4**: p. 1474.

100. Lui, C.H., et al., *Trion-Induced Negative Photoconductivity in Monolayer MoS$_2$.* Physical review letters, 2014. **113**(16): p. 166801.

101. Ramasubramaniam, A., D. Naveh, and E. Towe, *Tunable band gaps in bilayer transition-metal dichalcogenides.* Physical Review B, 2011. **84**(20): p. 205325.

102. Komsa, H.-P. and A.V. Krasheninnikov, *Effects of confinement and environment on the electronic structure and exciton binding energy of MoS$_2$ from first principles.* Physical Review B, 2012. **86**(24): p. 241201.

103. Zhao, W., et al., *Origin of Indirect Optical Transitions in Few-Layer MoS$_2$, WS$_2$, and WSe$_2$.* Nano Letters, 2013. **13**(11): p. 5627-5634.

104. Dou, X., et al., *Tuning and Identification of Interband Transitions in Monolayer and Bilayer Molybdenum Disulfide Using Hydrostatic Pressure.* ACS nano, 2014. **8**(7): p. 7458-7464.

105. Ramasubramaniam, A., *Large excitonic effects in monolayers of molybdenum and tungsten dichalcogenides.* Physical Review B, 2012. **86**(11): p. 115409.

106. Ugeda, M.M., et al., *Giant bandgap renormalization and excitonic effects in a monolayer transition metal dichalcogenide semiconductor.* Nature materials, 2014. **13**(12): p. 1091-1095.

107. Zhang, C., et al., *Direct Imaging of Band Profile in Single Layer MoS$_2$ on Graphite: Quasiparticle Energy Gap, Metallic Edge States, and Edge Band Bending.* Nano Letters, 2014.

14(5): p. 2443-2447.

108. Shinada, M. and S. Sugano, *Interband Optical Transitions in Extremely Anisotropic Semiconductors. I. Bound and Unbound Exciton Absorption.* Journal of the Physical Society of Japan, 1966. **21**(10): p. 1936-1946.
109. Lin, Y., et al., *Dielectric Screening of Excitons and Trions in Single-Layer* MoS_2*.* Nano Letters, 2014. **14**(10): p. 5569-5576.
110. Zhang, C., H. Wang, and F. Rana. *Optical Spectroscopy of Excitons and Trions in Single Layer* MoS_2. in *CLEO: 2013*. 2013. San Jose, California: Optical Society of America.
111. Li, H., et al., *Preparation and Applications of Mechanically Exfoliated Single-Layer and Multilayer* MoS_2 *and* WSe_2 *Nanosheets.* Accounts of Chemical Research, 2014. **47**(4): p. 1067-1075.
112. Bang, G.S., et al., *Effective Liquid-Phase Exfoliation and Sodium Ion Battery Application of* MoS_2 *Nanosheets.* ACS Applied Materials & Interfaces, 2014. **6**(10): p. 7084-7089.
113. Varrla, E., et al., *Large-Scale Production of Size-Controlled* MoS_2 *Nanosheets by Shear Exfoliation.* Chemistry of Materials, 2015. **27**(3): p. 1129-1139.
114. Coleman, J.N., et al., *Two-Dimensional Nanosheets Produced by Liquid Exfoliation of Layered Materials.* Science, 2011. **331**(6017): p. 568-571.
115. Jeon, J., et al., *Layer-controlled CVD growth of large-area two-dimensional* MoS_2 *films.* Nanoscale, 2015. **7**(5): p. 1688-1695.
116. Zhang, W., et al., *High-Gain Phototransistors Based on a CVD* MoS_2 *Monolayer.* Advanced Materials, 2013. **25**(25): p. 3456-3461.
117. Dumcenco, D., et al., *Large-Area Epitaxial Monolayer* MoS_2*.* ACS nano, 2015. **9**(4): p. 4611-4620.
118. Schmidt, H., et al., *Transport Properties of Monolayer* MoS_2 *Grown by Chemical Vapor Deposition.* Nano Letters, 2014. **14**(4): p. 1909-1913.
119. Lee, Y.-H., et al., *Synthesis of Large-Area* MoS_2 *Atomic Layers with Chemical Vapor Deposition.* Advanced Materials, 2012. **24**(17): p. 2320-2325.
120. Najmaei, S., et al., *Vapour phase growth and grain boundary structure of molybdenum disulphide atomic layers.* Nature materials, 2013. **12**(8): p. 754-759.
121. van der Zande, A.M., et al., *Grains and grain boundaries in highly crystalline monolayer molybdenum disulphide.* Nature materials, 2013. **12**(6): p. 554-561.
122. Wang, X., et al., *Controlled Synthesis of Highly Crystalline MoS2 Flakes by Chemical Vapor Deposition.* Journal of the American Chemical Society, 2013. **135**(14): p. 5304-5307.
123. Feldman, Y., et al., *High-Rate, Gas-Phase Growth of* MoS_2 *Nested Inorganic Fullerenes and Nanotubes.* Science, 1995. **267**(5195): p. 222-225.
124. Cong, C., et al., *Synthesis and Optical Properties of Large-Area Single-Crystalline 2D Semiconductor* WS_2 *Monolayer from Chemical Vapor Deposition.* Advanced Optical Materials, 2014. **2**(2): p. 131-136.
125. Kang, K., et al., *High-mobility three-atom-thick semiconducting films with wafer-scale homogeneity.* Nature, 2015. **520**(7549): p. 656-660.
126. Tatarchenko, Y.A., *Shaped crystal growth.* Kluwer Academic Publishers, 1994.
127. Kullaiah Byrappa, T.O., *Crystal growth technology.* William Andrew publishing., 2003.
128. Cao, D., et al., *Role of Chemical Potential in Flake Shape and Edge Properties of Monolayer MoS2.* The Journal of Physical Chemistry C, 2015. **119**(8): p. 4294-4301.

129. Altavilla, C., M. Sarno, and P. Ciambelli, *A Novel Wet Chemistry Approach for the Synthesis of Hybrid 2D Free-Floating Single or Multilayer Nanosheets of MS_2@oleylamine (M═Mo, W).* Chemistry of Materials, 2011. **23**(17): p. 3879-3885.
130. Shen, X., H. Wang, and T. Yu, *How do the electron beam writing and metal deposition affect the properties of graphene during device fabrication?* Nanoscale, 2013. **5**(8): p. 3352-3358.
131. Kim, S., et al., *Realization of a high mobility dual-gated graphene field-effect transistor with Al_2O_3 dielectric.* Applied Physics Letters, 2009. **94**(6): p. 062107.
132. Klitzing, K.v., G. Dorda, and M. Pepper, *New Method for High-Accuracy Determination of the Fine-Structure Constant Based on Quantized Hall Resistance.* Physical review letters, 1980. **45**(6): p. 494-497.
133. Bernevig, B.A., T.L. Hughes, and S.-C. Zhang, *Quantum Spin Hall Effect and Topological Phase Transition in HgTe Quantum Wells.* Science, 2006. **314**(5806): p. 1757-1761.
134. König, M., et al., *Quantum Spin Hall Insulator State in HgTe Quantum Wells.* Science, 2007. **318**(5851): p. 766-770.
135. Fu, L. and C.L. Kane, *Topological insulators with inversion symmetry.* Physical Review B, 2007. **76**(4): p. 045302.
136. Hsieh, D., et al., *A topological Dirac insulator in a quantum spin Hall phase.* Nature, 2008. **452**(7190): p. 970-974.
137. Murakami, S., N. Nagaosa, and S.-C. Zhang, *Dissipationless Quantum Spin Current at Room Temperature.* Science, 2003. **301**(5638): p. 1348-1351.
138. Sinova, J., et al., *Universal Intrinsic Spin Hall Effect.* Physical review letters, 2004. **92**(12): p. 126603.
139. Prinz, G., *Magnetoelectronics.* Science, 1998. **282**(5394): p. 1660.
140. Wolf, S.A., et al., *Spintronics: A Spin-Based Electronics Vision for the Future.* Science, 2001. **294**(5546): p. 1488-1495.
141. Liu, C., et al., *Quantum Spin Hall Effect in Inverted Type-II Semiconductors.* Physical review letters, 2008. **100**(23): p. 236601.
142. Du, L., et al., *Robust Helical Edge Transport in Gated InAs/GaSb Bilayers.* Physical review letters, 2015. **114**(9): p. 096802.
143. Liu, C.-C., W. Feng, and Y. Yao, *Quantum Spin Hall Effect in Silicene and Two-Dimensional Germanium.* Physical review letters, 2011. **107**(7): p. 076802.
144. Xiao, D., et al., *Interface engineering of quantum Hall effects in digital transition metal oxide heterostructures.* Nat Commun, 2011. **2**: p. 596.
145. Xu, Y., et al., *Large-Gap Quantum Spin Hall Insulators in Tin Films.* Physical review letters, 2013. **111**(13): p. 136804.
146. Weng, H., X. Dai, and Z. Fang, *Transition-Metal Pentatelluride $ZrTe_5$ and $HfTe_5$: A Paradigm for Large-Gap Quantum Spin Hall Insulators.* Physical Review X, 2014. **4**(1): p. 011002.
147. Cazalilla, M.A., H. Ochoa, and F. Guinea, *Quantum Spin Hall Effect in Two-Dimensional Crystals of Transition-Metal Dichalcogenides.* Physical review letters, 2014. **113**(7): p. 077201.
148. Kong, D. and Y. Cui, *Opportunities in chemistry and materials science for topological insulators and their nanostructures.* Nat Chem, 2011. **3**(11): p. 845-849.
149. Yang, K., et al., *A search model for topological insulators with high-throughput robustness descriptors.* Nature materials, 2012. **11**(7): p. 614-619.
150. Qian, X., et al., *Quantum spin Hall effect in two-dimensional transition metal dichalcogenides.*

Science, 2014. **346**(6215): p. 1344-1347.

151. Kane, C.L. and E.J. Mele, *Quantum Spin Hall Effect in Graphene.* Physical review letters, 2005. **95**(22): p. 226801.

152. Yao, Y., et al., *Spin-orbit gap of graphene: First-principles calculations.* Physical Review B, 2007. **75**(4): p. 041401.

153. Min, H., et al., *Intrinsic and Rashba spin-orbit interactions in graphene sheets.* Physical Review B, 2006. **74**(16): p. 165310.

154. Zhu, Z.Y., Y.C. Cheng, and U. Schwingenschlögl, *Giant spin-orbit-induced spin splitting in two-dimensional transition-metal dichalcogenide semiconductors.* Physical Review B, 2011. **84**(15): p. 153402.

155. LaShell, S., B.A. McDougall, and E. Jensen, *Spin Splitting of an Au(111) Surface State Band Observed with Angle Resolved Photoelectron Spectroscopy.* Physical review letters, 1996. **77**(16): p. 3419-3422.

156. Koroteev, Y.M., et al., *Strong Spin-Orbit Splitting on Bi Surfaces.* Physical review letters, 2004. **93**(4): p. 046403.

157. Ramakrishna Matte, H.S.S., et al., *MoS_2 and WS_2 Analogues of Graphene.* Angewandte Chemie International Edition, 2010. **49**(24): p. 4059-4062.

158. Hirsch, J.E., *Spin Hall Effect.* Physical review letters, 1999. **83**(9): p. 1834-1837.

159. Berger, L., *Emission of spin waves by a magnetic multilayer traversed by a current.* Physical Review B, 1996. **54**(13): p. 9353-9358.

160. Zhang, J., et al., *Topology-Driven Magnetic Quantum Phase Transition in Topological Insulators.* Science, 2013. **339**(6127): p. 1582-1586.

161. Sallen, G., et al., *Robust optical emission polarization in MoS${}_{2}$ monolayers through selective valley excitation.* Physical Review B, 2012. **86**(8): p. 081301.

162. Korn, T., et al., *Low-temperature photocarrier dynamics in monolayer MoS_2.* Applied Physics Letters, 2011. **99**(10): p. 102109.

163. Kresse, G. and J. Furthmüller, *Efficient iterative schemes for ab initio total-energy calculations using a plane-wave basis set.* Physical Review B, 1996. **54**(16): p. 11169-11186.

164. Kresse, G. and J. Furthmüller, *Efficiency of ab-initio total energy calculations for metals and semiconductors using a plane-wave basis set.* Computational Materials Science, 1996. **6**(1): p. 15-50.

165. Ni, Z.H., et al., *Graphene Thickness Determination Using Reflection and Contrast Spectroscopy.* Nano Letters, 2007. **7**(9): p. 2758-2763.

166. Li, S.-L., et al., *Quantitative Raman Spectrum and Reliable Thickness Identification for Atomic Layers on Insulating Substrates.* ACS nano, 2012. **6**(8): p. 7381-7388.

167. Castellanos-Gomez, A., N. Agrait, and G. Rubio-Bollinger, *Optical identification of atomically thin dichalcogenide crystals.* Applied Physics Letters, 2010. **96**(21).

168. Kadantsev, E.S. and P. Hawrylak, *Electronic structure of a single MoS_2 monolayer.* Solid State Communications, 2012. **152**(10): p. 909-913.

169. Stacy, A.M. and D.T. Hodul, *Raman spectra of IVB and VIB transition metal disulfides using laser energies near the absorption edges.* Journal of Physics and Chemistry of Solids, 1985. **46**(4): p. 405-409.

170. Alexandrou, A., et al., *Theoretical model of stress-induced triply resonant Raman scattering.* Physical Review B, 1989. **40**(3): p. 1603-1610.

171. Alexandrou, A., Y. Pusep, and M. Cardona, *Triply resonant second-order Raman scattering at the* E_0 *and* $E_0+\Delta_0$ *gap of GaP under uniaxial stress.* Physical Review B, 1989. **39**(12): p. 8308-8312.

172. Alexandrou, A. and M. Cardona, *Triply resonant second-order Raman scattering in GaAs.* Solid State Communications, 1987. **64**(7): p. 1029-1034.

173. Feng, W., et al., *Intrinsic spin Hall effect in monolayers of group-VI dichalcogenides: A first-principles study.* Physical Review B, 2012. **86**(16): p. 165108.

174. Kasowski, R.V., *Band Structure of* MoS_2 *and* NbS_2*.* Physical review letters, 1973. **30**(23): p. 1175-1178.

175. Kleinman, D.A., R.C. Miller, and A.C. Gossard, *Doubly resonant LO-phonon Raman scattering observed with GaAs-AlxGa1-xAs quantum wells.* Physical Review B, 1987. **35**(2): p. 664-674.

176. Cerdeira, F., et al., *Stress-induced doubly resonant Raman scattering in GaAs.* Physical review letters, 1986. **57**(25): p. 3209-3212.

177. Kaasbjerg, K., K.S. Thygesen, and K.W. Jacobsen, *Phonon-limited mobility in n-type single-layer* MoS_2 *from first principles.* Physical Review B, 2012. **85**(11): p. 115317.

178. Xiao, D., et al., *Coupled Spin and Valley Physics in Monolayers of* MoS_2 *and Other Group-VI Dichalcogenides.* Physical review letters, 2012. **108**(19): p. 196802.

179. Zeng, H., et al., *Optical signature of symmetry variations and spin-valley coupling in atomically thin tungsten dichalcogenides.* Sci. Rep., 2013. **3**.

180. Fleischmann, M., P.J. Hendra, and A.J. McQuillan, *Raman spectra of pyridine adsorbed at a silver electrode.* Chemical Physics Letters, 1974. **26**(2): p. 163-166.

181. Jeanmaire, D.L. and R.P. Van Duyne, *Surface raman spectroelectrochemistry: Part I. Heterocyclic, aromatic, and aliphatic amines adsorbed on the anodized silver electrode.* Journal of Electroanalytical Chemistry and Interfacial Electrochemistry, 1977. **84**(1): p. 1-20.

182. S. Nie, S.R.E., *Probing Single Molecules and Single Nanoparticles by Surface-Enhanced Raman Scattering.* Science, 1997. **275**: p. 1102.

183. Kneipp, K., et al., *Single Molecule Detection Using Surface-Enhanced Raman Scattering (SERS).* Physical review letters, 1997. **78**(9): p. 1667-1670.

184. Moskovits, M., *Surface-enhanced spectroscopy.* Reviews of Modern Physics, 1985. **57**(3): p. 783-826.

185. Kneipp, K., et al., *Ultrasensitive Chemical Analysis by Raman Spectroscopy.* Chemical Reviews, 1999. **99**(10): p. 2957-2976.

186. Garrell, R.L., *Surface-enhanced Raman spectroscopy.* Analytical Chemistry, 1989. **61**(6): p. 401A-411A.

187. Campion, A. and P. Kambhampati, *Surface-enhanced Raman scattering.* Chemical Society Reviews, 1998. **27**(4): p. 241-250.

188. Chang, K. and W. Chen, *l-Cysteine-Assisted Synthesis of Layered* MoS_2*/Graphene Composites with Excellent Electrochemical Performances for Lithium Ion Batteries.* ACS nano, 2011. **5**(6): p. 4720-4728.

189. Ling, X., et al., *Can Graphene be used as a Substrate for Raman Enhancement?* Nano Letters, 2009. **10**(2): p. 553-561.

190. Mohanty, N. and V. Berry, *Graphene-Based Single-Bacterium Resolution Biodevice and DNA Transistor: Interfacing Graphene Derivatives with Nanoscale and Microscale Biocomponents.* Nano Letters, 2008. **8**(12): p. 4469-4476.

191. Shan, C., et al., *Direct Electrochemistry of Glucose Oxidase and Biosensing for Glucose Based on Graphene.* Analytical Chemistry, 2009. **81**(6): p. 2378-2382.

192. Huh, S., et al., *UV/Ozone-Oxidized Large-Scale Graphene Platform with Large Chemical Enhancement in Surface-Enhanced Raman Scattering.* ACS nano, 2011. **5**(12): p. 9799-9806.

193. Thrall, E.S., et al., *R6G on Graphene: High Raman Detection Sensitivity, Yet Decreased Raman Cross-Section.* Nano Letters, 2012. **12**(3): p. 1571-1577.

194. Ju, L., et al., *Graphene plasmonics for tunable terahertz metamaterials.* Nat Nano, 2011. **6**(10): p. 630-634.

195. Jiang, H., *Electronic Band Structures of Molybdenum and Tungsten Dichalcogenides by the GW Approach.* The Journal of Physical Chemistry C, 2012. **116**(14): p. 7664-7671.

196. Lv, R., et al., *Nitrogen-doped graphene: beyond single substitution and enhanced molecular sensing.* Sci. Rep., 2012. **2**.

197. Yu, X., et al., *Increased chemical enhancement of Raman spectra for molecules adsorbed on fluorinated reduced graphene oxide.* Carbon, 2012. **50**(12): p. 4512-4517.

198. Wu, S., et al., *Vapor–Solid Growth of High Optical Quality MoS_2 Monolayers with Near-Unity Valley Polarization.* ACS nano, 2013.

199. Zhan, Y., et al., *Large-Area Vapor-Phase Growth and Characterization of MoS_2 Atomic Layers on a SiO_2 Substrate.* Small, 2012. **8**(7): p. 966-971.

200. Castellanos-Gomez, A., et al., *Laser-Thinning of MoS_2: On Demand Generation of a Single-Layer Semiconductor.* Nano Letters, 2012. **12**(6): p. 3187-3192.

201. Hong, J., et al., *Exploring atomic defects in molybdenum disulphide monolayers.* Nat Commun, 2015. **6**.

202. Shishoo, R., *Plasma Technologies for Textiles* 2007.

203. Liu, Y., et al., *Layer-by-Layer Thinning of MoS_2 by Plasma.* ACS nano, 2013. **7**(5): p. 4202-4209.

204. Hsiao, C.-L., et al., *Photoluminescence spectroscopy of nearly defect-free InN microcrystals exhibiting nondegenerate semiconductor behaviors.* Applied Physics Letters, 2007. **91**(18): p. 181912.

205. Monaico, E., et al., *Porosity-induced blueshift of photoluminescence in CdSe.* Journal of Applied Physics, 2006. **100**(5): p. 053517.

206. Strassburg, M., et al., *The origin of the PL photoluminescence Stokes shift in ternary group-III nitrides: field effects and localization.* physica status solidi (c), 2003. **0**(6): p. 1835-1845.

207. Qian, F., et al., *Multi-quantum-well nanowire heterostructures for wavelength-controlled lasers.* Nature materials, 2008. **7**(9): p. 701-706.

208. Ryu, S., et al., *Atmospheric Oxygen Binding and Hole Doping in Deformed Graphene on a SiO_2 Substrate.* Nano Letters, 2010. **10**(12): p. 4944-4951.

209. Zhang, Z. and J.T. Yates, *Band Bending in Semiconductors: Chemical and Physical Consequences at Surfaces and Interfaces.* Chemical Reviews, 2012. **112**(10): p. 5520-5551.

210. Yan, Y., et al., *Luminescence blue-shift of CdSe nanowires beyond the quantum confinement regime.* Applied Physics Letters, 2011. **99**(10): p. 103103.

211. Persson, B.N.J., K. Zhao, and Z. Zhang, *Chemical Contribution to Surface-Enhanced Raman Scattering.* Physical review letters, 2006. **96**(20): p. 207401.

212. Senthilkumar, V., et al., *Direct vapor phase growth process and robust photoluminescence properties of large area MoS2 layers.* Nano Research, 2014. **7**(12): p. 1759-1768.

213. Ji, Q., et al., *Epitaxial Monolayer MoS2 on Mica with Novel Photoluminescence.* Nano Letters,

2013. **13**(8): p. 3870-3877.

214. Zhou, W., et al., *Intrinsic Structural Defects in Monolayer Molybdenum Disulfide.* Nano Letters, 2013. **13**(6): p. 2615-2622.

215. Santosh KC, R.C.L., Rafik Addou, Robert M Wallace and Kyeongjae Cho, *Impact of intrinsic atomic defects on the electronic structure of MoS_2 monolayers.* Nanotechnology, 2014. **25**(37): p. 375703.

216. Xie, J., et al., *Defect-Rich MoS_2 Ultrathin Nanosheets with Additional Active Edge Sites for Enhanced Electrocatalytic Hydrogen Evolution.* Advanced Materials, 2013. **25**(40): p. 5807-5813.

217. Ghorbani-Asl, M., et al., *Defect-induced conductivity anisotropy in MoS_2 monolayers.* Physical Review B, 2013. **88**(24): p. 245440.

218. Gfroerer, T.H., *Photoluminescence in Analysis of Surfaces and Interfaces*, in *Encyclopedia of Analytical Chemistry*2006, John Wiley & Sons, Ltd.

219. Yang, X.L., et al., *Analytic solution of a two-dimensional hydrogen atom. I. Nonrelativistic theory.* Physical Review A, 1991. **43**(3): p. 1186-1196.

220. Nan, H., et al., *Strong Photoluminescence Enhancement of MoS_2 through Defect Engineering and Oxygen Bonding.* ACS nano, 2014. **8**(6): p. 5738-5745.

221. Tongay, S., et al., *Defects activated photoluminescence in two-dimensional semiconductors: interplay between bound, charged, and free excitons.* Sci. Rep., 2013. **3**.

222. Tongay, S., et al., *Broad-Range Modulation of Light Emission in Two-Dimensional Semiconductors by Molecular Physisorption Gating.* Nano Letters, 2013. **13**(6): p. 2831-2836.

223. Liu, Z., et al., *Strain and structure heterogeneity in MoS_2 atomic layers grown by chemical vapour deposition.* Nat Commun, 2014. **5**.

224. Castellanos-Gomez, A., et al., *Local Strain Engineering in Atomically Thin MoS_2.* Nano Letters, 2013. **13**(11): p. 5361-5366.

225. Conley, H.J., et al., *Bandgap Engineering of Strained Monolayer and Bilayer MoS_2.* Nano Letters, 2013. **13**(8): p. 3626-3630.

226. Lu, P., et al., *Strain-dependent electronic and magnetic properties of MoS_2 monolayer, bilayer, nanoribbons and nanotubes.* Physical Chemistry Chemical Physics, 2012. **14**(37): p. 13035-13040.

227. Hui, Y.Y., et al., *Exceptional Tunability of Band Energy in a Compressively Strained Trilayer MoS2 Sheet.* ACS nano, 2013. **7**(8): p. 7126-7131.

228. Wang, Y., et al., *Raman Spectroscopy Study of Lattice Vibration and Crystallographic Orientation of Monolayer MoS_2 under Uniaxial Strain.* Small, 2013. **9**(17): p. 2857-2861.

229. Lei Yang, X.C., Jingyu Zhang, Kan Wang, Meng Shen, Shuangshuang Zeng, Shadi A Dayeh, Liang Feng, and Bin Xiang,, *Lattice strain effects on the optical properties of MoS_2 nanosheets.* Scientific reports, 2014. **4**.

230. Attaccalite, C., et al., *Doped Graphene as Tunable Electron−Phonon Coupling Material.* Nano Letters, 2010. **10**(4): p. 1172-1176.

231. Chakraborty, B., et al., *Symmetry-dependent phonon renormalization in monolayer MoS_2 transistor.* Physical Review B, 2012. **85**(16): p. 161403.

232. Popov, I., G. Seifert, and D. Tománek, *Designing Electrical Contacts to MoS_2 Monolayers: A Computational Study.* Physical review letters, 2012. **108**(15): p. 156802.

233. Peimyoo, N., et al., *Chemically Driven Tunable Light Emission of Charged and Neutral Excitons*

in Monolayer WS_2. ACS nano, 2014. **8**(11): p. 11320-11329.

234. Mouri, S., Y. Miyauchi, and K. Matsuda, *Tunable Photoluminescence of Monolayer MoS2 via Chemical Doping.* Nano Letters, 2013. **13**(12): p. 5944-5948.
235. Siviniant, J., et al., *Chemical equilibrium between excitons, electrons, and negatively charged excitons in semiconductor quantum wells.* Physical Review B, 1999. **59**(3): p. 1602-1604.
236. Vercik, A., Y.G. Gobato, and M.J.S.P. Brasil, *Thermal equilibrium governing the formation of negatively charged excitons in resonant tunneling diodes.* Journal of Applied Physics, 2002. **92**(4): p. 1888-1892.
237. Butler, S.Z., et al., *Progress, Challenges, and Opportunities in Two-Dimensional Materials Beyond Graphene.* ACS nano, 2013. **7**(4): p. 2898-2926.
238. Akinwande, D., N. Petrone, and J. Hone, *Two-dimensional flexible nanoelectronics.* Nat Commun, 2014. **5**.
239. Kim, S.J., et al., *Materials for Flexible, Stretchable Electronics: Graphene and 2D Materials.* Annual Review of Materials Research, 2015. **45**(1): p. null.
240. *Physical Vapor Deposition (PVD) to Synthesize* MoS_2, in *Encyclopedia of Tribology*, Q.J. Wang and Y.-W. Chung, Editors. 2013, Springer US. p. 2523-2523.
241. Tan, L.K., et al., *Atomic layer deposition of a* MoS_2 *film.* Nanoscale, 2014. **6**(18): p. 10584-10588.
242. Jin, Z., et al., *Novel chemical route for atomic layer deposition of* MoS_2 *thin film on* SiO_2/Si *substrate.* Nanoscale, 2014. **6**(23): p. 14453-14458.
243. Geim, A.K. and I.V. Grigorieva, *Van der Waals heterostructures.* Nature, 2013. **499**(7459): p. 419-425.
244. Gong, Y., et al., *Vertical and in-plane heterostructures from* WS_2/MoS_2 *monolayers.* Nature materials, 2014. **13**(12): p. 1135-1142.
245. Wang, X. and F. Xia, *Van der Waals heterostructures: Stacked 2D materials shed light.* Nature materials, 2015. **14**(3): p. 264-265.
246. Wong, H.S.P., et al., *Phase Change Memory.* Proceedings of the IEEE, 2010. **98**(12): p. 2201-2227.
247. Wuttig, M., *Phase change materials: Chalcogenides with remarkable properties due to an unconventional bonding mechanism.* physica status solidi (b), 2012. **249**(10): p. 1843-1850.
248. Raoux, S., W. Wełnic, and D. Ielmini, *Phase Change Materials and Their Application to Nonvolatile Memories.* Chemical Reviews, 2010. **110**(1): p. 240-267.
249. Hsieh, W.-P., et al., *High-pressure Raman spectroscopy of phase change materials.* Applied Physics Letters, 2013. **103**(19): p. 191908.
250. Goncharov, A.F., *Raman Spectroscopy at High Pressures.* International Journal of Spectroscopy, 2011. **2012**.